UNIVERSITÀ DEGLI STUDI DI NAPOLI "FEDERICO II"
DIPARTIMENTO DI INGEGNERIA INDUSTRIALE

DOTTORATO DI RICERCA IN INGEGNERIA AEROSPAZIALE,
NAVALE E DELLA QUALITÀ

XXVII CICLO

TESI DI DOTTORATO

Swirl and precession in submerged free and confined jets

Giuseppe Ceglia

Tutor:
Prof. Ing. Tommaso Astarita

Coordinatore:
Prof. Ing. Luigi de Luca

Marzo 2016

“Blues is easy to play,
but not to feel.”
Jimi Hendrix

Table of Contents

Abstract

The present thesis deals with an experimental investigation on swirl and precession in free and confined submerged jets in cold flow conditions by means of tomographic particle image velocimetry. Swirling and precessing jets are widely used to enhance the mixing performance in combustion applications. Therefore, the aim of the present research is devoted to elucidate insights on the 3D flow patterns of swirling flows characterized by either a periodic-stable precessing helical structures or intermittent bi-stable fluidic mechanism that produces a large scale precessing motion. To this purpose, a lean pre-vaporized premixed swirl injector is characterized through the study of its main flow features generated in free and confined configurations. Whereas, a fluidic precessing jet nozzle is undertaken to inspect the flow features characteristics of the precessing motion. Moreover, the precessing jet has been investigated for two inflow conditions using either a short-pipe nozzle, i.e., jet without grid, or placing a regular grid at the inlet. The flow features in swirling and precessing jets so generated are described in the thesis.

Nomenclature

a_b	Time coefficient, *m/s*
c	Speed of sound, *m/s*
d	Diameter of the short pipe nozzle, *m*
d_{diff}	Diffraction-limited diameter, *m*
d_{geom}	Geometric image diameter, *m*
d_p	Particle physical diameter, *m*
d_τ	Particle image diameter, *m*
D	Inner diameter of the cylindrical chamber, *m*
D_e	Equivalent nozzle diameter, *m*
D_S	Diameter of the swirler, m
E	3D intensity distribution of the light scattered by the tracer particles
f	Frequency, *Hz*
$f_\#$	Focal ratio
f_L	Objective focal length, *m*
f_p	Precession frequency, *Hz*
f_r	Resonant frequency, *Hz*
$\underline{\underline{F}}$	Generic tensor
$\underline{g_b}$	Orthonormal basis function of the proper orthogonal decomposition
G_y	Axial flux of axial momentum, *N*
G_θ	Axial flux of swirl momentum, *N m*
h	Step height, *m*
I_a	Pixel intensity of the first exposure
I_b	Pixel intensity of the second exposure
L	Length of the cylindrical chamber, *m*
L_I	Size of the interrogation window, *pixel*
M_0	Lateral magnification
N	Number of snapshots
N_{cam}	Number of cameras
N_g	Number of ghost particles

N_m	Number of modes
N_p	Number of actual particles
N_{pix}	Number of pixels
N_{ppp}	Particle density
N_s	source density
N_{vox}	Number of voxels
P_p	Pixel pitch, *m*
Q	Second invariant of the velocity gradient, s^{-2}
Q_V	Volume flow rate, m^3/s
R	Radial coordinate, *m*
R_{corr}	Cross-correlation coefficient
R_{ij}	Two-point temporal correlation matrix, m^2/s^2
Re	Reynolds number
Re_{Tube}	Reynolds number based on the duct diameter
Re_d	Reynolds number based on the diameter of the fluidic PJ nozzle
Re_{D_S}	Reynolds number based on the diameter of the swirler LPP injector
S	Swirl number
$\underline{\underline{S}}$	Strain rate tensor, s^{-1}
St_p	Strouhal number of the precessing motion
St_h	Strouhal number based on the step height
$St_{p_{crit}}$	Critical Strouhal number of the precessing motion
t	Time coordinate, *s*
Δt	Adjustable time delay, *s*
Δt_{ac}	Time delay between two subsequent acquired samples, *s*
u'	Transverse velocity fluctuation, *m/s*
u'_{rms}	Root mean square of the transverse velocity fluctuation, *m/s*
U	Transverse velocity component, *m/s*
$\overline{U}$	Transverse mean velocity component, *m/s*
v'	Axial velocity fluctuation, *m/s*
v_r'	Radial velocity fluctuation, *m/s*
v_θ'	Azimuthal velocity fluctuation, *m/s*
v'_{rms}	Root mean square of the axial velocity fluctuation, *m/s*

V	Axial velocity component, *m/s*
$\bar{V}$	Axial mean velocity component, *m/s*
V_0	Maximum axial velocity, *m/s*
V_j	Bulk velocity, *m/s*
V_r	Radial velocity component, *m/s*
V_θ	Azimuthal velocity component, *m/s*
w'	Depth velocity fluctuation, *m/s*
$w_{j,k}$	Weighting coefficients
w'_{rms}	Root mean square of the depth velocity fluctuation, *m/s*
W	Depth velocity component, *m/s*
$\bar{W}$	Depth mean velocity component, *m/s*
x	Image plane coordinate, *m*
Δx	Transverse mean displacement of the particles image, *pixels*
Δx_p	Transverse image displacement, *m*
X	Transverse coordinate, *m*
X_p	Transverse particle location in the physical space, *m*
ΔX_p	Transverse physical displacement, *m*
y	Axial image plane coordinate, *m*
Δy	Axial mean displacement of the particles image, *pixels*
Δy_p	Axial image displacement, *m*
Y	Axial coordinate, *m*
Y_p	Axial particle location in the physical space, *m*
ΔY_p	Axial physical displacement, *m*
δz	Focal depth, *m*
Δz_p	Depth image displacement, *m*
Z	Depth coordinate, *m*
Z_p	Depth particle location in the physical space, *m*
ΔZ_0	Thickness of the light sheet, *m*
ΔZ_p	Depth physical displacement, *m*
ΔZ_V	Depth of an illuminated volume, *m*

Greek symbols

α	Exit angle of the mechanical precessing jet nozzle, °
α_S	Half spreading angle, °
β	Deflection angle of the emerging precessing jet, °
Γ	Local circulation, m^2/s
δ	Vortex core radius, m
θ	Azimuthal coordinate, °
λ_i	Eigenvalue corresponding to i-th mode, m^2/s^2
λ_L	Wavelength of the illuminating source, m
λ_r	Wavelength of resonance, m
λ_2	Second largest eigenvalue of $\left\|\underline{\underline{\Omega}}\right\|^2 + \left\|\underline{\underline{S}}\right\|^2$, s^{-2}
μ_a	Mean intensity of the correlation windows for the first exposure
μ_b	Mean intensity of the correlation windows for the second exposure
μ_M	Scalar relaxation parameter
ν	Kinematic viscosity, m^2/s
φ	Phase angle, °
ω_r	Radial vorticity, s^{-1}
ω_y	Axial vorticity, s^{-1}
ω_z	Depth vorticity, s^{-1}
ω_θ	Azimuthal vorticity, s^{-1}
Ω	Circulation number
$\underline{\underline{\Omega}}$	Vorticity tensor, s^{-1}

Acronym

AJ	Axial jet
CC	Cyclone combustors
CCD	Charge Coupled Device
CDS	Cyclone dust separator
CL	Centreline
CMOS	Metal-Oxide Semiconductor
CRZ	Central recirculation zone

CSMART	Camera-simultaneous multiplicative algebraic reconstruction technique
EJR	Exit jet region
IRZ	Inner recirculation zone
ISL	Inner shear layer
JWG	Jet without grid
LDA	Laser Doppler anemometry
LOR	Low order reconstruction
LPP	Lean pre-vaporized premixed
MBSG	Ljmuiden movable bock swirl burner
MIR	Middle internal region
MLOS	Multiplicative line of sight
MTE	Motion tracking enhancement
ORZ	Outer recirculation zone
OSL	Outer shear layer
ppp	particle per pixel
PDF	Probability density function
PIV	Particle image velocimetry
PJ	Precessing jet
POD	Proper orthogonal decomposition
PSB	Power station boilers
PVC	Precessing vortex core
PVC	Precessing vortex core
rms	Root mean square
RG	Regular grid
SB	Swirl burner system
SER	Sudden expansion region
SMART	Simultaneous multiplicative algebraic reconstruction technique
TKE	Turbulent kinetic energy
VODIM	Volume deformation iterative multigrid
W	Wall pressure measurements

Introduction

In turbulent combustion systems, the role of the mixing between fuel and oxidant is of fundamental importance in determining the performance of combustion processes in terms of efficiency, stability and radiation of flames and NO_x emissions (Nathan et al. 2006). The driving requirements strongly depend upon the applications; for example in gas turbine, the residence time of the species (normally a few milliseconds) has to be minimized in order to reduce the radiant heat transfer at the exposed wall of a combustion chamber; in contrast, for furnaces and kilns the leading mechanism in heat transfer is the radiance, thus making very desirable a long residence time (typically of several seconds).

Considerable efforts have been placed upon the development of devices that excite and enhance the large scale coherent structures embedded in shear layer of jets. Indeed, the organization of these structures influences the combustion process in terms of mass and momentum transport of the species (Mungal et al. 1991). It is possible to promote their mixing by increasing the initial spreading rate of jets with acoustic excitation (Reynolds et al. 2003), that is achieved either by an external forcing (e.g. using a loud speaker) or by self-excitation, using the natural coupling of flow instabilities and acoustic resonance (Hill and Greene, 1977). This approach intensifies the coherence of the large-scale structures within the near field and, for combustion applications, reduces the flame volume (Gutmark et al. 1989). Nevertheless, the acoustic excitation induces a periodic forcing in the flow field producing regular pressure oscillations causing stress by fatigue of the structural components. To overcome this disadvantage, mechanically oscillating devices were developed without compromising the enhancing of the jet mixing. Their effectiveness has been proved in cold flows, while in practical applications, such as in combustion chambers, the moving parts suffer the degradation process due to the thermal and chemical processes arising in high temperature environments. Another strategy to stimulate the oscillations of the large-scale structures is the use of fluidically excited devices, such as flapping jets (Mi et al. 2001) or precessing jets (Nathan, 1988).

Precessing jet PJ nozzles are bundled in a specific category of devices that promote such oscillations in axisymmetric jets. They are equivalent, in three-dimensional form, to the two-dimensional flapping jets (Reynolds et al. 2003). In this framework, the

precessing motion describes the azimuthal oscillation of an emerging jet about an axis other than its own centreline (Nathan et al. 2006).

Similarities on the basic mechanism that originate the precessing flows have been observed for the precessing vortex cores PVC, that can occur in swirl flows (Syred, 2006).

In gas turbine combustors, such oscillating flows compromise the combustion processes introducing flame instabilities. In order to promote the flame stabilization, swirling jets are used in gas turbine combustors to generate an inner recirculation region near the jet nozzle (Lilley, 1977). Moreover, swirling flows have demonstrated their capability in reducing the pollutants emissions (Lucca-Negro and O'Doherty, 2001) and improving the control of the combustion processes. On the other hand, PJ flows have demonstrated to be extremely interesting features in terms of reduction of the global flame strain rate, thus leading to an increasing of volume of soot. The larger amount of soot enhances the radiative heat transfer, reducing the flame temperature and the production of NO_x (Newbold et al. 1997, Newbold et al. 2000). PJ devices have found applications in industrial processes where the simultaneous reduction of NO_x and the enhancing of the efficiency in product throughput is required (Nathan et al. 2006).

The aim of this thesis is devoted to the description of the 3D flow patterns arising in swirling flows characterized by either a periodic-stable precessing helical structures or intermittent bi-stable fluidic mechanism that produces large scale precessing motion. In particular, the effect of these precessing coherent structures on the flow organization under an imparted or naturally triggered swirl motion is addressed.

The thesis has been divided as following: Chapter 1 reviews the current literature, Chapter 2 describes the fundamentals of the measurement technique and gives a description of the data reduction methods, Chapter 3 outlines the design and the technical solutions of the experimental setup, Chapters 4 and 5 discuss the results relative to the swirling and precessing jets, Chapter 6 summarizes the main findings together with final conclusions and draws perspectives on future investigations.

Chapter 1

Literature review

In this chapter, the definitions and terminology of the physical concepts relative to swirling and precessing jet flows are introduced. Particularly emphasis is placed upon fundamental aspects of flow field topologies featuring such flows and the main technical solutions in combustion application.

1.1 Swirling flows

Swirling flows are generated from the application of spiralling motion, characterized by a swirl velocity component, referred in literature as tangential or azimuthal velocity component V_θ (Lilley, 1977). The most common solutions adopted to generate a swirling flow are probably radial swirl vanes (Harvey, 1962) or axial-tangential fluid entry (Chigier and Chervinsky, 1967). Recently, multiple swirler systems in radial configuration are employed in gas turbine combustors (Huang et al. 2013) to obtain a further improvement of the flame stability and reduction of the emission of pollutants.

According to the Buckingham-Pi theorem (Buckingham, 1914), a swirling flow can be characterized by two non-dimensional numbers, the Reynolds number Re_d, and the swirl number S. In the present investigation, the Reynolds number is based on the bulk velocity V_j and the diameter of the nozzle exit d. It reads as:

$$Re_d = \frac{V_j d}{\nu} \qquad 1.1.$$

Where ν is the kinematic viscosity. In addition, the degree of swirl is evaluated by means of S, which represents the axial flux of swirl momentum G_θ divided by axial flux of axial momentum G_y times the half of the equivalent nozzle diameter D_e (Gupta et al. 1984).It is given by

$$S = \frac{2G_\theta}{G_y D_e} \qquad 1.2$$

1.1.1 Flow characteristics of swirling jets

The introduction of a swirl in turbulent axisymmetric jets dramatically changes its flow field topology (Yule, 1978); increasing the level of swirl, the growth and entrainment rate of the jet are intensified (Gupta et al. 1984). At low swirl level (S<0.6), centrifugal effects, due to the term ${V_\theta}^2/R$, produce significant centrifugal pressure gradients along the

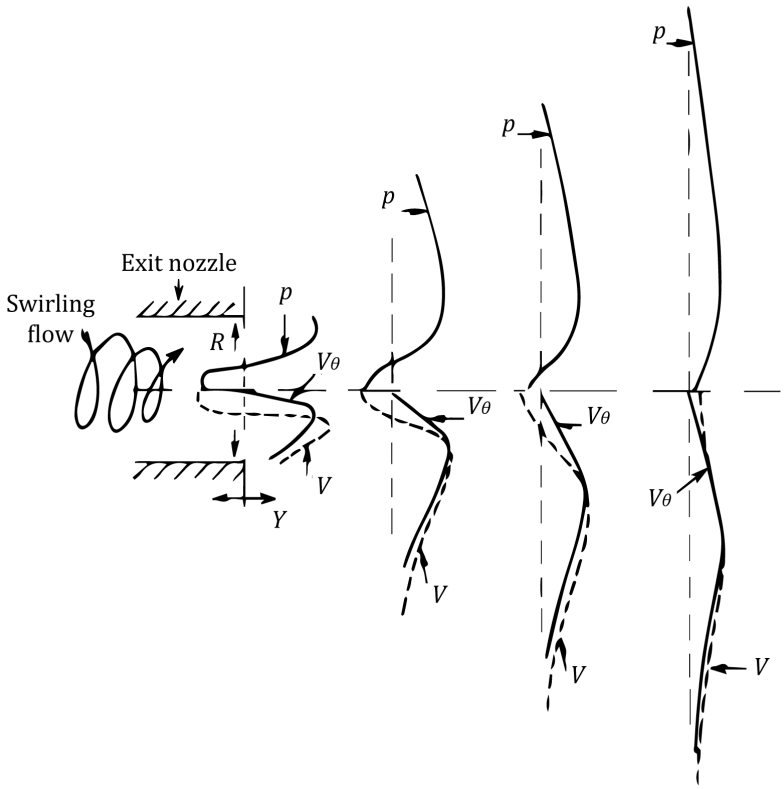

Figure 1.1 Schematic of the process leading to the formation of CRZ (extracted from Gupta et al. 1984): azimuthal velocity profile (V_θ) generates a centrifugal pressure gradient reducing the pressure (p) in the vicinity of the jet axis; subsequently, azimuthal velocity decreases along the axial direction causing a reduction of the radial centrifugal pressure gradient; as a consequence, an axial pressure gradient establishes on the axis of the jet and promotes the recirculation of the flow.

radial direction *R* without axial recirculation of the flow; the expected coupling between the axial and azimuthal velocity components does not occur.

Increasing the level of swirl, the combination effect between the axial and azimuthal components develops an adverse pressure gradient along the axial direction that dominates on the kinetic energy of the fluid flowing in the axial direction. A central recirculation zone CRZ with a reverse flow is formed in the vicinity of the jet axis. A schematic of the process leading to the formation of the CRZ is illustrated in Figure 1.1.

The CRZ is strongly dependent on the azimuthal velocity decay as the swirling jet expands (Syred, 2006). In the early investigation by Harvey (1962), experiments on swirling flows within a long tube were conducted at different swirl levels. The study was focused on the onset of the 'vortex breakdown' by varying the amount of swirl imparted

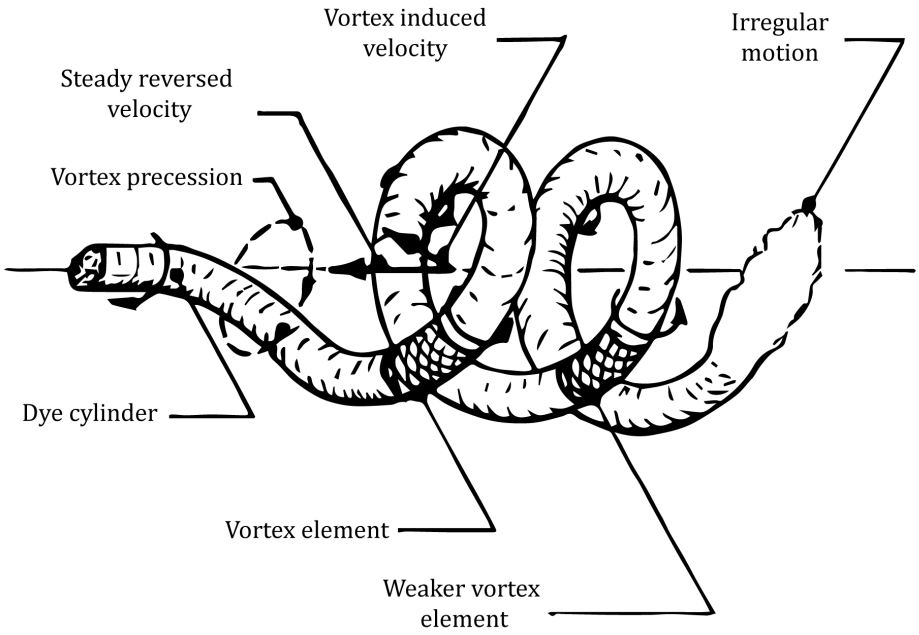

Figure 1.2 Sketch of the periodic motion of the spiral vortex (adapted from Chanaud 1965).

upstream. It was found an intermediate stage between a weak swirling flows, which does not exhibit reversal flows, and a rapidly swirling flows that produce the reverse of the axial velocity component.

In his observations, the breakdown was described as "*…giving the impression that an imaginary body of revolution has been placed on the axis of the vortex, around which the fluid is obliged to flow*". Chanaud (1965) observed an oscillatory motion of a flow characterized by a disturbed azimuthal velocity component in a tube at different Reynolds numbers Re_{Tube} (based on the diameter of the duct). At a certain value of Re_{Tube}, this oscillation produces a reversed steady flow. Increasing the flow rate, the amplitudes of this periodic motion increases and a spiral flow field is formed causing an upstream displacement of the stagnation point. A representation of such oscillating motion is illustrated in Figure 1.2.

For different flow rates and swirl levels imparted to the fluid flowing into a slightly divergent cylindrical tube, Sarpkaya (1971) recognized three types of vortex breakdown: double helix, axisymmetric (bubble) and spiral. Whereas, at higher Reynolds numbers it is

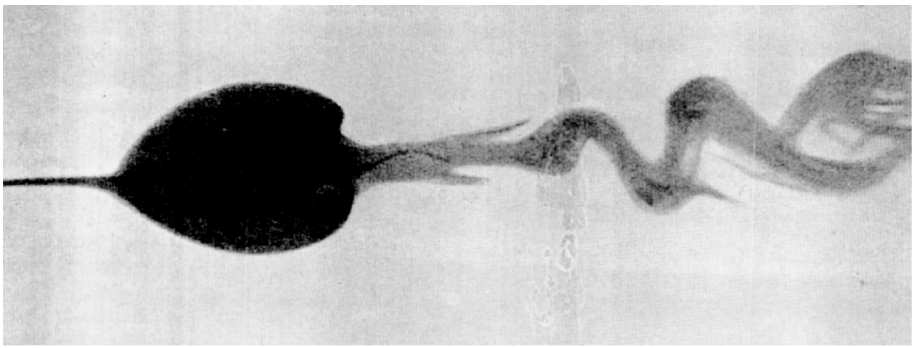

Figure 1.3 Axisymmetric breakdown with spiralling tail (extracted from Sarpkaya 1971).

possible to observe only the bubble and spiral geometric forms (Lucca-Negro and O'Doherty, 2001).

The axisymmetric breakdown is represented in Figure 1.3, it is characterized by a toroidal vortex ring located downstream of a bubble. By inspecting a time sequence of pictures, Sarpkaya (1971) observed that this ring vortex participates to a fluid exchange between the bubble and its spiralling wake. Further downstream, the vortex core expands and becomes weaker with an axial velocity deflection in the wake before its breaking up into a spiralling turbulent structures.

In the spiral breakdown, the filament is abruptly decelerated along the axial direction causing the formation of a stagnation point as shown in Figure 1.4. The vortex filament undergoes a twisting activity that produces a 'corkscrew-like' shape growing in one or two cycles before breaking up into large-scale turbulence (Lucca-Negro and O'Doherty, 2001).

An interesting feature of this type of breakdown lies on the relation between the sense of the winding and the rotation of the spiral with that of the external imparted swirl. It is found that this relation is sensitive on the method of generation of the upstream swirl and the profile of the axial velocity. By exciting helical mode instability of the vortex breakdown by using a loud speaker installed asymmetrically respect to the axis of a guided-vane swirler, Gursul (1993) observed that for a jet-like axial velocity profile the spiral is counter-winding with respect to the main swirl; whereas for a wake-like axial velocity profile the disturbance rotates in the same direction as the main swirl.

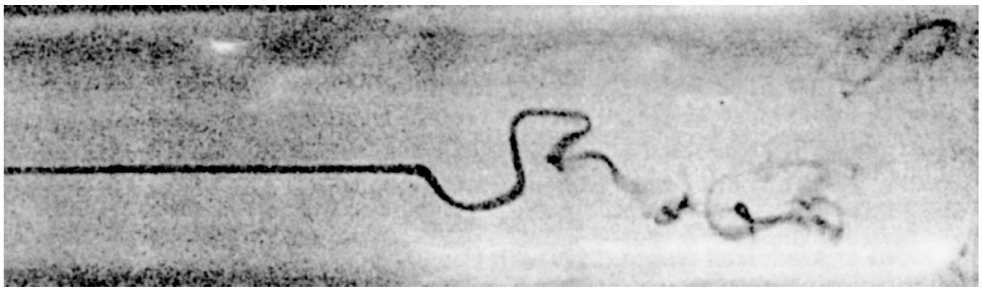

Figure 1.4 Spiral type breakdown: dye filament, 'corkscrew-like' shape and breaking up to turbulent coherent structures (extracted from Leibovich 1978).

Furthermore, these forms of breakdown follow a well-defined evolutionary pattern when the flow parameters vary in a certain range (Lucca-Negro and O'Doherty, 2001). Sarpkaya (1971) identified an order of progression between the axisymmetric and spiral bubble. In Figure 1.5, position and mode of the vortex breakdown with respect to the Reynolds number (based on the equivalent diameter D_e) is presented at different values of circulation number $\Omega = \pi\Gamma D_e/4Q_V$ (Sarpkaya, 1971), where Γ and Q_V are the local circulation and the volume flow rate, respectively. As the swirl increases, the spiral breakdown always occurs downstream respect to the axisymmetric breakdown and the spiral moves upstream. At larger level of swirl, the spiral is formed more rapidly and transforms itself into bubble breakdown. Further increasing the circulation number, Escudier and Zehnder (1982) observed that the vortex breakdown exhibits steady features and moves upstream reaching the exit of the swirl generator. In addition, an increase of the rotational frequency of the wake moving closer to the jet axis was detected. On the other hand, even though a definite progression of forms were observed, Sarpkaya (1971) also recognized an hysteresis region where a spiral, or 'bubble', form is conserved when the swirl level increases (decreases).

The existence of an adverse axial pressure gradient affects the evolution of the vortex breakdown. Cassidy and Falvey (1970) in their early observations detected an increasing of the precession frequency of the helical vortex when the exit of the duct is in part blocked. Reducing the axial velocity at the exit of the duct, Sarpkaya (1971) noticed a rapid upstream displacement of the breakdown event along the streamwise direction. These findings were inferred for imposed axial pressure gradients imparted externally to swirling flows.

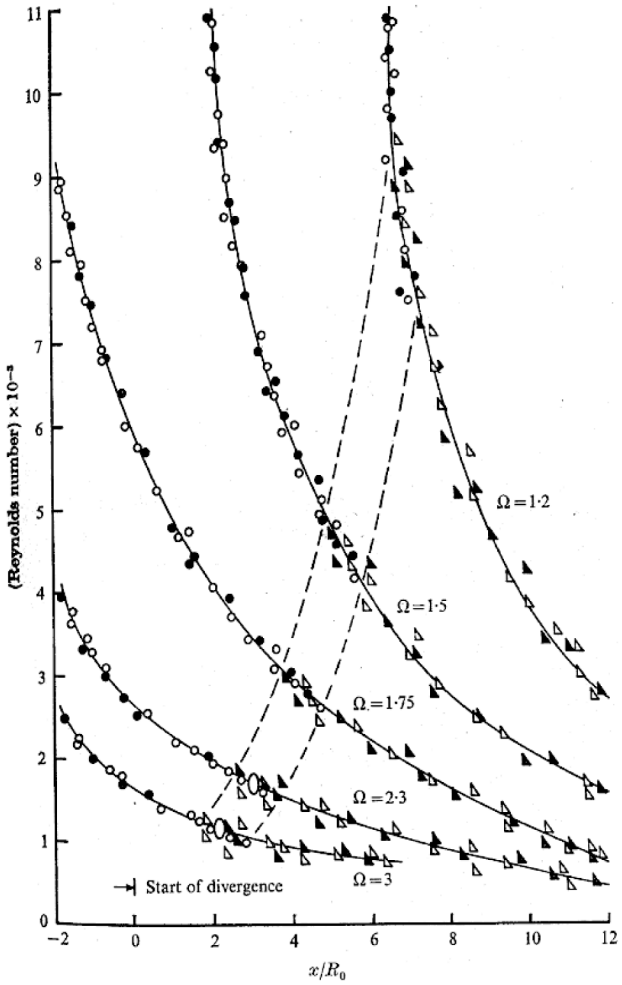

Figure 1.5 Vortex breakdown position as a function of Reynolds number and circulation numbers Ω, (○, ●) axisymmetric and (◺, ◣) spiral breakdown forms (extracted from Sarpkaya 1971).

A new approach was introduced by Hall (1967), who deduced that the axial pressure gradient is a combination of an imposed external pressure gradient and the contribution related to the presence of the swirl. Considering that the azimuthal velocity profile consists of forced and free vortex distributions (known as Rankine vortex), for an inviscid flow the axial pressure gradient $dp/dx|_0$ on the jet axis reads as (Escudier and Zehnder 1982, Lucca-Negro and O'Doherty 2001)

$$\left(\frac{dp}{dx}\right)_0 = \left(\frac{dp}{dx}\right)_\infty + \frac{2\rho}{\delta^3}\left(\frac{\Gamma_\infty}{2\pi}\right)^2 \frac{d\delta}{dx} \qquad 1.3.$$

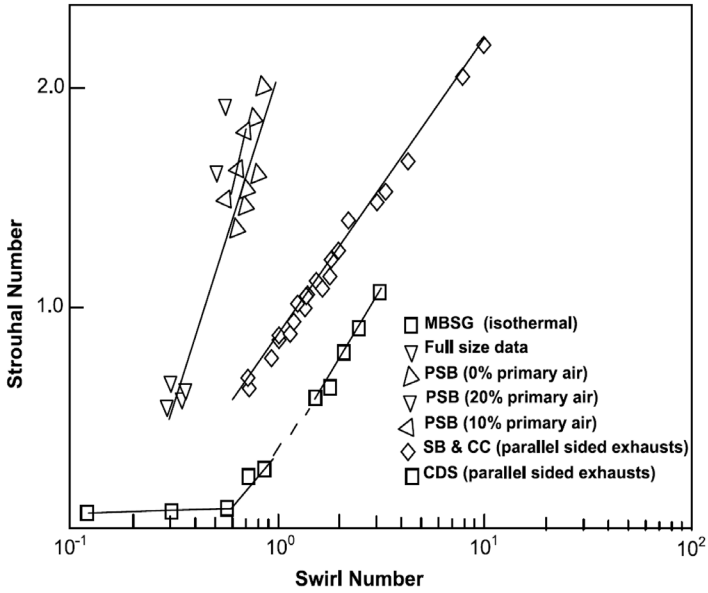

Figure 1.6 Strouhal number as a function of swirl number S at high Reynolds number. PSB power station boilers, SB swirl burner system, CC cyclone combustors, MBSG Ijmuiden movable bock swirl burner and CDS cyclone dust separator (adapted from Syred 2006).

Where $dp/dx|_{\infty}$ and Γ_{∞} are the imposed pressure gradient and the local circulation in the far field, respectively; δ represents the vortex core radius. Equation (1.3) indicates that the swirl contribution is positive if the vortex core expands along the axial direction, this effect is more emphasized as the circulation increases. Furthermore, Krause (1985) conducted an analytic analysis on an incompressible, steady and axisymmetric flow using the momentum equation applied upstream to the breakdown axial position. He concluded that the distance between the point of instability initiation and breakdown exhibits a proportional dependency with respect to the square of the freestream velocity and an inversely dependency with the square of the maximum azimuthal velocity.

Another interesting feature that characterizes the vortex breakdown lies on its time dependent phenomenology (O'Doherty et al. 2008). In this context, in correspondence of the CRZ the forced vortex region is displaced from the axis of symmetry of the swirl generator and, under unstable processes, it starts to precess about it, thus forming the precessing vortex core PVC. The PVC is located in the CRZ between the zero tangential velocity and zero streamline (Syred and Beér 1974). Furthermore, under the action of the PVC the CRZ distorts into a 'kidney-like' shape with the presence of an helical bubble wrapping around the boundary of the CRZ (Lucca-Negro and O'Doherty, 2001).

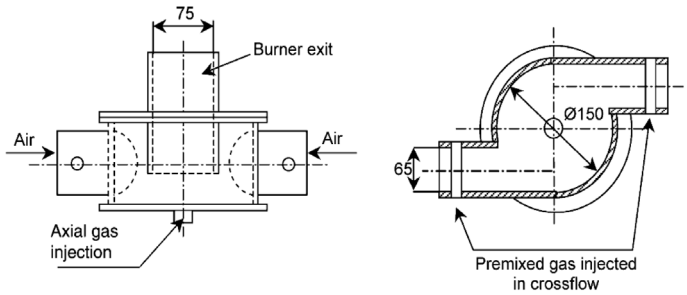

Figure 1.7 Schematic of a generic swirl burner with adjustable swirl number (extracted from Rodriguez-Martinez et al. 2006).

In isothermal conditions, the frequency of the PVC results to be characterized by the Strouhal number fD_e/V_j and the swirl number S (1.2). The Strouhal number assumes a rather asymptotic value in correspondence of high Reynolds numbers (Syred, 2006). In Figure 1.6, the relationship of these two parameters exhibits a clear dependency by the degree of swirl and the burner systems. In particular, for large power station boilers PSB (Syred et al. 1994) high values of Strouhal number correspond also to lower ones of S. For swirl burner systems SB (Gupta et al. 1984) and cyclone combustors CC (Syred et al. 1994) with parallel sided exhaust and without centrebody, the data fit onto the same curve, giving for S=1, a Strouhal number equal to 0.86. On the other hand, the Ijmuiden movable bock swirl burner MBSG (Gupta et al. 1984) returns a Strouhal number 0.37 at S=1. A similar behaviour is detected for cyclone dust separator CDS (Yazdabadi et al. 1994).

Syred (2006) described the structure of the PVC arising in the near field of a swirl burner under isothermal condition. The swirl burner is shown in Figure 1.7 and its configuration consists of two circular inlet firing into a circular chamber with the axis perpendicular with respect to the main direction of the two inlets. The flow undergoes a sudden contraction at the exhaust with a reduction of the diameter of 50%. This burner was extensively used to elucidate the phenomena related to the PVC (Doherty et al. 1994, Syred et al. 1994, Rodriguez-martinez et al. 2006). Crosswise velocity fields at the exit of the swirl burner are depicted in Figure 1.8, they were obtained from phase averaged particle image velocimetry PIV experiments (see Chapter 2 for details on the PIV experimental technique) and phase-locked laser Doppler anemometry LDA when the swirl burner was operating at S=2.6 (Syred, 2006). For reference, the geometrical axis of the burner together with its exit profile is represented.

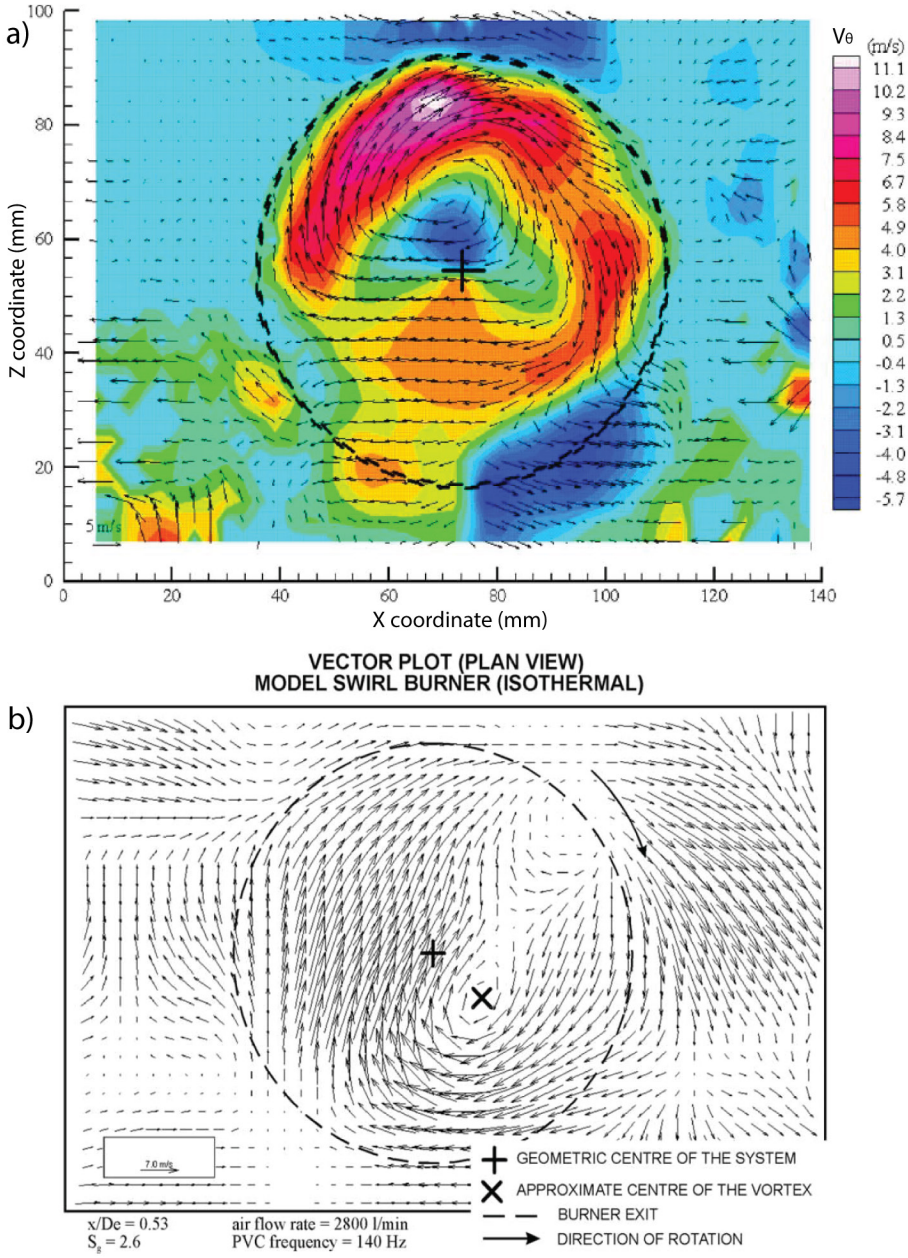

Figure 1.8 Contour of azimuthal velocity component with in-plane velocity vectors describing the footprint of one PVC (a) and velocity vectors describing the occurrence of two PVCs (b) on the plane at the nozzle exit of the burner (adapted from Syred 2006).

In Figure 1.8a, the footprint of the PVC is clearly illustrated by the in-plane velocity vectors superimposed on the contour of the azimuthal velocity. The PVC core is located in the surrounding of the axis and induces a positive azimuthal velocity along the inner region enclosed by the nozzle exit profile and a negative one around of the axis. On the other hand, Figure 1.8b shows the occurrence of two PVCs. It was also underlined that the PVC frequency increases with the flow rate quasi-linearly.

Other interesting features were carried out by Syred et al. (1994) using the swirl burner shown in Figure 1.7. From phase-locked LDA experiments, they mapped the entire periodic velocity field at axial positions Y/D_e=0.007 and 0.78 for a swirling jet at S=1.5. Figure 1.9(i) shows the azimuthal (a), axial (b) and radial (c) velocity components at the cross-sectional plane Y/D_e=0.007. As already described, in Figure 1.9(i)a the PVC induces a weaker intensity of negative azimuthal velocity around the jet axis, while high levels were detected in a sector of 120°, defined as 'banana-shaped' region, close to the outer wall of the burner. On the diametrically opposite side, low azimuthal velocity component represents the imposed swirl imparted from the burner. In Figure 1.9(i)b, the axial velocity component exhibits its maximum intensities at the same angular position as shown for that of the azimuthal component. They inferred that a bulk of flow leaves the exit burner passing through the rotating 'banana-shaped' segment inclined upwards at an angle of 45°. The reverse flow, indicated by the negative axial velocity, covers a region localized between the axis and the radial position R/D_e=0.7 over a phase angle of 100°. Figure 1.9(i)c shows the radial velocity component characterized by a region, referred as 'kidney-shaped', of negative values corresponding to an inward flow motion. Further downstream, at Y/D_e=0.78 Syred et al. (1994) observed rather axisymmetric features, even though the PVC and the reverse flow region were still present (Figure 1.9(ii)). Interesting enough, a weaker induction related to the PVC was detected, the negative azimuthal velocity region reduced its spreading and its overall intensity decreases. In addition, the 'banana-shaped' region was still evident and moved to 230° along the azimuthal direction. Syred (2006) described the footprint of axial-radial eddies on two axial planes (oriented at 90° respect to each other) investigated by means of PIV experiments on the swirl burner at S=1.7 shown in Figure 1.7. These eddies were detected into and on the CRZ and their strength was depended on the orientation of the axial plane. In other works (Masri et al. 2004, Syred et al. 2004), similar observations were reported for swirling flames, without the presence of the PVC.

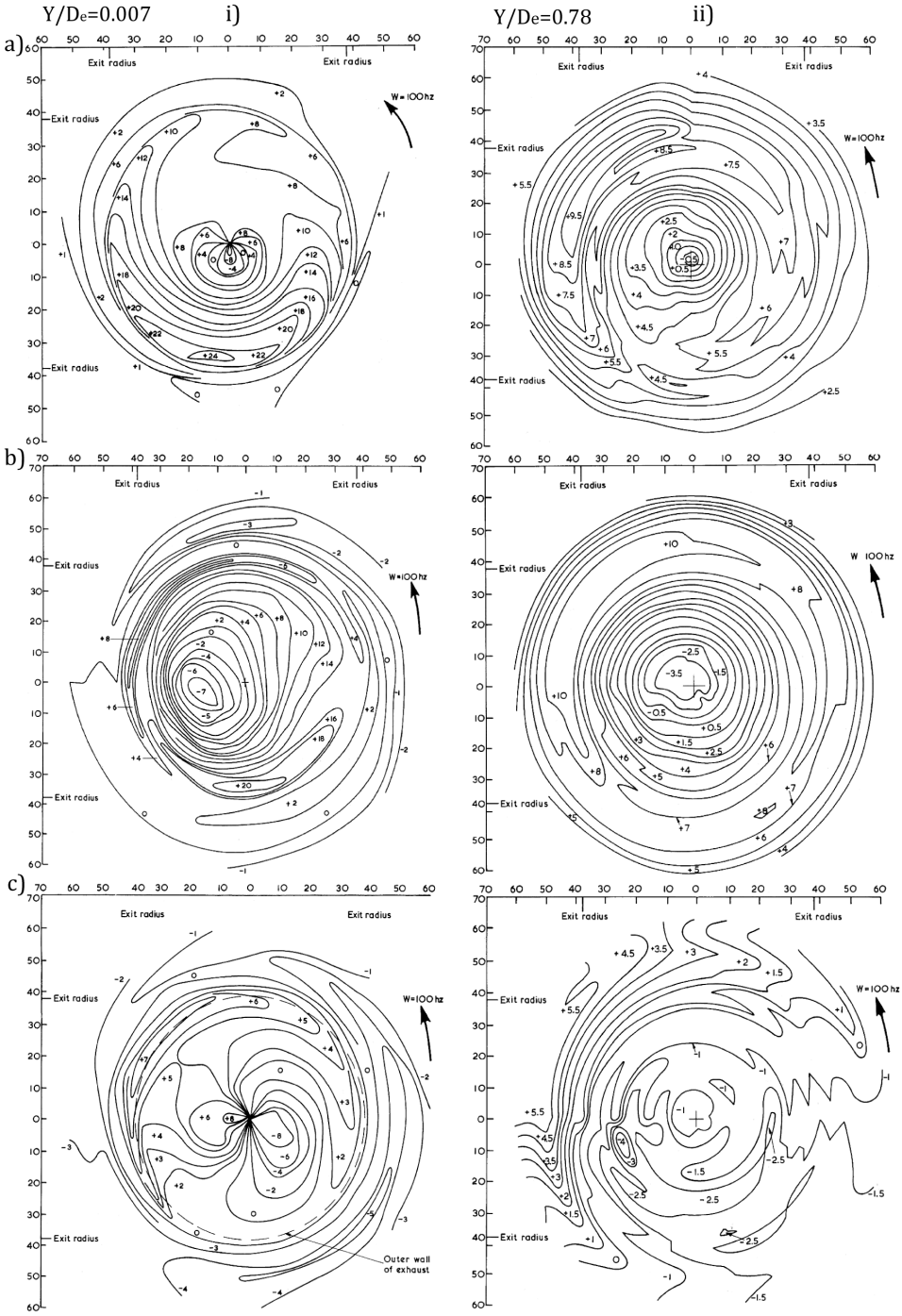

Figure 1.9 Iso-contours of phase-locked azimuthal (a), axial (b) and radial (c) velocity components on the cross-sectional planes at Y/D_e=0.007 (i) and 0.78 (ii) (adapted from Syred et al. 1994).

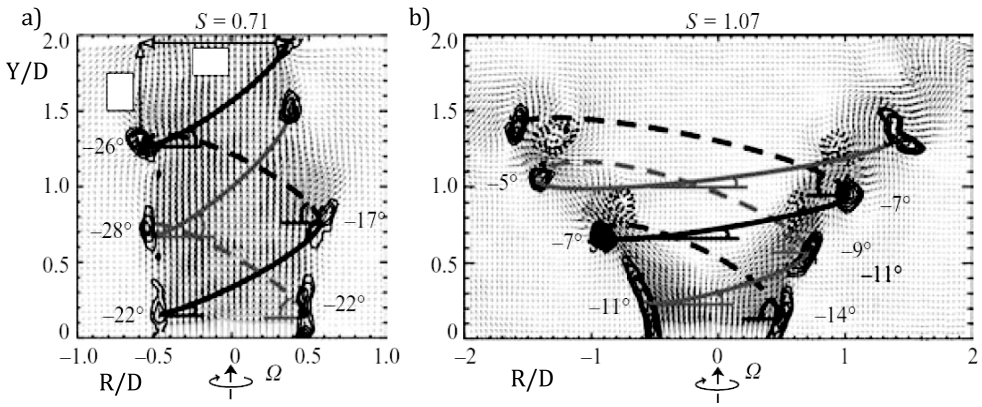

Figure 1.10 Instantaneous flow field with in-plane velocity vectors and iso-contours of azimuthal vorticity on an axial plane of swirling jets issuing at Re_{D_e}=1,000 and swirl number S=0.71 (a) and 1.07 (b). The spiral lines indicate the spatial development of counter-winding helical coherent structures (adapted from Liang and Maxworthy 2005).

Liang and Maxworthy (2005) described the spatial organization and the dynamic evolution of the vortical structures arising from swirling jets issuing at Re_{D_e}=1,000. The experimental investigation was conducted by varying the swirl number S between 0 and 1.1. For 0<S<0.6, the axial shear layer leads to the formation of axisymmetric ring vortices, also present in axisymmetric turbulent jets (Yule, 1978). Increasing the swirl (0.6<S<0.88), these vortex rings were tilted under the combined activity of the axial and azimuthal shear layers. For strongly swirling jets (S>0.88), the axial and azimuthal vorticity were comparable in intensity and the axisymmetric pattern was replaced by dominant helical vortex structures before the vortex breakdown. Furthermore, they inferred that the PVC was characterized by a vorticity with the same direction of the mean swirl vorticity while the precession motion was counter-winding with the mean swirl motion. Figure 1.10 shows instantaneous flow fields with in-plane velocity vectors and iso-contours of azimuthal vorticity on an axial plane of swirling jets at S=0.71 and 1.07, extracted from Liang and Maxworthy (2005). They underlined the presence of these counter-winding spirals with the helix angle decreasing in magnitude with the swirl number.

Oberleithner et al. (2011) investigated the evolution of a turbulent swirling jet issuing at Re_{D_e}=20,000 and S=1.22. From their experiments, they observed a self-excited global mode characterized by a well-defined dominant frequency, in particular this mode resulted to be unstable leading to a rotating counter-winding helical vortex located in the

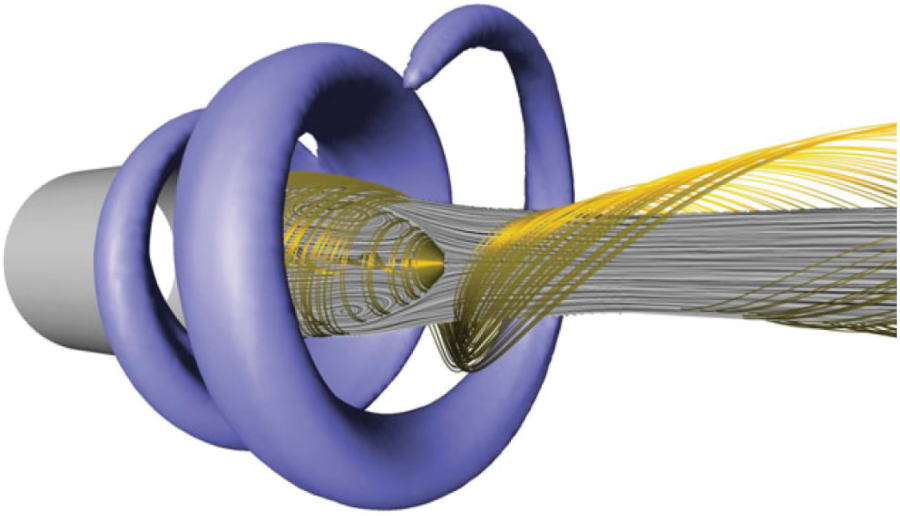

Figure 1.11 Three-dimensional flow field describing the prominent features for a swirling jet issuing at Re_{D_e}=20,000 and S=1.22. Iso-surface (violet) of azimuthal vorticity of phase-averaged velocity represents the helical coherent structure. Streamlines (gold) and linear integral convolution surface visualize the CRZ (extracted from Oberleithner et al. 2011).

periphery of the CRZ. This three-dimensional 3D coherent structure is shown in Figure 1.11, it was built up from uncorrelated two-dimensional 2D PIV data using proper orthogonal decomposition POD (see Section 2.3.2 for details) and phase averaging technique. The iso-surface of azimuthal vorticity (violet) indicates the spatial development of the helical structure, while the streamlines and the linear integral convolution (Cabral and Leedom, 1993), calculated from the averaged flow field, illustrate the CRZ.

The intensity of the PVC is stronger at the nozzle exit close to the inner shear layer ISL between the jet and the reverse flow region. The PVC extends with decaying intensity up to the boundary of the CRZ (or also referred as, for swirling jets at high swirl number inner recirculation zone IRZ) (Stöhr et al. 2011, Oberleithner et al. 2011). Additional coherent structures can be found in the outer shear layer OSL between the exiting jet and the surrounding ambient. In particular, the PVC is accompanied by a co-precessing vortex related to the convective waves through the inner and outer shear layers (Stöhr et al. 2011, Cala et al. 2006).

1.1.2 Effect of the confinement

The flow features of swirling jets are significantly influenced by the effects of the confinement. The PVC is characterized by a higher frequency and lower amplitude than that detected in free swirling jets (Syred, 2006). This effect is caused by the reduced decay of the swirl velocity component along the axis of the chamber. Along with this change, the size and strength of the IRZ increase. The ''level'' of the confinement is usually quantified with the ratio of the diameter of the confinement chamber and the diameter of the nozzle exit of the swirl burner. Smaller is this ratio and the more pronounced is the influence of the confinement. In this context, experimental investigations by Syred and Dahman (1978) addressed the effects of high level of confinement on swirling jets. They found that the size of the IRZ can be increased by inserting bluff bodies into or near the exit of the swirl burner. Sheen et al. (1996) investigated the flow field pattern in the IRZ behind of the bluff body of an annular swirling jet for both free and confined configurations. Seven different regimes for IRZ were observed, depending on the Reynolds and swirl numbers: stable flow, vortex shedding, transition, pre-penetration, penetration, vortex breakdown and attachment. Schefer et al. (1996) investigated the effects of the confinement on annular jets for variable blockage ratio (i.e., the ratio of the cross-sectional area of the inner centrebody and the duct). Their results highlight that at high level of the blockage ratio (equal to 0.83) the size of the IRZ increases, promoting the combustion stability.

1.2 Precessing jets flow

A precessing jet PJ flow originates from an abrupt expansion of an axisymmetric jet, flowing into a cylindrical short chamber, coaxial with the jet itself. During the expansion, the flow tends to attach asymmetrically to the chamber wall causing an internal recirculation. The reattaching flow precesses about the geometrical axis of the PJ nozzle producing an internal precessing motion. The natural precessing motion of a jet in a fluidic PJ nozzle is presented in Figure 1.12 (Nathan et al. 1998).

The parameters that characterize the flow field of a PJ are: the thermodynamics properties such as the kinematic viscosity υ, the bulk velocity, the jet precession frequency f_p, the nozzle diameter d, and the inner diameter D and length L of the cylindrical chamber. The following four non-dimensional groups can be addressed as governing parameters St_p, Re_d, $\frac{D}{d}$ and $\frac{L}{D}$, where the first reads as

$$St_p = \frac{f_p d}{V_j} \qquad 1.4$$

In the early work conducted by Hallett and Gunther (1984) and Dellenback et al. (1988), the precession was induced by an upstream swirl motion imparted at the inlet flow. Hallett and Gunther (1984) performed experiments on a chemical reactor model with an expansion ratio of D/d=2.2, they observed a precessing motion at low swirl number. The precession of the flow was triggered for swirl intensities lower than that required for the formation of the CRZ. Dellenback et al. (1988) conducted experimental investigations on a water flow at Reynolds number ranging between 30,000 and 100,000 and a swirl number from zero to 1.2. They deduced that at low swirl intensities the flow field was axisymmetric with a recirculation bubble located on the axis of the chamber, while increasing the swirl intensity the flow on the centreline followed the same direction as the mean flow and the recirculation bubble was located on the periphery of the axis.

Nathan (1988) in his Ph.D. thesis investigated the effect of an abrupt expansion on axisymmetric jets, showing that an upstream swirl is not required to promote a precessing motion. In particular, his research was focused on the determination of the optimal nozzle geometry, in terms of D/d and L/D, which guaranties a more reliable precessing motion. Considering a jet flow issuing from the orifice into the cylindrical chamber (Figure 1.12), it was found that the optimal PJ nozzle geometry ensures the largest spreading and decay rate of the jet flow. From flow visualization experiments and pressure measurements, Nathan (1988) found out that the optimum was reached at D/d=6.4 and L/D=2.7. In cold flow conditions, the spreading angle of the half jet was 70° and the entrainment increased by a factor 2 with respect to a free axisymmetric orifice jet.

Since the generated flow field within the cylindrical chamber produces a precessing jet at its exit, this large scale mechanism determines a natural oscillation that appeared interesting for combustion applications. In this context, Nathan (1988) found that the length of the flame was shorter than that produced by an axisymmetric flame at the same geometric and fluid-dynamic parameters. This features leaded to a commercialized device, under the name *Gyro-therm*®, patented by the University of Adelaide and applied in rotary kilns.

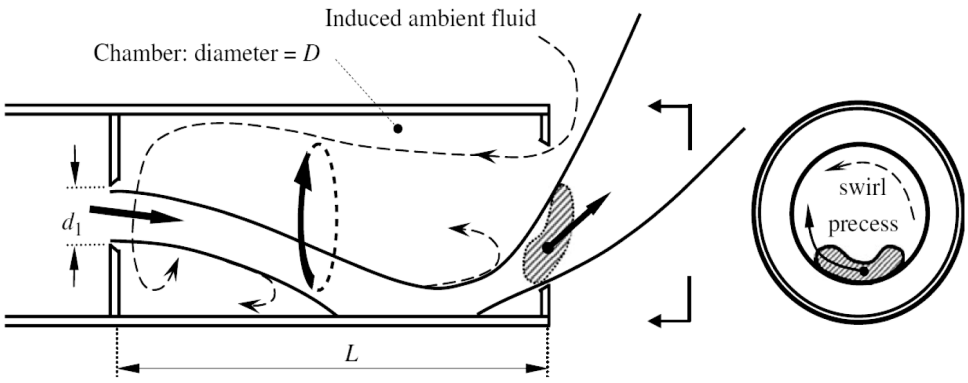

Figure 1.12 Geometry of a fluidic precessing jet nozzle and schematic representation of the interaction between the precessing jet and the entrained fluid (Nathan et al. 1998).

1.2.1 Flow characteristics of precessing jets

The naturally generated PJ flow can be bundled among the different complex class of bifurcating flow instabilities related to that naturally generated in symmetrical configurations without any initial bias (Battaglia 1997). Since the PJ phenomenon is generated by a fluid-dynamic instability, an intermittent bi-stable behaviour, represented by two modes, a PJ mode and an axial jet AJ mode, have been observed. The description of the phenomenology of the PJs has been provided by Nathan et al. (1998). In their work, particular emphasis was placed upon the evidence that the inlet flow was symmetric without any initial bias to avoid influence of residual or induced swirl within the chamber. In addition, the fluidic PJ nozzle tested by Nathan et al. (1998) was equipped by an exit lip in order to promote the precession of the jet by deflecting it towards the axis of the chamber. The flow field switched between the PJ and AJ modes as testified by the visualization of the instantaneous pathlines of the two modes depicted in Figure 1.13, obtained by capturing the light scattered from air bubbles seeding the flow. In the AJ mode, the flow does not exhibit an asymmetric reattachment, the jet is located on the axis of the cylindrical chamber and interacts with the lip, determining the occurrence of a wide recirculation region in the periphery of the jet characterized by large-scale coherent structures. In the PJ mode, the flow field is characterized by a continuously unstable reattaching jet with a recirculation region on the opposite side of the chamber. An asymmetric and rotating pressure gradient within the chamber is established with an asymmetric entrainment process that moves upstream within the chamber and swirls in the opposite direction to that of precession. This leads to a net angular momentum equal

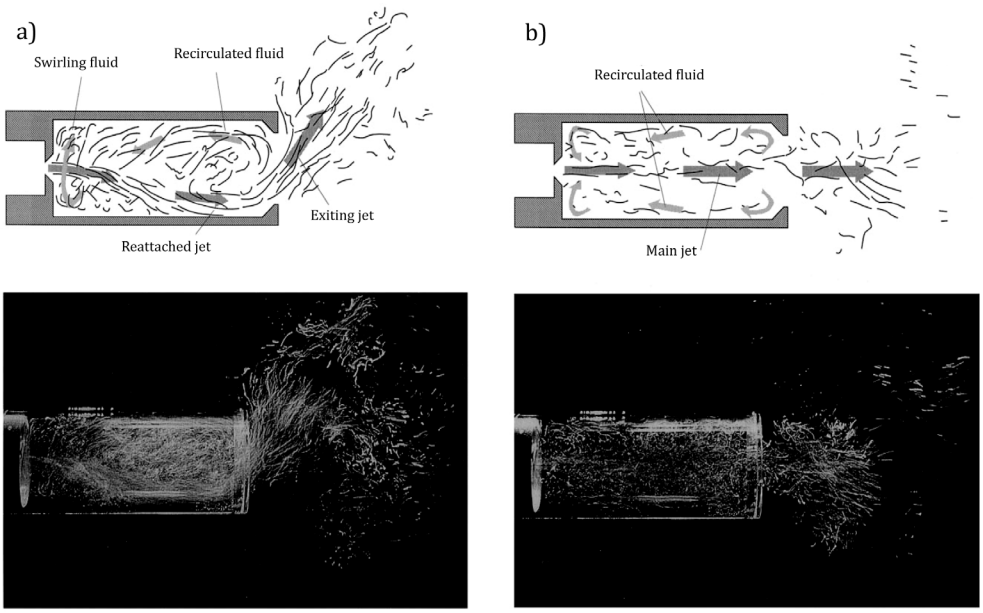

Figure 1.13 Schematic interpretation (top) and water flow visualization (bottom) of the instantaneous pathlines in the precessing jet (a) and axial jet (b) modes (Nathan et al. 1998).

to zero, this aspect is also illustrated in Figure 1.12. The combination of the entrainment effect and the emerging jet attached to the wall determines the presence of an additional pressure gradient at the exit of the PJ nozzle (Wong, 2004).

The probability with which the PJ mode occurs is a function of the nozzle geometry and the Reynolds number (Nathan 1988, Nathan et al. 1998, Wong et al. 2004, Madej et al. 2011). However, it is possible to enhance the PJ mode probability by selecting nozzle configurations equipped with a centrebody, firstly introduced by Nathan (1988), as described by Wong et al. (2003).

The flow within the chamber results to be complex, 3D and unsteady and also influenced by the inlet conditions. Wong et al. (2004) used an orifice plate, smooth contraction and a pipe to improve the PJ mode probability. As reported by Nathan et al. (2006), the key features of the flow within the chamber lie on the organization of the large-scale reverse flow zone and the induced swirl upstream of the chamber. From phase-averaged LDA measurements of the axial velocity component, Wong et al. (2003) investigated the internal and external flow field of a fluidic PJ nozzle equipped with a centrebody and an exit lip; a sketch of such a nozzle configuration, termed as chamber-lip-centrebody configuration, is illustrated in Figure 1.14. Inside the chamber, they identified

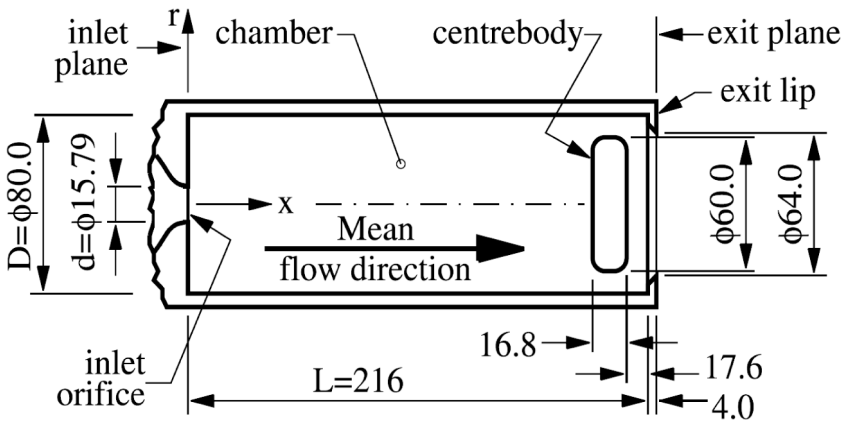

Figure 1.14 Sketch of the chamber-lip-centrebody configuration (Wong et al. 2003).

two regions of forward and reverse flows, implying the presence of a large-scale recirculation region. The intensity of the reverse mean flow was found to be about 30% of the forward axial velocity. The external flow is characterized by an emerging jet with a profile on the cross-sectional exit plane more like a distorted ellipse, also referred to as 'banana-shaped' zone (many aspects on the topology of a PJ flow field results to be similar to swirling flows). In addition, the emerging jet exhibits a phase-averaged deflection angle of 50° at the exit of the chamber and, further downstream, decreases down to 30° at 0.4 chamber diameters from the exit. Nathan et al. (2006) reported the presence of two streamwise vortices, both in the internal and external flow field, which are embedded within the shear layer and characterized by different vorticity intensities consistent with the precessing motion. In this context, Kelso (2001) proposed a model of precession in which these coherent structures have a leading role on the development of the jet precession. It was based on the superposition of a steady contribution, i.e., reattachment of the jet to the chamber wall, and an unsteady one, i.e., the response of the pattern under an infinitesimal perturbation of the reattachment point in steady condition. The model has been developed from many observations of fluidic PJ flows (Nathan, 1988) and based on phase-averaged measurements (Wong et al. 2003). The comparison with the experimental data indicates strong agreement with the model, but how the precessing motion is related with the instantaneous coherent structures embedded in the shear layer of the curved jet still has not been clearly understood.

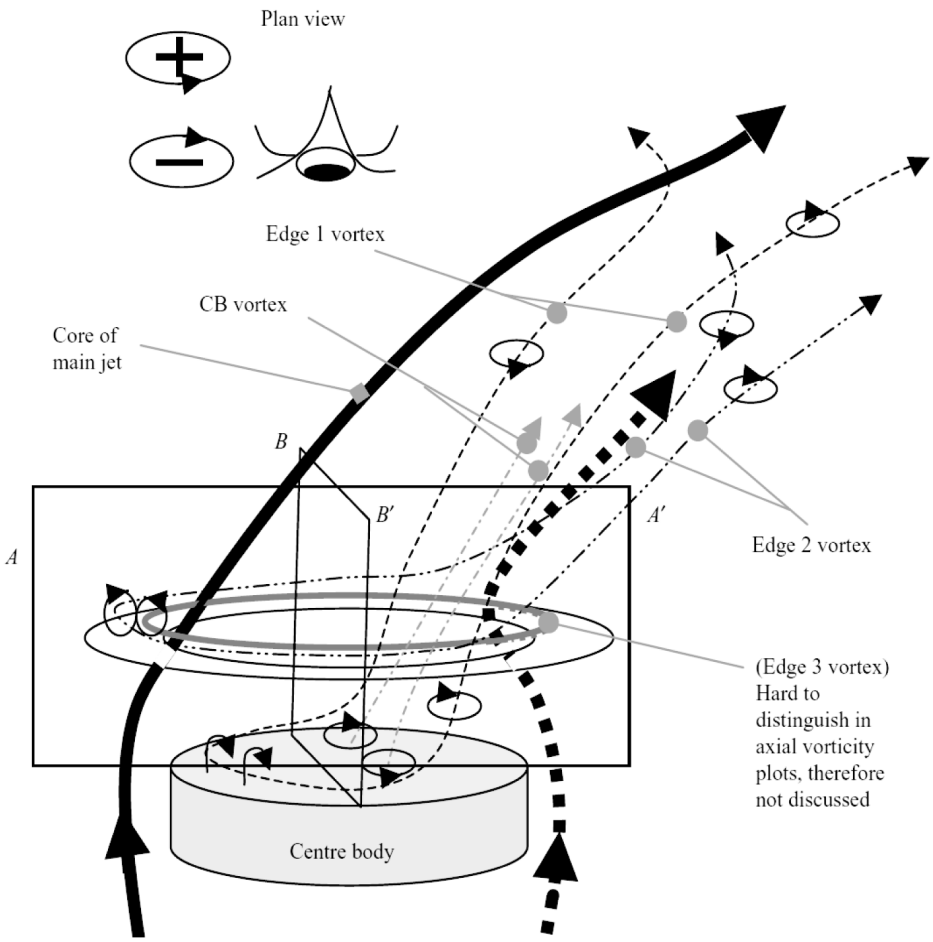

Figure 1.15 The interpretation of the flow emerging from the fluidic PJ nozzle investigated by Wong et al. (2008). Diagram is not in scale and extracted from Wong et al. (2008).

The flow field organization within the cylindrical chamber of a fluidic PJ nozzle (without the presence of the exit lip) was presented by Cafiero et al. (2014) using tomographic PIV experimental technique (see Section 2.2). They educed, using a low order reconstruction of the flow field (see Section 2.3.2), the interaction between the entrainment of the external fluid and the recirculation region in the lower part of the chamber. This interaction determines a swirling motion that penetrates into the shear layer of the inlet jet and produces instantaneously two helical vortices.

An investigation on the flow field at the exit of a PJ device in chamber-lip-centrebody configuration (Figure 1.14) were performed by Wong et al. (2008) at Reynolds and Strouhal numbers equal to 59,000 and 0.0017, respectively. They interpreted from phase-

averaged and directionally triggered particle image velocimetry the flow features downstream of the centrebody for the deflected jet. Figure 1.15 present a comprehensive schematic diagram of the flow topology of the precessing jet. The core of the emerging jet is represented by the thickest line, while the emerging fluid characterized by an averaged weaker velocity (Wong et al. 2003) is indicated with the thick-dotted line. Averaged vortex regions, marked with thinner lines, refer to maximum vorticity patterns. They also identified pair of vortices originating from the surface of the centrebody, indicated in Figure 1.15 by dash-dot-dashed lines. Their results indicated that the azimuthal component of the emerging jet is in opposite direction to that of the jet precession.

1.2.2 The effect of the geometry and Re_d on the precession probability

Even though in the early work by Nathan (1988) the optimal geometric configuration of a fluidic PJ nozzle that promotes the precession motion was at D/d=6.4 and L/D=2.7, several later studies were conducted on devices with fixed expansion ratio of D/d=5 with the purposes to investigate the effects of the Reynolds number, geometry and aspect ratio L/D on the precession probability (Nathan et al. 1998, Madej et al. 2011, Wong et al. 2004).

Nathan et al. (1998) calculated the precession probability from pressure measurements at the wall or from the signal of a total pressure probe at the jet axis using the probability distribution function. By varying the Reynolds number Re_d and remaining with a fixed aspect ratio at L/D=2.75, the precession probability increases with the Reynolds number, as shown in Figure 1.16. In addition, comparing their results with respect to that reported by Hill et al. (1992) fluidic precessing nozzles with larger expansion ratio, ranging between 3.3<D/d<5.7, are more favourable to promote the precessing motion.

In a later study, Madej et al. (2011) conducted stereoscopic PIV experiments (see Section 2.1.3) at the exit of a fluidic PJ nozzle with D/d=5 and no exit lip. By varying the Reynolds number (ranging between 10,000<Re_d<61,900) and the aspect ratio, they evaluated the precession probability using three different criteria to identify the PJ mode, based on the location of the maximum outflow velocity, centroid location of the volume flow rate and volume flow beyond a cut-off radius. The results from each approach lead to a relatively low uncertainty on the determination of the PJ mode. Thus, Figure 1.17 shows the PJ mode probability as a function of the aspect ratio at different Re_d. In the case of L/D=1, the flow does not exhibit a precessing motion. Between 2<L/D<2.75, the PJ

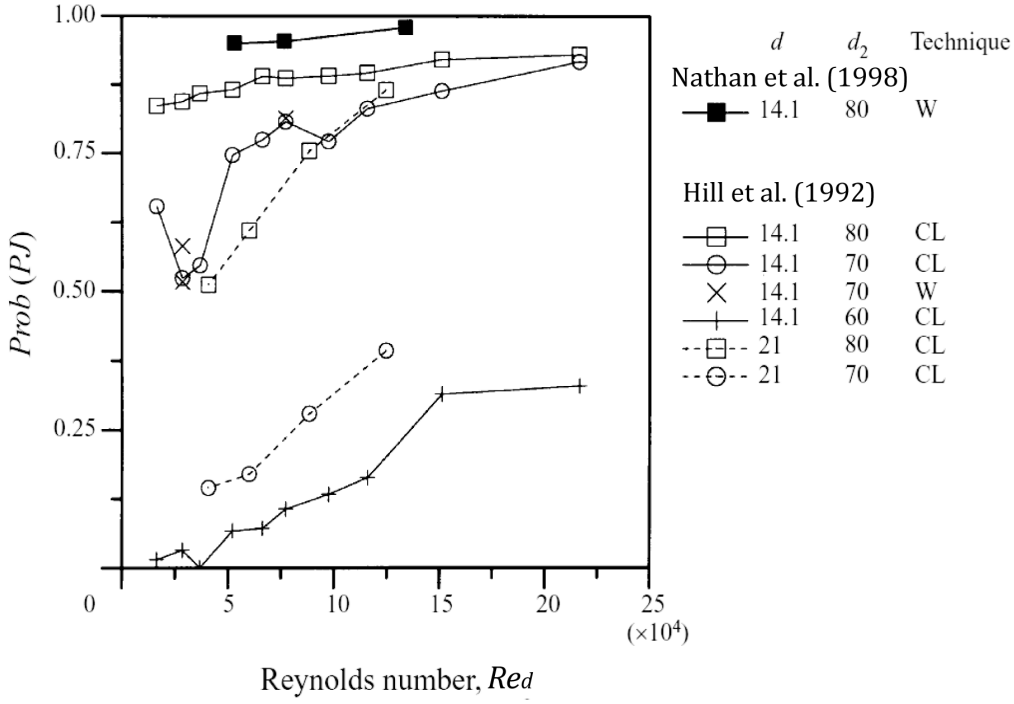

Figure 1.16 Precession probability, *Prob(PJ)*, as a function of the Reynolds number Re_d evaluated by Nathan et al. (1998) and compared with that reported by Hill et al. (1992). The experimental methods were based on pressure measurements at the wall (W) or the signal from a total pressure probe at the jet axis (CL) (adapted from Nathan et al. 1998).

mode is promoted and increases its probability with the Reynolds number. At L/D=3, the probability dramatically drops down and then slightly increases for larger aspect ratios.

In order to provide a more reliable precessing motion, Nathan (1988) introduced an insert within the chamber near the exit of the fluidic PJ nozzle, opening the possibility to stabilize the flow patterns at much shorter aspect ratio. However, using flow visualization the resulting patterns exhibited features similar as observed when no insert was installed. More recently, an improved version of the fluidic PJ nozzle is obtained by installing a centrebody along the centerline of the chamber as shown in Figure 1.14. This configuration ensures about the 100% probability of precession at sufficiently large Reynolds numbers (Wong et al. 2004).

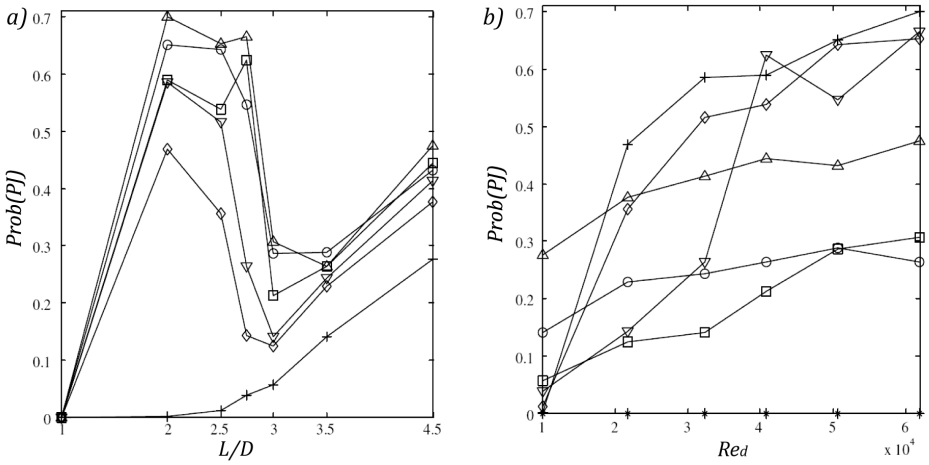

Figure 1.17 Precession probability Prob(PJ) as a function of the aspect ratio L/D (a) and Reynolds number Re_d (b). On the left, + Re_d=10,000, ◇ 21,800, ▽ 32,4002, □ 40,800, ○ 50,700, △ 61,900. On the right, * L/D=1.0, + 2.0, ◇ 2.5, ▽ 2.75, □ 3.0, ○ 3.5, △ 4.5 (adapted from Madej et al. 2011).

1.3 Oscillation mechanism in PJ flows and PVC in swirling flows

In the review work by Syred (2006), a description of PVC phenomenology has been comprehensively provided and a comparison between PJ flows and PVC in swirling flows has been discussed starting from the physical evidence that both phenomena occur naturally within axisymmetric inlet and boundary conditions (Nathan et al. 2006). However, the main difference relies on the fact that PVC is generated by a flow with a significant azimuthal velocity component, while the PJ flow is a natural precessing motion without requiring, in principle, an initial swirl. On the other hand, a common feature is that both types of flow are originated from a fluid-mechanical instability; Nathan et al. (2006) underlined that the coupling between a vortex shedding and an acoustic resonance does not produce PVCs and PJ flows. In particular, Selle et al. (2006) pointed out that a PVC is generated by a hydrodynamic instability testified by the evidence that it was found to be present also in cold flow condition, where coupling with acoustic modes does not occur. However, in reacting conditions the confined swirling flame is rather comprised of a rotating acoustic mode.

The fact that the fluidic PJ oscillation is not caused by an acoustic generation has been conclusively verified in the early work by Nathan (1988). Investigations, using both the same experimental apparatus and Strouhal number St_p, were conducted in water and air in order to achieve Mach numbers differing by a factor of 70. The results indicated that at

different Mach numbers the flow field exhibited rather the same features. Nathan et al. (2006) reasoned that this behavior discards the possibility of an acoustic coupling since it requires a matching between the frequency of a hydrodynamic instability, such as vortex shedding frequency, and an acoustic resonant mode related to the geometry of the pipe or the chamber (Mugridge 1980, Candel 1992). Indeed, the wavelength of resonance is fixed by the physical dimension of the device, λ_r, and the resonant frequency is controlled by both this dimension and the speed of sound, $f_r=c/\lambda_r$. Whereas, the shedding frequency is independent by the speed of sound being controlled by the Strouhal number, $St=fd/V_j$. Thus, if a dramatic change of the Mach number occurs, any acoustic coupling achieved for a fixed operating condition is lost. Furthermore, they also stated that the precession frequency f_p is directly proportional with the flow rate (Nathan 1988, Nathan et al. 1998) and its instantaneous value scatters significantly about the expected value at fixed operating conditions.

In combustion applications, measuring the Strouhal number associated with the precessing motion is of fundamental importance for the determination of the PJ nozzle operating conditions respect to the features of the PJ flow field in terms of level of mixing in the region where the flame is located. Nathan (1988) introduced, for a fluidic PJ nozzle, a different definition of Strouhal number $St_h= f_p h/V_j$ where $h=(D-d)/2$ is the step height, noting best collapses of the data and enabling an easy comparison with Strouhal numbers characteristics of other flow phenomena described in literature. However, the common definition reported in literature corresponds to the (1.4) and its characteristic value for a fluidic PJ nozzle is about 0.002 (Nathan et al. 2006). Mi and Nathan (2004) investigated the influence of the chamber length and the Reynolds number on the precession frequency from total pressure measurements at the nozzle axis. They observed that St_d increases rather linearly with both the chamber length and the flow rate. Furthermore, the enhancing of the mixing at the exit of the PJ nozzle results to be more sensitive with the former, indeed, the Strouhal number of the emerging flow is an order of magnitude higher than that within the nozzle, but an order of magnitude lower than the vortex shedding within the shear layer of the inlet jet.

A greater understanding on the mixing characteristics of the external flow can be quantified using mechanical precessing jet nozzles, MPJ nozzles (Schneider et al. 1997a and 1997b). A schematic of a MPJ nozzle is sketched in Figure 1.18. This nozzle has the unquestionable advantage over a fluidic PJ nozzle of enabling independently the control of

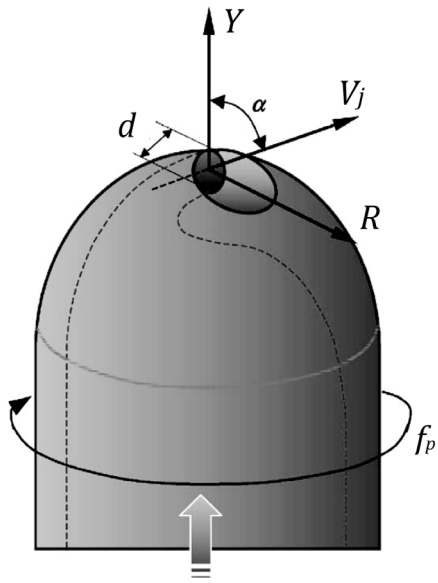

Figure 1.18 Schematic of the mechanical precessing jet nozzle (adapted from Mi and Nathan 2004).

the rotational frequency, the flow speed and the dimension of the exit diameter. On the other hand, it results to be not suitable for applications in combustion where the harsh environment can compromise the structural integrity of the rotating parts. Depending on the St_d and the exit angle, Schneider et al. (1997b) identified two classes of flow regimes separated by a value of a 'critical' Strouhal number, introduced by Mi and Nathan (2005), $St_{d_{crit}}$=0.008 for an exit angle equal to α=45°. For $St_d<St_{d_{crit}}$, the emerging jet is located on the wall of the chamber presenting, in averaged sense, features similar to that detected for a fully bifurcating jets (Reynolds et al. 2003). Conversely, for $St_d>St_{d_{crit}}$ the flow tends to deflect towards the axis of rotation.

Chapter 2

Particle Image Velocimetry

This chapter is devoted to the description of the fundamentals of planar PIV and tomographic PIV techniques. A description of the data reduction methods used in the present work, i.e., vortex identification criteria and proper orthogonal decomposition, is also outlined.

2.1 Fundamentals of planar PIV

Particle image velocimetry (PIV, Raffel et al. 2007) is an non-intrusive anemometric technique for velocity field measurements. The principal characteristic is its ability to measure the instantaneous velocity field simultaneously at different points with a spatial resolution that permits to extract flow field information as vorticity and rate of strain ((Westerweel et al. 2013). A basic PIV experimental setup with the working principle is sketched in Figure 2.1.

The pulsed light source is collimated in a light sheet that illuminates the investigated region (object plane) of a fluid seeded by tracer particles. The pulsed light is separated by an adjustable time delay Δt with pulse duration short enough, <10 ns, to assume frozen the scattered particles imaged onto an image plane using a camera (for example a high resolution digital camera). The optical axis of the camera is set perpendicular to the light sheet within the alignment tolerances. The particles are selected to follow the acceleration within the flow field with high accuracy and to scatter efficiently the light in order to capture clearly particle images. Typically, aerosol particles of a diameter of about 1 μm are used in gas flows and solid particles of diameter of about 10 μm are homogeneously dispersed in water flows. The scattered particles imaged onto the image plane can be stored on a single-frame (double exposure) or on two separate frames (single exposure). The recorded images determine the direction of the motion of the particles by dividing each frame into small interrogation regions (often referred to as 'windows'); the displacement of the particle images in each interrogation region is measured using statistical methods: auto-correlation in the case of double-exposure (Adrian and Yao 1984) or cross-correlation in the case of single exposure images (Willert and Gharib 1991).

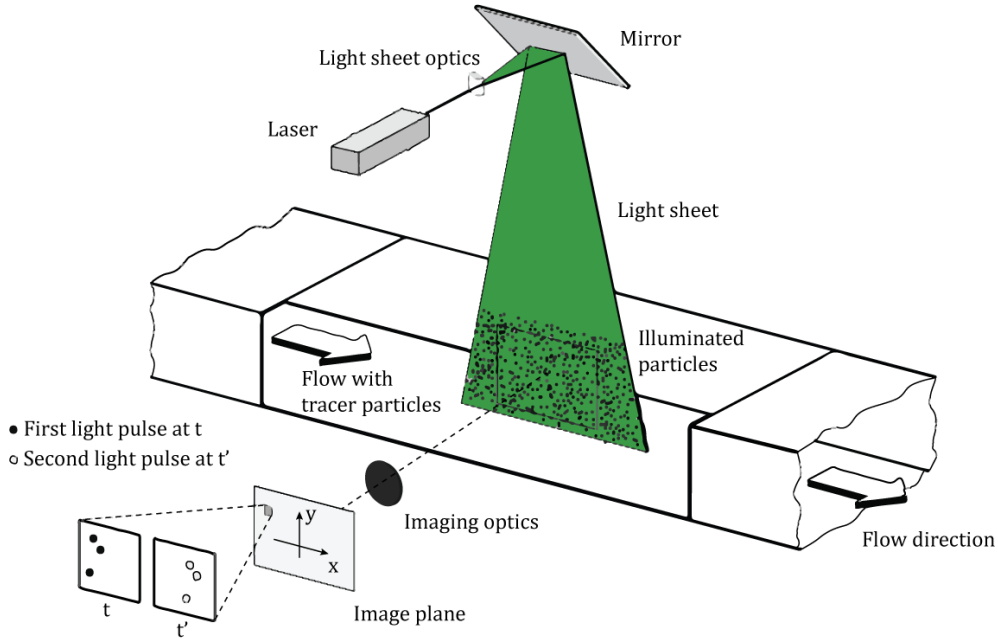

Figure 2.1 Sketch of a basic PIV experimental setup (adapted from Raffel et al. 2007).

The maximum correlation gives the mean displacements of the particles image, Δx and Δy, residing in the volume produced by the intersection of the interrogation domain and the light sheet. The estimation of the velocity components in the physical plane, i.e., U and V, is computed in agreement with the relation

$$\binom{U}{V} = \frac{1}{M_0 \Delta t}\binom{\Delta x}{\Delta y}, \qquad 2.1$$

where M_0 is the lateral magnification from the object plane to the image plane; it is defined as the ratio of the image distance (between the imaging optics and the sensor plane) to the object distance (between the imaging optics and the object plane).

2.1.1 Particle imaging

The particle images are formed on the sensor of the camera (in the following, Charge Coupled Device CCD and Complementary Metal-Oxide Semiconductor CMOS sensors are used) via high quality imaging optics. A simplified expression for the particle image diameter d_τ, considering the effects of the particle size and the lens properties, is (Adrian, 1991)

$$d_\tau \approx \sqrt{d_{geom}^2 + d_{diff}^2} = \sqrt{\left(M_0 d_p\right)^2 + (2.44 f_\# (1 + M_0)\lambda_L)^2} \qquad 2.2$$

where d_{geom} is the geometric image diameter due to the magnificationd_{diff}, is the diffraction-limited diameter by approximating the Airy disk with a Gaussian function, d_p is the particle physical diameter, $f_\#$ is defined as the ratio of the focal length and the aperture diameter and λ_L is the wavelength of the illuminating source.

It is crucial that the particles are imaged in focus ensuring that the sensor area covered by the particles is minimized for a given amount of particles. In particular, a smaller d_τ enhances the quality of the measurements by reducing the uncertainty in the measured displacement (Raffel et al. 2007) and ensuring strong light intensity (the light intensity detected by the sensor scales with the inverse of the particle image area); on the other hand, reducing d_τ can determine a detrimental effect, i.e., the bias of the correlation peak towards integer pixel values, referred in literature as 'peak-locking' (Westerweel 1993).

The condition that ensures the particles are imaged in focus is that the focal depth δz should be larger or equal to the thickness of the light sheet ΔZ_0. According to the diffraction optics (Adrian, 1991), the optical focal depth reads as

$$\boldsymbol{\delta} z \approx 4.88\lambda_L f_\#^2 \left(1 + \frac{1}{M_0}\right)^2. \qquad 2.3$$

The source density N_s, defined as

$$N_s = C\Delta Z_0 \frac{\pi d_\tau^2}{4M_0^2} \qquad 2.4$$

where C is the particles concentration, features the quality of the recorded images. In case of N_s<1, the image is composed of randomly located individual spots with a small probability to detect overlapped particles, otherwise, they generate randomly oriented pattern of fringe due to the coherent nature of the light source (typical in PIV applications laser light is used as light source).

2.1.2 Data processing

Since the recorded images are characterized by a large image density so that the use of particle identification schemes suffers in case of overlapping particles, statistical methods devoted to evaluate the particle displacement are required. Correlation technique (either auto-correlation and cross-correlation) are suitable to comply with this purpose.

The image is divided in interrogation windows. For each selected interrogation window, I_a and I_b are the pixel intensities of both exposures at the image plane locations x and y; the normalized cross-correlation coefficient R_{corr} is determined by

$$R_{corr}(\Delta x, \Delta y) = \frac{\sum_{x,y}^{L_I}(I_a(x,y)-\mu_a)(I_b(x+\Delta x,y+\Delta y)-\mu_b)}{\sqrt{\sum_{x,y}^{L_I}(I_a(x,y)-\mu_a)^2 \sum_{x,y}^{L_I}(I_b(x+\Delta x,y+\Delta y)-\mu_b)^2}} \quad 2.5$$

where μ_a and μ_b are the mean intensities of the interrogation windows, L_I is the size of the square interrogation window.

The location of the peak in the cross-correlation map represents the most likely mean displacement of the particles within the interrogation window. Since the diffraction-limited spot is approximately Gaussian, it is possible to assume that the correlation peak resulting from convolution of Gaussian filter is Gaussian as well. Thus, by fitting the correlation map with Gaussian or similar function has demonstrated to reach sub-pixel accuracy in case of small particle images (Raffel et al. 2007).

In order to improve the accuracy and the robustness of the statistical method, strategies using interrogation window with different size (Adrian, 1991) or multi-pass cross-correlation with discrete windows offset (Westerweel 1997) or with windows deformation (Huang et al. 1993) have been developed.

2.1.3 Stereoscopic PIV

As already outlined, the planar PIV measures only two components of the velocity field (2D-2C), thus requiring the need of assumptions to infer three-dimensional (3D) information on the spatial organization of coherent structures in turbulent flows. Taking advance of the out-of-plane motion of the particles through the illuminated light sheet, the third component of the velocity field could be inferred if another simultaneous measurement is available from a different point of view, i.e., using two-cameras system in stereoscopic arrangement (Figure 2.2). Indeed due to the finite depth of the light sheet, a particle imaged on the cameras comes from the planes within the region $|Z - Z_p| < \Delta Z_0/2$. Assuming (X_p, Y_p, Z_p) is the particle location in the physical space, the components of the image displacement vector read as (Raffel et al. 2007)

$$\begin{pmatrix}\Delta x_p \\ \Delta y_p\end{pmatrix} = M_0 \begin{pmatrix}\Delta X_p \\ \Delta Y_p\end{pmatrix} + M_0 \begin{pmatrix}X_p/Z_p \\ Y_p/Z_p\end{pmatrix} \Delta Z_p \quad 2.6$$

where ΔX_p, ΔY_p, ΔZ_p are the components of the physical displacement vector and Δx_p, Δy_p, Δz_p are the components of the image displacement vector. The system (2.6) with two

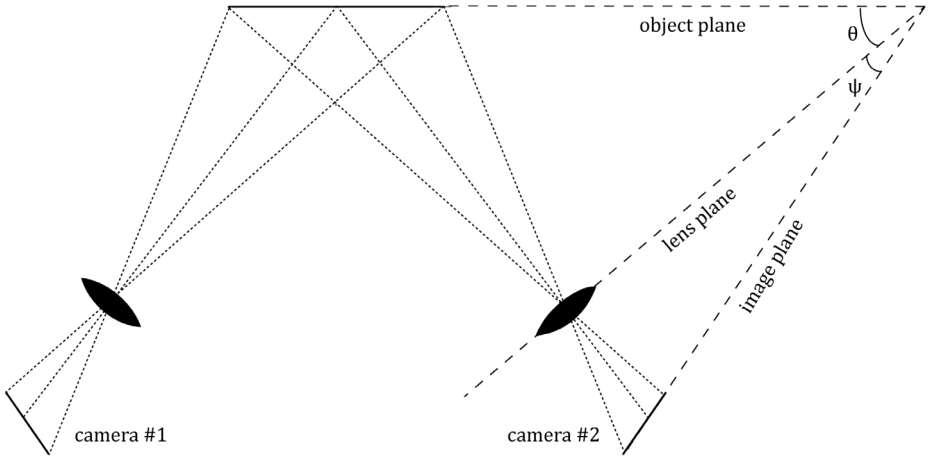

Figure 2.2 Stereoscopic PIV arrangement with angular lens displacement complying with the Scheimpflug condition (Raffel et al. 2007).

equations per camera in three unknowns can be resolved using the information acquired by the stereoscopic camera system.

In Figure 2.2, the stereoscopic PIV arrangement with a rotational lens system is depicted; the requirement that the object plane, the lens plane and the image plane have to be collinear (Scheimpflug condition) allows to obtain well-focused particle images over the field of view. This arrangement optimizes the lens performance by reducing the viewing angle of the optical setup. However, the magnification is no longer uniform because the rotational system complying with the Scheimpflug condition exasperates the gradient of the line of sight along the image plane (Raffel et al. 2007).

2.2 Tomographic PIV

Tomographic PIV (Tomo-PIV) was introduced as a promising method for measuring instantaneous 3D velocity field (Elsinga et al. 2006). This leads to an unambiguous interpretation of the spatial organization of the coherent structures arising in turbulent flows (Scarano and Poelma 2009, Violato and Scarano 2011) and provides all the nine component of the velocity gradient.

The working principle of Tomo-PIV relies on the reconstruction of a 3D distribution of scattered light coming from tracer particles homogeneously dispersed into a control volume. The reconstruction is achieved by analysing the projections of these scattering

objects imaged simultaneously by multiple cameras oriented along different viewing directions. The computed distribution of the light intensity is discretized in fundamental cubic supports named 'voxels', which are the volumetric equivalent of pixels. The three-components of the velocity vector within the volumetric measurement domain is then computed by 3D cross-correlation of the reconstructed volume. The schematic of the working principle of the technique is sketched in Figure 2.3.

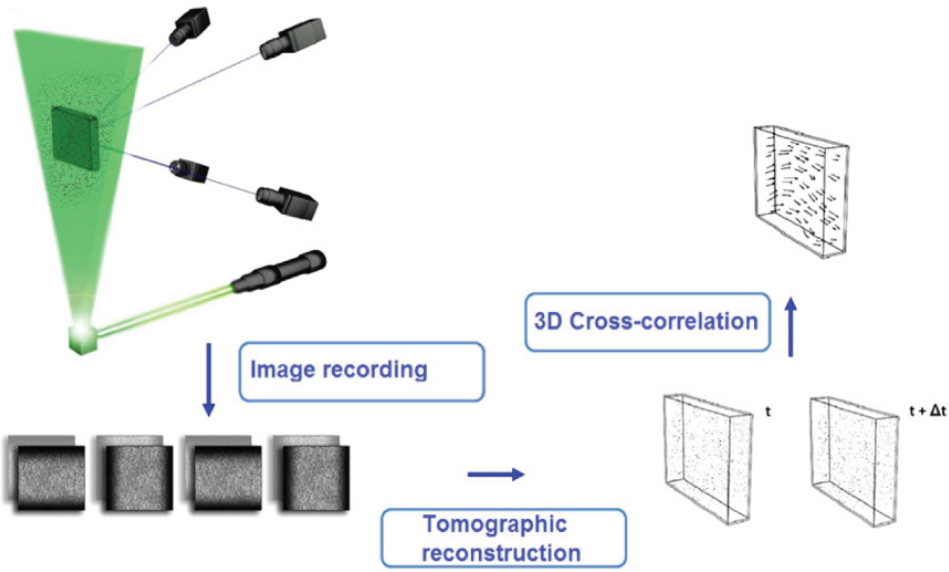

Figure 2.3 Schematic of the working principle of tomographic PIV (adapted from Elsinga et al. 2006).

2.2.1 System calibration

Since the tomographic reconstruction is based on a correspondence between the 3D space (X, Y, Z) and the image plane (x, y), calibration-based methods, determining a mapping function M_i (Willert 1999, Prasad 2000), are required. Considering a point in the physical space $P = (X, Y, Z)$, its projection onto the image plane of the ith camera is $p_i = (x, y)$,

$$(x_i, y_i) = M_i(X, Y, Z) \qquad 2.7$$

Generally, the calibration procedure consists of recording images of a target with high-contrasted markers located at known physical position and mechanically translated along the depth direction to encompass a volume in which the illuminated region is enclosed. Several studies have dealt with the determination of the mapping functions (Prasad, 2000), the most adopted calibration models are the pinhole camera model (Tsai,

1987) and the third order polynomial interpolating functions (Soloff et al. 1997). In the following, the pinhole camera model is adopted for the precessing jet measurements (Section 3.3.2). It is based on six extrinsic parameters, i.e., a translation vector and three Euler angles, and six intrinsic parameters, i.e., pixel aspect ratio, radial distortion factor describing the effect due to the distortion caused by the lenses, focal length and image coordinates intersection of the optical axis and the image plane. For the swirling jet measurements, the third order polynomial interpolating function is applied (Section 3.2.2).

2.2.2 Volume self-calibration

It is crucial for a successful reconstruction of the 3D particle field to reduce any misalignment larger than a fraction of the particle image diameter (Elsinga et al. 2006). Indeed, the 3D particle field reconstruction by tomography requires that the lines of sight corresponding to particle imaged by all the cameras are precisely intersecting (Scarano 2013). Under realistic experimental conditions, this correspondence has to be achieved through the optical calibration described in Section 2.2.1. However, Tomo-PIV imaging systems suffer of uncertainties due to the mechanical stability camera holders, thermal variation within the cameras, vibration introduced by its cooling system or by surrounding sources.

An iterative process for detecting and, subsequently, reducing the misalignment for 3D measurements has been devised by Wieneke (2008) (volume self-calibration). The technique is based on locating the particle in the individual images and their 3D position through triangulation. The residual local disparity obtained by the statistical estimation of the most probable relative offset between the projection of each particle and the correspondent positions on the camera images is used to correct the mapping functions. Figure 2.4 shows the triangulation procedure, it is worth to note that the application of this method works quite easily on low density images (particle image density below to 0.1 ppp).

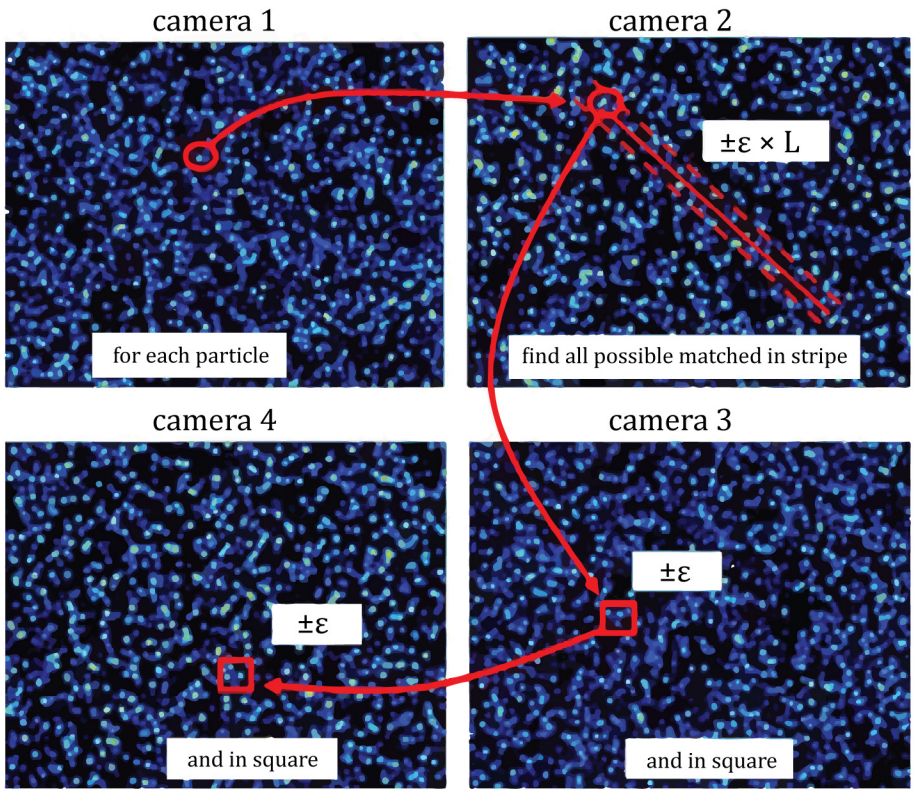

Figure 2.4 Particle triangulation procedure for the volume self-calibration technique (adapted from Wieneke 2008).

2.2.3 Volume reconstruction

A novel approach introduced with the Tomo-PIV is the reconstruction of the 3D particle distribution by optical tomography. The 3D intensity distribution of the light scattered by the tracer particles $E(X,Y,Z)$ is represented by an array of voxels discretizing the physical space (Figure 2.5); while, the intensity values recorded on the camera images constitutes the set of projections $I(x_j, y_j)$ at a position corresponding to the jth pixel (x_j, y_j). In the hypothesis of superposition effects, the line integrals of the intensity along the line of sight are discretized as a weighted sum of voxel intensities

$$I(x_j, y_j) = \sum_{k=1}^{N_{vox}} w_{j,k} E(X_k, Y_k, Z_k) \qquad j = 1, \dots, N_{pix} \qquad 2.8$$

where N_{vox} and N_{pix} are the number of voxels that contributes to the image intensity and the number of pixels, respectively; $w_{j,k}$ is a weighting coefficient determining the influence of the intensity of the kth voxel on the intensity recorded on the jth pixel. The (2.8)

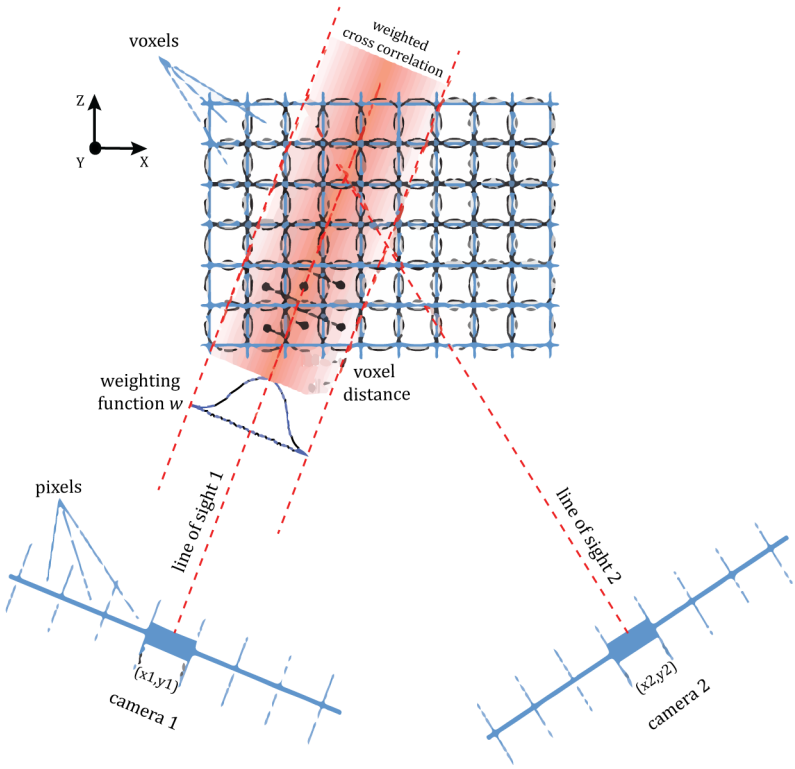

Figure 2.5 2D representation for the tomographic reconstruction with two 1D cameras. The weighting coefficients are non-zero within the shaded region. Spherical shape of the voxels simplifies the calculation of the weighting coefficients (Scarano 2013).

results in an undetermined problem of a linear system characterized by N_{pix} equations with N_{vox} unknowns ($N_{pix} > N_{vox}$).

A possible approach to determine a solution of (2.9) is the Multiplicative Algebraic Reconstruction Technique (MART, Herman and Lent 1976)

$$E_{n+1}(X_k, Y_k, Z_k) = E_n(X_k, Y_k, Z_k)\left(\frac{I(x_j, y_j)}{\sum_{k=1}^{N_{vox}} w_{j,k} E(X_k, Y_k, Z_k)}\right)^{\mu_M w_{j,k}} \qquad 2.9$$

where the subscript n indicates the current iteration and μ_M is a scalar relaxation parameter related to the stability of the iterative process (for the MART method it ranges $0 < \mu_M < 1$). Furthermore, the MART scheme requires that E and I are definite positive.

The 3D intensity fields reconstructed by MART are typically affected by several types of errors due to the ambiguity in the estimation of the correct position of the particles along the line of sight. As outlined by Novara et al. (2010), these artefacts can be classified

in three categories: discretization errors, geometrical errors and ghost particles (Maas 1993).

Discretization errors are due to under-sampling of signal, i.e., when the diameter of the particles to be reconstructed is smaller than 2-3 pixels. Discetti et al. (2013) pointed out that the discretization procedure produces a Gaussian shape of the particles because of their diffraction limited spot; as a consequence, the reconstructed particles should have Gaussian shape as well. The discretization errors can be reduced by applying a Gaussian filter in the iterative process of equation (2.9), increasing the reconstruction accuracy.

Geometrical errors occur when the solid angle subtended by the viewing directions of the cameras is too small; this results in an elongation of the reconstructed particle in the depth direction, determining an increment of the random errors in the measurement of the velocity component along the depth. This effect can be compensated by orienting the cameras at an optimum angle approximately of 30° (Scarano 2013).

Ghost particles are intensity blobs forming at the intersection of the line of sight with non-zero values, but not corresponding to the position of actual particles. The formation of the ghost particles relies on the non-uniqueness of the solution of the reconstruction problem (2.9). This source of error can be reduced by increasing the number of cameras, reducing the seeding density and using advanced reconstruction schemes.

2.2.4 Ghost particles

The ghost particles constitute a limiting effect for tomographic measurements when a limited number of cameras records tracer particles at high concentration.

A ghost particle is formed when the lines of sight corresponding to actual particles imaged on all the cameras intersect at a point in the reconstructed domain. Following Discetti (2013), a simple model to predict amount of ghost particles N_g with respect to the number of actual particles N_p can be formulated considering an illuminated volume of depth ΔZ_V and two-cameras PIV system. A particle image of the first camera can be located anywhere along the line of sight, whose length is of the same order of ΔZ_V (the effect of the viewing angle is neglected). The possible candidates for the matching of a single particle of the first camera on the second camera are enclosed in a strip with length equal to the projection of the line of sight on the second camera, i. e., epipolar line (it can be estimated by multiplying ΔZ_V for the average magnification M_0 and by dividing the pixel pitch P_p) and width equal to the particle image diameter d_τ. A statistical estimation

of the number of matching for each particle image of the first camera with the second camera can be determined by multiplying this area for the particle image density.

A general formulation for N_{cam} cameras system reads as

$$\frac{N_g^{N_{cam}}}{N_p} = \left(N_{ppp}\right)^{N_{cam}-1} d_\tau \left(\frac{\Delta Z_V M_0}{P_p}\right)\left(\frac{\pi {d_\tau}^2}{4}\right)^{N_{cam}-2} = \frac{4}{\pi d_p}\left(N_s\right)^{N_{cam}-1}\Delta Z_V M_0 \qquad 2.10$$

where N_{ppp} is the particle image density, $\Delta Z_V M_0 / P_p$ represents the depth of the volume in voxels and $\pi d_\tau / 4$ is the diameter of the particle image.

In practical cases, the number of ghost particles may exceed that of the actual particles. On the other hand, the intensity of a ghost particle seldom reaches that of actual particles and if the particle images do not triangulate exactly at the same point, the energy of a potential ghost particle remains low without compromising the velocity field measurement.

In case of flow field characterized by velocity gradient (e.g. shear/mixing layer regions), it is possible to reduce the detrimental effect of the ghost particles. Novara et al. (2010) introduced a novel method that takes advance of the information included at two or more different time instants for the tomographic reconstruction. The method is based on an iterative procedure in which a preliminary motion analysis is performed: the first guess distributions of the two (or more) exposures are reconstructed by MART and, subsequently, cross-correlation is performed. According to the velocity field, the first guess distribution are deformed in order to obtain two versions of the object with the same distribution of the actual particles and an altered distribution of the ghost particles. These objects are then summed in order to obtain an enhanced guess distributions from which MART can be applied again. In the following, the combination of MART algorithm and MTE process is applied to enhance the accuracy of the volume reconstruction for the present data (see Section 3.3.3).

2.2.5 3D motion analysis

The 3D velocity field is computed by cross-correlation of the two reconstructed intensity field with the knowledge of the magnification factor and the time separation Δt between the exposures. The measurement domain is divided into box-like sub-volumes (extension to 3D of the interrogation windows) and then the 3D cross-correlation function (obtained by extension to 3D of the (2.5)) is used to evaluate the particle displacement.

In this work, the 3D velocity field is evaluated by the following algorithm, whose skeleton has been summarized in Discetti (2013):

1. 3D cross-correlation is computed on a rather coarse grid in order to obtain a predictor displacement field. The interrogation spot size complies with the one-quarter rule introduced by Keane and Adrian (1992);
2. A volume deformation approach is applied by interpolating the predictor displacement field on each voxel;
3. Reduction of the interrogation spot size is executed since the volume deformation compensates the loss of pairs;
4. A corrector displacement field is calculated on the deformed volumes;
5. The final displacement is obtained by summing the corrector and a weighted average of the dense predictor at a prescribed region.

The steps 2-5 are repeated till the convergence. Since the multi-grid volume deformation approach (VODIM, Scarano and Poelma 2009) introduces high computational burden, development of more robust PIV interrogation algorithms is required. Discetti and Astarita (2012b) have recently proposed a new efficient algorithm combining the multi-resolution interrogation concept (Discetti and Astarita 2012a) with sparse data storage, cross-correlation and interpolation for the calculation of the 3D velocity field without any significant loss of accuracy. This efficient 3D PIV interrogation algorithm is used for the flows studied within this thesis.

2.3 Data reduction

2.3.1 Vortex-identification criteria

The availability of volumetric measurements of the 3D velocity field enables more advanced flow diagnostic possibilities. The main advance compared to the planar PIV relies on the simultaneous evaluation of the velocity vector $\underline{V}$ and the velocity gradient tensor $\underline{\nabla}\,\underline{V}$ within a measurement domain over the three coordinate directions.

An intuitive method for educing coherent structures relies on the analysis of the vorticity vector field $\underline{\omega} = \underline{\nabla} \wedge \underline{V}$ or its norm. As pointed out by Jeong and Hussain (1995), this approach does not identify vortex cores in shear flows characterized by vorticity magnitude within the vortex core comparable with that in the surrounding shear. Most widely methods for vortex identification define a function that can be evaluated point-by-point, classifying each point as being inside or outside a vortex. These local vortex identification criteria are based on the kinematics, i.e., on the analysis of the velocity

gradient tensor $\underline{\nabla}\,\underline{V}$ in its symmetric (strain rate tensor $\underline{\underline{S}}$) and antisymmetric (vorticity tensor $\underline{\underline{\Omega}}$) part. Hunt et al. (1988) introduced a method to identify vortices into an incompressible flow as connected fluid regions with a positive second invariant of $\underline{\nabla}\,\underline{V}$. The Q-criterion reads as

$$Q = \frac{1}{2}\left(\left\|\underline{\underline{\Omega}}\right\|^2 - \left\|\underline{\underline{S}}\right\|^2\right) > 0, \qquad 2.11$$

that is, regions where the vorticity magnitude prevails over the strain-rate magnitude. Additionally, the pressure in the vortex core has to be lower than the ambient pressure. The norm operator $\left\|\underline{\underline{F}}\right\|$ of any tensor $\underline{\underline{F}}$ is defined as $\left\|\underline{\underline{F}}\right\| = \sqrt{tr\left(\underline{\underline{F}}\,\underline{\underline{F}}^T\right)}$. Interesting enough, the Q>0 does not guarantee the condition of minimum pressure inside the detected region (Jeong and Hussain 1995). In the present study, the Q-criterion is applied without the additional pressure condition. Jeong and Hussain (1995) formulated a vortex identification method based on dynamic considerations for incompressible flows. Considering the well-known vorticity and strain-rate transport equations and discarding the unsteady irrotational straining and viscous contributions, the λ_2-criterion is defined as the occurrence of a local pressure minimum in a plane across the vortex. Thus, a vortex is defined as a connected fluid region with two negative eigenvalues of $\left\|\underline{\underline{\Omega}}\right\|^2 + \left\|\underline{\underline{S}}\right\|^2$. The λ_2-criterion was introduced from the observation that the identification of vortices based on local pressure minima fails in unsteady flows with strong viscous effects (Jeong and Hussain, 1995). Furthermore, the main difference between these two approaches is that, while the Q-criterion takes into account the excess of the rotation rate over the strain rate in all directions, the λ_2-criterion measures this excess only on a plane perpendicular to the axis of the detected vortex.

Figure 2.6 shows an application of the three presented vortex identification methods on present Tomo-PIV data. The case study is a swirl flow produced by a sudden expansion of a jet flow passing through a double-radial swirl-burner for aeronautical application; the terms of the velocity gradient tensor are evaluated from present Tomo-PIV data. Chapter 4 gives a broader discussion on the spatial organization of these helical vortex structures.

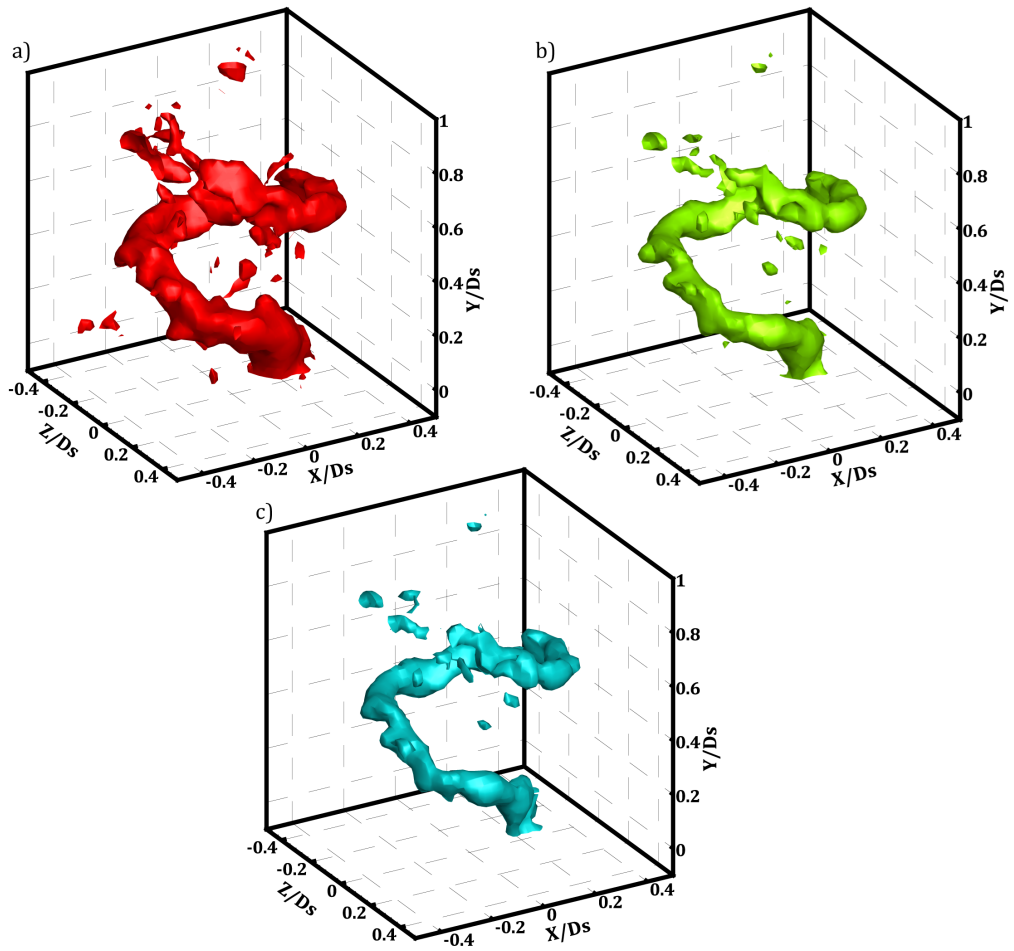

Figure 2.6 Helical vortex structure; vortex visualization using $|\underline{\omega}|$ (a), Q-criterion (b) and λ_2-criterion (c) (present data).

2.3.2 Proper orthogonal decomposition

The proper orthogonal decomposition (POD) is a mathematical procedure that identifies an orthonormal basis using functions estimated as solutions of the integral eigenvalue problem known as Fredholm equation (see Sirovich (1987) for a rigorous formulation). Berkooz et al. (1993) have shown that the POD represents a powerful technique to extract relevant information about the coherent structures in turbulent flows. Consider a function (e.g. a velocity field) $\underline{V}(\underline{x},t)$ that is approximated as

$$\underline{V}(\underline{x},t) = \overline{\underline{V}(\underline{x},t)} + \underline{v}'(\underline{x},t) = \overline{\underline{V}(\underline{x},t)} + \sum_{b=1}^{N_m} a_b(t)\underline{g}_b(\underline{x}) \qquad 2.12$$

where $\underline{x}$ and t are the spatial and temporal coordinates, respectively; the overbars indicate the operation of ensemble averaging. The functions $\underline{g}_b(\underline{x})$ constitute the decomposition basis of the fluctuating velocity field $\underline{v}'(\underline{x},t)$; $a_b(t)$ are the time coefficients. The symbol N_m indicates the number of modes used to decompose the velocity field. The solution is not unique as it depends on the chosen basis functions $\underline{g}_b(\underline{x})$. The snapshots method proposed by Sirovich (1987) assumes that the POD modes are calculated as the eigenmodes of the two-point temporal correlation matrix $\underline{\underline{R}}$,

$$\underline{\underline{R}}\underline{g} = \lambda \underline{g} \tag{2.13}$$

where $R_{i,j} = \overline{\underline{v}'(\underline{x}_i, t) \cdot \underline{v}'(\underline{x}_j, t)}$. Since $\underline{\underline{R}}$ is a non-negative Hermitian matrix, it has a complete set of non-negative eigenvalues, whose magnitude indicates the energy contribution of the respective eigenmodes.

Ben Chiekh et al. (2004) introduced a procedure to reconstruct the flow field in the case of shedding-dominated velocity fields. The technique, referred to as low order reconstruction LOR, is based on approximating the sum of (2.12) with only the first two modes, representing the shedding contribution:

$$\underline{V}(\underline{x},t) = \overline{\underline{V}(\underline{x},t)} + \underline{v}'(\underline{x},t) \approx \overline{\underline{V}(\underline{x},t)} + a_1(\varphi)\underline{g}_1(\underline{x}) + a_2(\varphi)\underline{g}_2(\underline{x}) \tag{2.14}$$

The coefficients $a_1(\varphi)$ and $a_2(\varphi)$ are phase terms; they are related to the shedding phase angle and, consequently, are not independent:

$$a_1(\varphi) = \sqrt{2\lambda_1}\sin(\varphi) \tag{2.15}$$

$$a_2(\varphi) = \sqrt{2\lambda_2}\cos(\varphi) \tag{2.16}$$

where λ_1 and λ_2 are the first two eigenvalues obtained by the POD. It can be demonstrated that the low order representation corresponds to the basic Fourier component of the flow field ensemble with respect to the reconstructed phase (Van Oudheusden et al 2005).

Chapter 3

Experimental instrumentation and arrangement

This chapter is devoted to the description of the facility, the experimental instrumentations and the technical solutions adopted for the setup of a reliable apparatus used for the experimental investigation. The chapter also includes a characterization of the inlet conditions of the fluidic PJ nozzle.

3.1 Design of the jet flow facility

Tomographic PIV experiments are conducted in the water jet facility at the Gasdynamic Laboratory of the University of Naples "Federico II". The jet flow facility has been designed to enable extensive optical access of the illumination and tomographic imaging; a similar water tank was previously developed by Violato (2013). The jet is installed at the bottom wall of a tank, shaped as a non-regular nonagonal prism, of circumscribed diameter of 640 mm and height of 720 mm. The mainframe of the tank is made of *Plexiglass® GS 233*, that has been chosen for its suitable surface quality and its index of refraction relatively close to that of water. Furthermore, *Plexiglass®* is transparent in the spectral band of wavelengths of the visible light, enabling the possibility to investigate the flow field by means of the PIV technique. The schematic in Figure 3.1 shows the jet flow facility and a cross-section of the settling chamber**.** Stabilized water supply is provided using a centrifugal water pump (1) manufactured by IRCEM water pumps. The model is 2004 PP4M providing a maximum power of 1.5 kW. The operating regime of the water centrifugal pump is controlled by means of an industrial inverter TOSVERT™ VF-S11 manufactured by TOSHIBA for 3-phase induction motors. Subsequently, the flow rate is measured by means of a flow meter (2) with a maximum flow rate equal to 6.9 kg/s and accuracy of ±0.1 kg/s. A multi-point point water injection system (3) provides an unbiased distribution of the stream at the inlet of the settling chamber (4) of inner diameter of 100 mm and length of 400 mm. In order to reduce free stream turbulence anisotropy, the flow passes through a series of honeycomb and grids (5) fitted into the settling chamber. This system along with the nozzle holder (6) guides the flow into the nonagonal water tank (7). A closed loop circuit is completed by a siphon at the top of the tank, providing the water to the centrifugal pump.

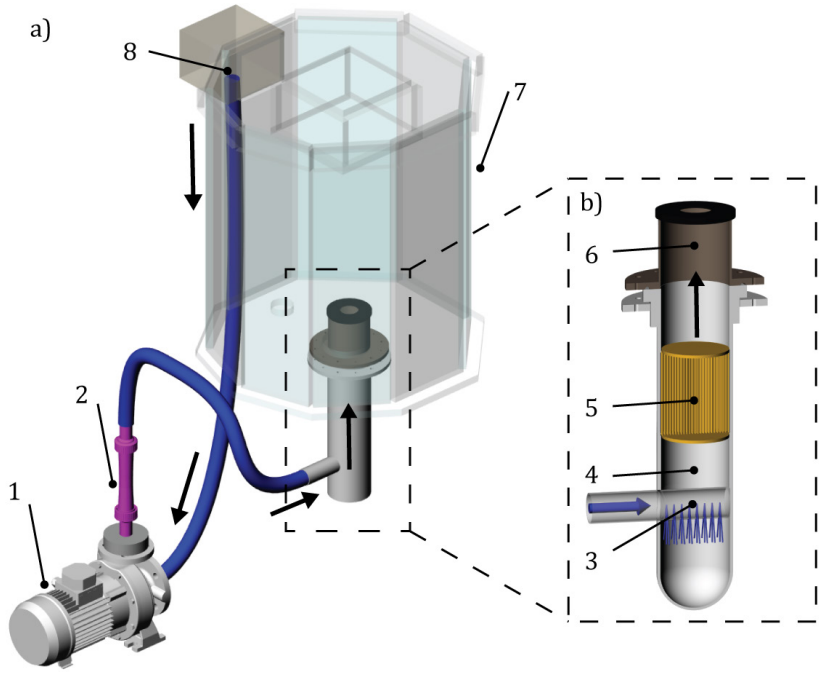

Figure 3.1 Schematic view of the jet flow facility (a) and cross-section of the settling chamber (b); centrifugal pump (1), flow meter (2), multi-point water injection (3), settling chamber (4), honeycomb and grids (5), nozzle holder (6), nonagonal water tank (7) and siphon (8). The arrows indicate the flow direction of the water.

3.2 Swirling jet experiment

The experiments are carried out on a lean pre-vaporized premixed LPP injector for aero-engine applications. The LPP injector with an exit diameter D_S equal to 40 mm, designed by GE AVIO S.r.l., is installed on the nozzle holder of the jet flow facility (Figure 3.1). In Figure 3.2, the flow coming from the settling chamber passes through two radial co-swirl generators and, subsequently, two co-swirl flows pass through a central circular nozzle of diameter of 0.63 D_S and a surrounding annular nozzle of outer diameter of D_S. The pilot fuel injector guide is clogged for all experimental conditions in order to investigate the flow field generated only by the swirl generators.

Experiments are conducted in two different test conditions: free and confined outflow. In the latter case, the swirling jet is confined in a *Plexiglass*® cylindrical chamber with inner diameter equal to 3 D_S. Both experiments are performed with a flow rate equal to about 2.0 kg/s, corresponding to a bulk velocity V_j equal to about 1.6 m/s. This yields a fixed Reynolds number $Re_{D_s} = V_j D_s/\nu$ of 64,000.

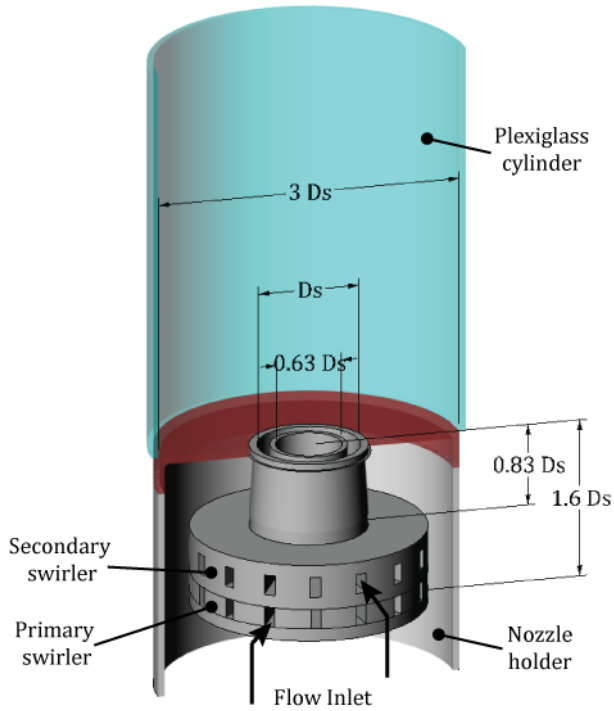

Figure 3.2 Details of the LPP injector: double radial swirler and cross-section of the nozzle holder with the *Plexiglass*® cylindrical chamber.

3.2.1 Tomographic PIV measurements

Neutrally buoyant polyamide particles of 56 μm median diameter are homogeneously distributed in order to achieve a uniform concentration approximately of 0.3 particles/mm^3. Laser pulses are produced with a double-cavity Gemini PIV Nd:YAG system (532 nm, 200 mJ/pulse at 15 Hz, 5 ns pulse duration). The exit beam of 5 mm diameter is shaped into a parallelepiped volume using a three lenses system, i.e., a diverging and a converging spherical lens (with focal length equal to -75 mm and 100 mm, respectively), and a diverging cylindrical lens (with focal length equal to -50 mm); a knife edged mask is placed along the laser path in order to suppress the tails of the Gaussian beam profile and also achieving a volume thickness equal to 46 mm (Figure 3.3). The light scattered by the particles is recorded by a tomographic system composed of four LAVision Imager sCMOS 5.5 megapixels cameras (2560 x 2160 pixels resolution, pixel pitch 6.5μm, 16 bit). The cameras are equipped with 100 mm EX objectives, set at $f_{\#}$=16. Lens-tilt adapters are installed between the image plane and lens plane. Well-focused particle images are achieved throughout the volume by aligning the focal plane with the mid-plane

TOMO PIV		
Seeding particles	Diameter [μm]	56
	Concentration [particles/mm^3]	0.3
Volume illumination	Thickness [mm]	46
Recording devices	4 LAVision Imager sCMOS (2560 × 2160pixels@10Hz)	
Optical arrangement	EX objectives (f_L [mm], $f_\#$)	100, 16
	Field of view [D_s^2]	3.4 × 3.4
Magnification		0.1
Acquisition frequency	[Hz]	10
Pulse separation	[μs]	150
Number of recordings		500

Table 3.1 Experimental parameters for the swirling jet experiment.

of the measurements domain (Scheimpflug condition). The schematic of the illumination and imaging setup of the experiments is sketched in Figure 3.4. Particle image density obtained for chosen illumination and imaging configuration is about 0.05 particles/pixel. The average magnification in the centre of the measurement volume is approximately 0.1 corresponding to a spatial resolution of about 18 pixels/mm, resulting in a depth of field of 62 mm and particle image diameter of 3.7 pixels (Westerweel et al. 2013). The details of the experimental settings are summarized in Table 3.1. Sequences of 500 couple of images are captured with acquisition frequency of 10 Hz with time separation of 150 μs. The particle displacement detected on the image plane at nozzle exit is approximately of 10 pixels. The field of view is set up to 3.2 D_S along the jet axis, corresponding to approximately 120 mm, in order to provide a field investigation of the vortices organization. A schematic of the measurement domain and the reference frame is shown in Figure 3.5.

Figure 3.3 Pictures of the setup: tomographic experimental apparatus during the calibration procedure (left); camera arrangement: four 5.5 megapixels cameras LAVision Imager sCMOS.

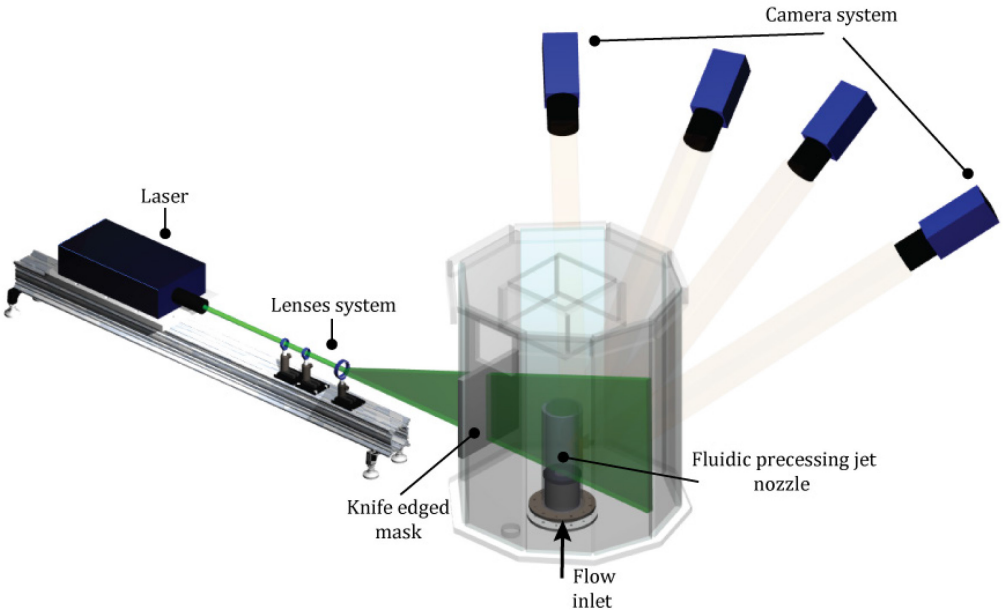

Figure 3.4 Schematic view of the illumination and imaging setup of the experiments.

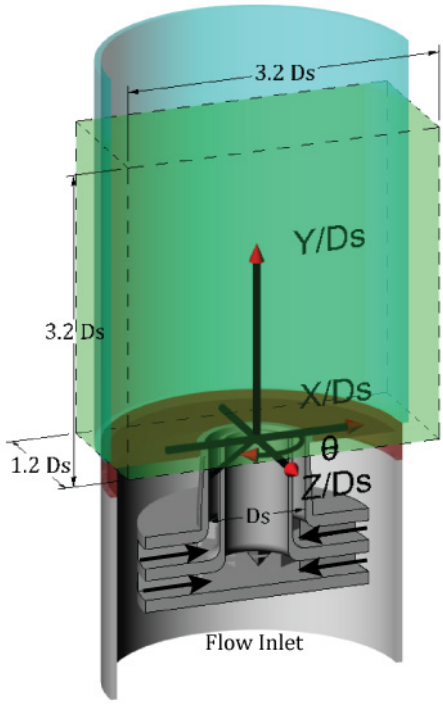

Figure 3.5 Measurement domain and reference frame; cross-section of the LPP injector.

3.2.2 Calibration procedure

The measurement domain is calibrated such that an accurate relation is found for the physical coordinates in the measurement volume to image plane coordinates (see Section 2.2.1 for details). A calibration procedure is performed using a LAVision double/plane target (shown in Figure 3.6) imaged at five Z-locations covering the entire measurement domain (±23 mm). The 3D mapping functions are generated using a 3rd order polynomial function in X and Y, and 2nd order in Z with a root mean square rms calibration error equal to about 0.3 pixels. The calibration error is reduced up to 0.05 pixels by means of volume self-calibration technique (Wieneke, 2008). For both the experiments, the calibration is performed without the presence of the cylindrical chamber due to physical access restrictions. The challenge is to correct the mapping functions reducing the misalignment of the lines of sight induced by the optical distortions across the interface between water and the cylindrical chamber. Despite of the very similar values of refraction index of water and *Plexiglass*® the optical distortions can cause significant

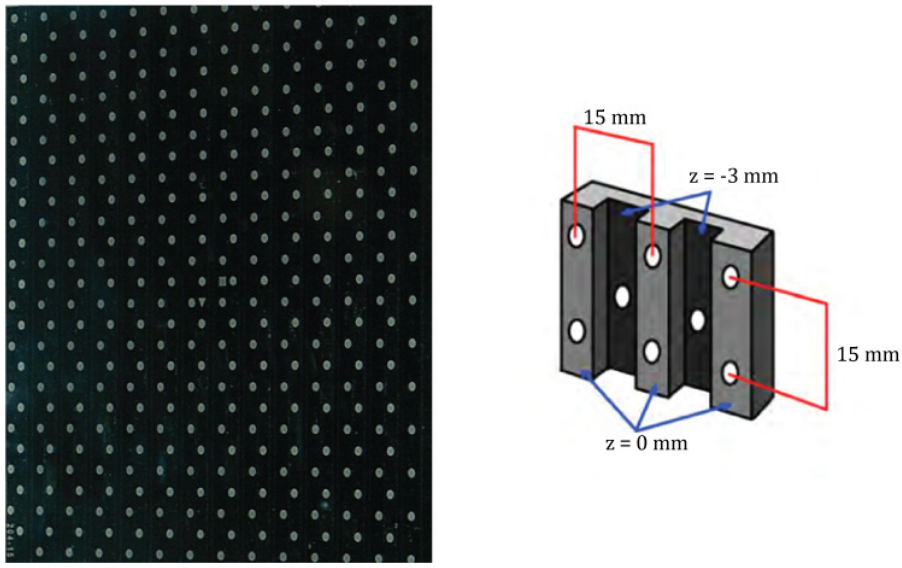

Figure 3.6 LaVision calibration target geometry.

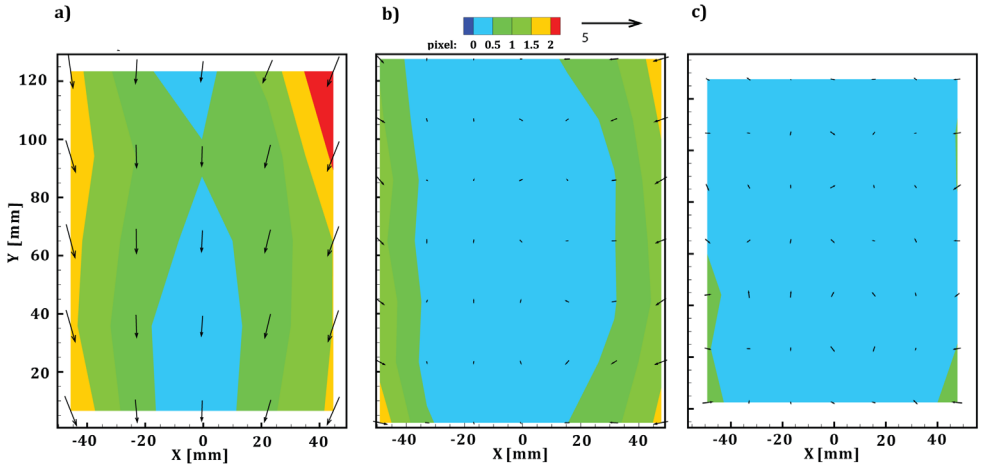

Figure 3.7 Iso-contour with displacement vectors of the calibration error of a camera for three subsequent (a, b and c) self-calibration corrections.

errors (up to about 3 pixels) because the viewing angle on the cylinder surface varies across the image.

The volume self-calibration technique (Wieneke, 2008) is applied: the corrections are obtained through ensemble average on 200 images. The maps of the iso-contour of the rms calibration error related to a front camera are show in Figure 3.7 for three

subsequent self-calibration corrections. After the self-calibration procedure, the rms of calibration error is reduced up to 0.07pixels.

3.2.3 Tomographic reconstruction

The background intensity on the raw images is eliminated by subtracting the historical minimum based on the acquired sequence of 500 images. Subsequently, a residual fluctuating background is removed applying a sliding minimum subtraction over a kernel of 31 × 31 pixels in space and using 5 samples in time.

The volumetric light intensity reconstruction is performed combining the MLOS technique with the CSMART algorithm (10 iterations) by LAVision software Davis 8. The illuminated volume of 3.2 × 3.2 × 1.2 D_S^3 (i.e. 130 × 130 × 46 mm^3) is discretized with 2298 × 2298 × 1004 voxels (18 voxel/mm). The reconstruction quality is improved by filtering the reconstructed distributions in between each iteration using a Gaussian filter ((Discetti et al. 2013).

The sum of the intensity of the reconstructed particles on XY planes has been calculated in order to assess the accuracy of the reconstruction. In Figure 3.8, the intensity of the reconstructed particles with respect to the Z direction is shown for free and confined configuration. The signal/noise is about 2, being acceptable for three dimensional velocity measurements.

The 3D particle field motion is computed with the LAVision software Davis 8 software; the interrogation algorithm is based on a direct sparse cross-correlation approach as proposed by Discetti and Astarita (2012). The final interrogation volume is of 64 × 64 × 64 voxels (3.5 × 3.5 × 3.5 mm^3) with an overlap between adjacent interrogation boxes of 75%, leading to a vector pitch of 0.8 mm. The measurement uncertainty is evaluated considering the local mass conservation in the incompressible regime, as applied for the precessing jet measurements. The standard deviation of the divergence computed on raw data is about 7% of the typical value of the vorticity magnitude within the shear layer (0.24 voxels/voxel, equivalent to 1.6 × 10^3 s^{-1}).

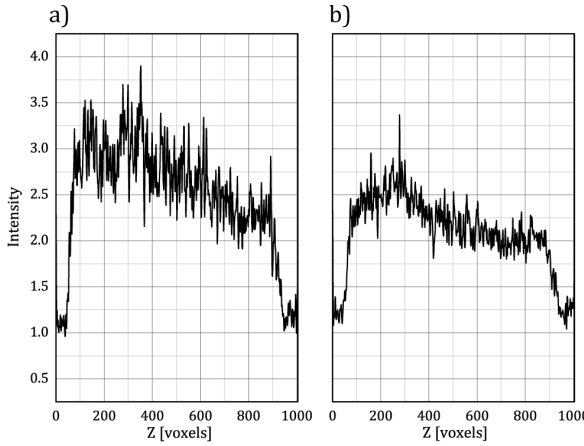

Figure 3.8 Intensity profile in the XZ (depth) plane: free (a) and confined (b) experimental configuration.

3.3 Precessing jet experiment

The jet issues through a short-pipe nozzle with diameter d=20 mm and length 6.2d installed on the nozzle holder of the jet flow facility. The jet expands with a step-like inflow condition into a cylindrical chamber coaxial with the nozzle (diameter D=100 mm, length L=275 mm, so that, D/d=5 and L/D=2.75; see Figure 3.9 for details of the nozzle geometry). The cylindrical chamber is made of *Plexiglass*® in order to ensure a full optical access. While in many investigations an exit lip (Nathan et al. 1992) and/or a centrebody (Wong et al. 2003) have been included into the chamber to favor the precessing motion and to condition the exit angle, in this study these arrangements are not considered in order to assess the topology of the flow field without external forcing.

Tomographic PIV measurements are performed for two inflow conditions by using either simply a short-pipe nozzle (jet without grid JWG) or placing a regular grid (RG) at the nozzle exit (Figure 3.9). The mesh-length of the regular grid is equal to 2.4 mm, while the bar thickness is 0.4 mm. The bulk velocity V_j of the fluid entering the chamber is about 2.12 m/s corresponding to a Reynolds number $Re_d = V_j d/\upsilon$ of ~42,500, where υ is equal to 10^{-6} m^2/s. For these experimental conditions, the precessing mode is expected to be prevalent on the axial mode, indeed, Madej et al. (2011) indicated a probability more than 60% of precessing motion for Re_d=40,800, in geometrical conditions of D/d=5 and L/D=2.75.

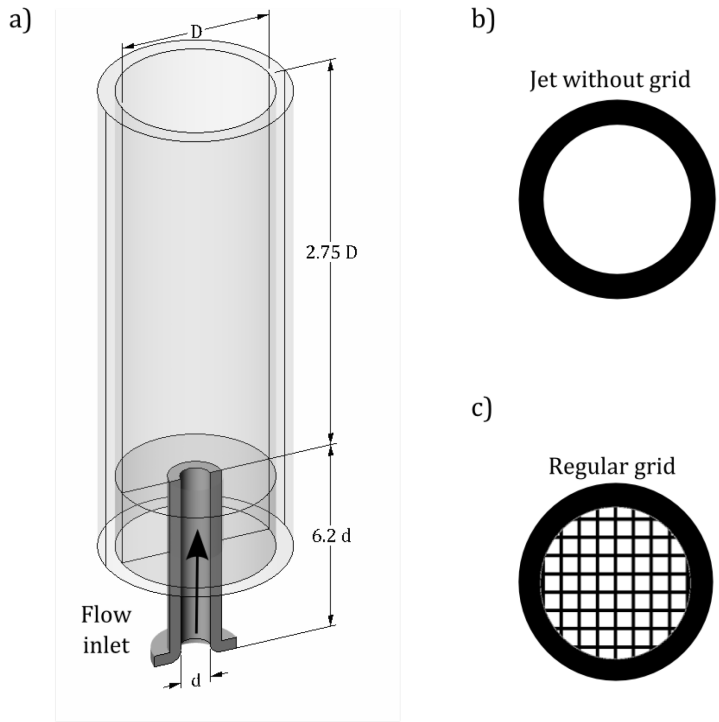

Figure 3.9 Details of the fluidic precessing nozzle (a); jet without grid JWG (b) and regular grid RG (c) placed at the nozzle exit.

3.3.1 Tomographic PIV measurements

The flow is seeded with neutrally buoyant polyamide particles, already used for the swirling jets experiment (Section 3.2.1), homogeneously dispersed into the circuit upstream of the centrifugal pump. The illumination is provided by a Quantel Evergreen laser for PIV applications (light wavelength equal to 532 nm, 200 mJ/pulse at 15 Hz, <10 ns pulse duration) with an exit diameter of about 5 mm. The laser beam is shaped into a parallelepiped volume using the optical arrangement already presented in Section 3.2.1 (Figure 3.4), except for the knife edged mask that is re-contoured in order to set the volume thickness to 27 mm. The light scattered by the particles is recorded by a tomographic system composed of four Andor sCMOS 5.5 Mpixels cameras (pixel pitch 6.5 μm) arranged horizontally with azimuthal aperture of 90°, and diagonally tilted in order to prevent spurious reflections of the laser light on the *Plexiglass*® wall of the cylindrical chamber. Because of the parallelepiped shape of the illuminated volume, a camera lens tilt mechanism is used to comply the Scheimpflug condition. Tokina 100 mm macro objectives are set at $f_{\#}$=16 in order to allow focused imaging of the illuminated particles.

TOMO PIV		
Seeding particles	Diameter [μm]	56
	Concentration [particles/mm^3]	0.68
Volume illumination	Thickness [mm]	27
Recording devices	4 Andor sCMOS 5.5 Mpixels cameras (2560 × 2160pixels)	
Optical arrangement	Tokina objectives (f [mm], $f\#$)	100, 16
	Field of view [D^2]	1 × 1.07
Magnification		0.1
Acquisition frequency	[Hz]	15
Pulse separation	(for SER and MIR; for EJR) [μs]	350; 550
Number of recordings		500

Table 3.2 Experimental parameters for the precessing jet experiment.

The particles image density is estimated by counting the particles on the images. The measured image density is about 0.052 particles/pixel. Considering the depth of the illuminated volume of 27 mm, this leads to a volumetric particles concentration of about 0.68 particles/mm^3.

The field of view of each camera covers a 1 × 1.07 D^2 area with a digital resolution of 18.8 pixels/mm. The requirement to spatially resolve the coherent structures arising into the cylindrical chamber and at the exit of the fluidic precessing nozzle imposes to investigate the entire probed volume capturing three different velocity fields, i.e., sudden expansion region SER, middle internal region MIR and exit jet region EJR, with an overlap along the streamwise direction approximately of 0.1 D (Figure 3.10). Three different sets of tomographic PIV experiments are carried out for each inflow conditions, i.e., JWG and RG exit nozzle configurations (see Figure 3.9). The total measurement domain is of 1 × 3.05 × 0.27 D^3 (100 × 305 × 27 mm^3). Sequences of 500 couples of images are captured for each experiment at 15 Hz. Considering the typical values of the Strouhal number of the precession motion (Wong et al. 2004), the acquisition frequency complies with the Nyquist-Shannon sampling theorem for the temporal resolution of the precessing jet mode(Nathan et al. 1998), but it does not suffice to resolve in time the coherent structures arising into the shear layer (Yule, 1978). For the SER and MIR experiments, the time separation is of 350 μs. Since the rapid decay of the axial velocity component along the streamwise direction (Wong et al. 2003), the time separation is set at 550 μs for the EJR experiment. The displacement of the particles attains a maximum of approximately 12 voxels along the jet axis. The details of the experimental settings are summarized in Table 3.2.

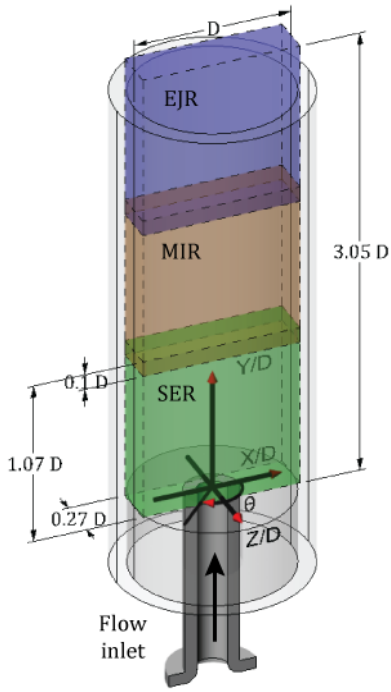

Figure 3.10 Measurement domain and reference frame; sudden expansion region SER (green), middle internal region MIR (orange) and exit jet region EJR (violet).

3.3.2 Calibration procedure

An optical calibration is performed by recording images of a target mechanically translated along the depth *Z* direction of the measurement volume in the range ±16 mm. The calibration markers are black dots on a white background with a regular spacing of 5 mm along two orthogonal directions. A template-matching technique, with a cross-correlation based algorithm, is used to identify the location of the markers. The rms of the initial calibration error is about 1.1 pixels.

The challenge to apply this procedure relies on the impossibility to perform the calibration *in-situ* due to physical restrictions, i.e., the calibration is performed without the presence of the cylindrical chamber. As for swirling jets experiments, the volume self-calibration (Wieneke, 2008) is used to correct the mapping functions to account for misalignment of the lines of sight due to refraction effects along the optical path (as done by Baum et al. 2013 and Ceglia et al. 2013). The corrections are obtained through an ensemble average on 200 images in order to get well-converged statistics. The procedure

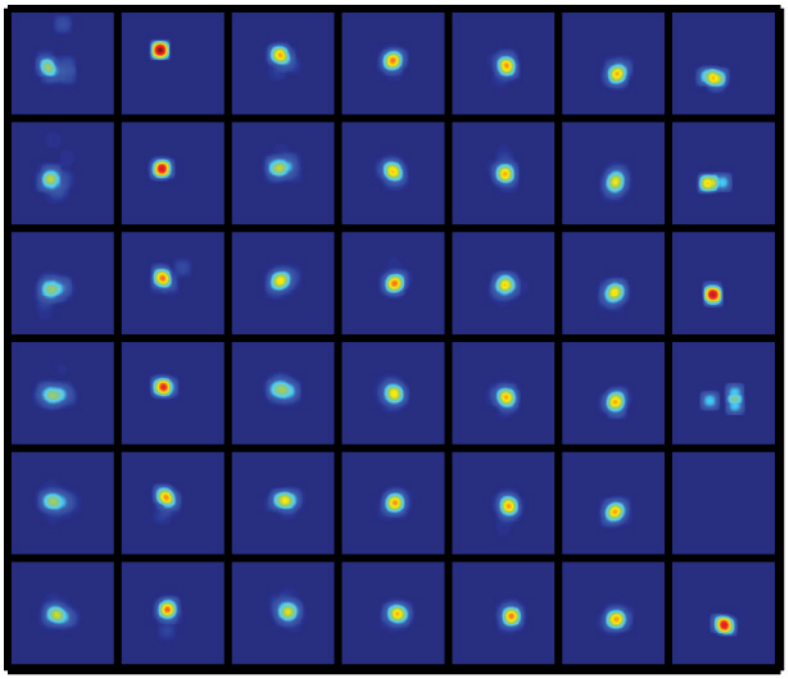

Figure 3.11 Disparity map on the middle plane of the measurement volume.

is an iterative process based on a multi-grid algorithm. In the first iteration, the misalignment due to the relative displacement between the cameras is corrected by computing the disparity map over the entire volume. By considering 600 particles for the triangulation, the maximum correction applied on the camera is of 0.5 pixels. Additional two iterations are performed by computing the disparity maps using 9,000 particles on 2 × 2 × 2 and 5 × 5 × 3 sub-volumes. The final iteration is computed on a refined grid with 7 × 7 × 5 sub-volumes using 11,000 particles; the relative disparity map on the middle plane for one camera is depicted in Figure 3.11. The correlation peak decreases on the left and right side of the volume with some rejections. Indeed, the presence of the residual reflections of the laser on the wall of the cylindrical chamber determines a weaker illumination of the particles compromising the matching on the different images. Interesting enough, the particles are also stretched and distorted because of the optical aberrations due to the change of the index of refraction that the optical path encounters passing through different media. At the end of the self-calibration procedure, the rms of the calibration error is reduced down to 0.03 pixels.

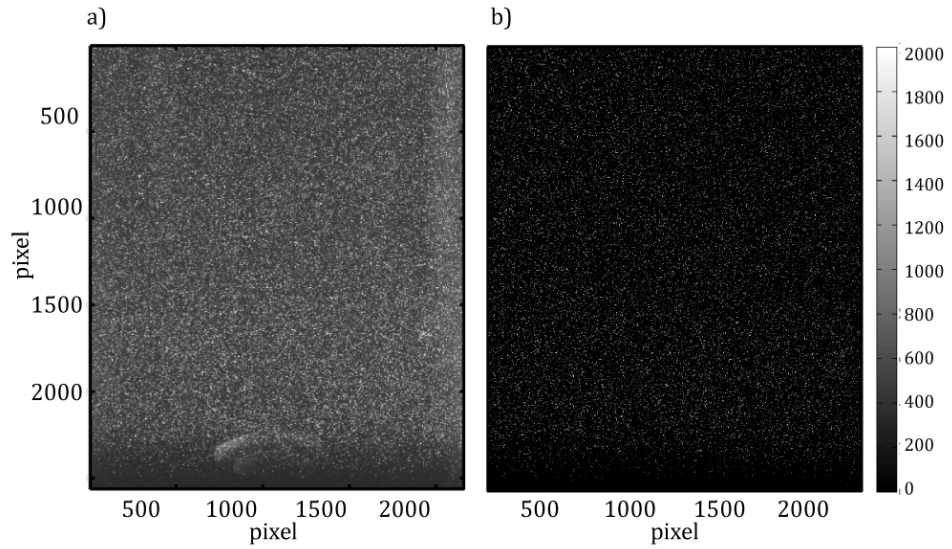

Figure 3.12 Raw (a) and pre-processed (b) particle images.

3.3.3 Tomographic reconstruction

As done for swirling jets images, background intensity on the raw images is eliminated by subtracting the historical minimum based on the acquired sequence of 500 images. Subsequently, a residual fluctuating background is removed applying a sliding minimum subtraction over a kernel of 31 × 31 pixels in space and using 5 samples in time. The raw and pre-processed images are shown in Figure 3.12.

The volumetric light intensity reconstruction is performed using a custom-made multi-resolution algorithm with four CSMART iterations on a binned 2 × configuration and, subsequently, three CSMART and one SMART iterations at the final resolution (Discetti and Astarita 2012). The algorithm CSMART is similar to the SMART technique implemented by Mishra et al. (1999), with the basic difference in the update process, involving each camera separately. In order to enhance the quality of the reconstruction (reduction of the ghost particles matching), one iteration of MTE (Novara and Scarano, 2012) is applied. The illuminated volume is discretized with 2200 × 2300 × 1100 voxels. The quality of the reconstruction is assessed *a-posteriori* by computing the sum of the intensity on *XY* planes. In Figure 3.13a, the intensity of the reconstructed particles with respect to the *Z* direction is shown. A signal to noise ratio is commonly defined as the ratio of the intensity of the reconstructed particles (true and ghost) in the illuminated domain

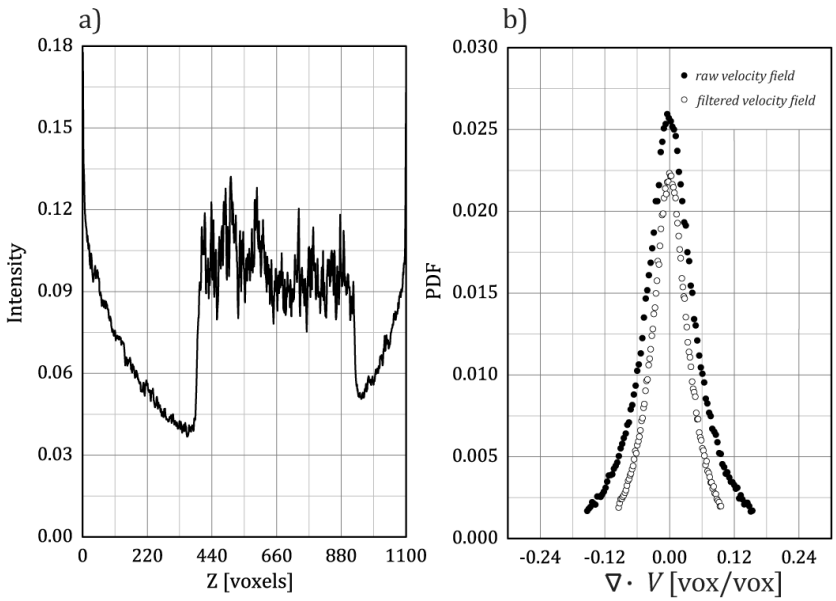

Figure 3.13 Intensity profile in the XZ (depth) plane (a), PDF of the divergence of the raw and filtered velocity field (b).

and the ghost particles intensity in the immediate surrounding domain, it is about 2, that is generally considered a value acceptable for three dimensional velocity measurements.

The 3D particle field motion is computed with volume cross-correlation technique with a final interrogation volume of 64 × 64 × 64 voxels (3.4 × 3.4 × 3.4 mm^3) with an overlap between adjacent interrogation boxes of 75% producing a velocity field measured over a grid of 120 × 115 × 31 points (vector pitch of 0.8 mm).

The uncertainty on the velocity measurement can be assessed by applying physical criteria, for example by computing the divergence of the velocity field. The uncertainty in the divergence is both due to the measurement error on the velocity and the numerical truncation in the derivatives calculation; however, the 75% overlap reduces this second source of error (Scarano and Poelma, 2009), thus making it possible to quantify with reasonable approximation the uncertainty on the velocity measurement using the standard deviation of the divergence. Considering the typical value of the vorticity within the shear layer in the case of circular jet is of 0.2 voxels/voxel, the standard deviation of the velocity field is of 0.011 voxels/voxel (i.e. 6% uncertainty); it is reduced to 0.0076 voxels/voxel (i.e. 4% uncertainty) if a low-pass Gaussian filter on a kernel 3 × 3 × 3 and standard deviation equal to 1 is applied (Figure 3.13b).

3.3.4 Planar PIV measurements

It is known from previous works that the nature of the inlet flow has a significant influence on the probability of precession (Wong et al. 2004). Moreover, according to Nathan et al. (2006), the inlet flow has also a significant influence on the shedding of structures embedded in the shear layer. The profiles of the mean axial velocity $\bar{V}/V_0$ (being V_0 the maximum axial velocity) at the exit of the nozzle is measured with stereo PIV in JWG outflow and without the cylindrical chamber at Re_d=150,000 (Cafiero et al. 2014); the measurement is conducted in order to characterize the inlet conditions along the XZ and XY directions (see Figure 3.10 for the reference frame). A sequence of 1,000 instantaneous realizations is captured with two PCO SensiCam cameras (1280 × 1024 pixels, 6.67 μm pixel pitch), with a time delay equal to 80 μs. A measurement domain of about 3 d × 2.1 d is taken into account. The calibration procedure is similar to that used for the tomographic PIV test (Section 3.3.2), with a plate being imaged at three depths encompassing a measurement domain of ±2 mm. The raw images are dewarped onto a common grid with a resolution of 16 pixels/mm. The image interrogation is performed with the adaptive method implemented by Astarita (2009), with window size of 64 × 64 pixels, overlap of 75%, and Blackman filtering within the interrogation process to tune the spatial resolution (Astarita, 2008). The results, reported in Figure 3.14 versus previous literature data (Mi et al. 2001, Madej et al. 2011), do not show any significant evidence of asymmetry and residual bias.

In order to further characterize the nozzle exit conditions, a planar-PIV measurement is conducted on the unconfined JWG. With the aim of identifying easily the vortex features of the flow, the tested Reynolds number is reduced down to Re_d=16,000. In this case, a larger domain in the streamwise direction is taken into account, in order to characterize the streamwise organization of the large coherent structures of the jet shear layer. As in the previous case, 1,000 realizations have been captured with a time delay of 950 μs. The area is discretized with 12 pixels/mm, corresponding to a measurement domain of about 4 d × 5 d. The method implemented by Discetti and Adrian (2012) is used to significantly reduce the magnification measurement error. The application of the POD analysis (see Section 2.3.2 for implementation details) allows the characterization of the shedding features within the shear layer of the unconfined JWG. Figure 3.15 depicts the most energetic POD mode, where the presence of axisymmetric ring-vortices is outlined from the contour representation of the normalized out-of-plane vorticity $\omega_z\ d\ /\ V_0$.

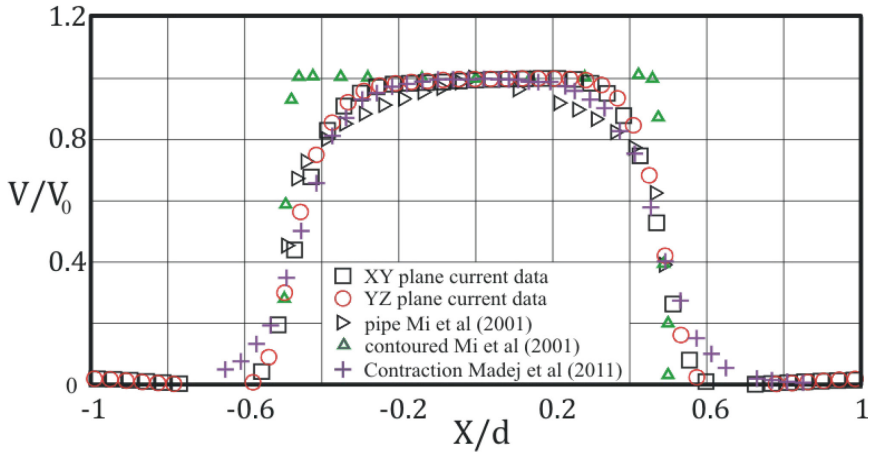

Figure 3.14 Radial profiles of the mean axial velocity $\overline{V}$ normalized versus the jet centerline velocity V_0 for the stereo PIV data set along the XY (□) and YZ (○) planes compared with contoured (△, +), pipe (▷) nozzles extracted from Mi et al. (2001) and Madej et al. (2011).

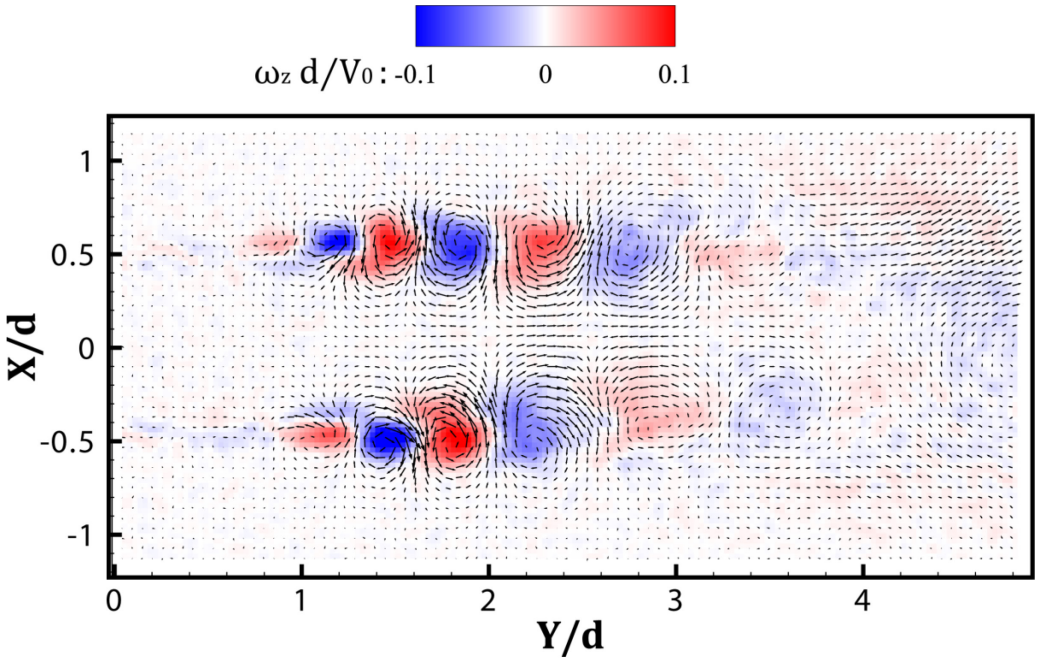

Figure 3.15 Most energetic POD mode of the free jet flow issued by the nozzle at Re_d=16,000. Velocity vectors plotted at each two measured vectors and contour plot of the ω_z d / V_0.

Chapter 4

3D organization of free and confined swirling jets

In the present chapter, the 3D coherent structures organization of the turbulent swirling flow at Re_{D_s}=50,000 generated by an aero engine lean burn injection system in cold (i.e. non-reacting) flow conditions is investigated using Tomographic PIV. The effect of the confinement on both the instantaneous and statistical flow features is addressed. Moreover, a POD analysis is conducted to extract information on the most energetic coherent structures.

4.1 Introduction

The wide application in industrial processes has stimulated many studies to understand the swirling flow organization. The flow field is made complex by both the transition of the flow from jet-like to wake-like, which induces the coexistence of the internal shear layer ISL and outer shear layer OSL, and by the concomitant axial and azimuthal shear stresses; these features impose a challenge to both numerical and experimental investigations. Recent researches are mainly focused on the study of the unsteady vortical features in swirling jets and of their effect on combustion processes (Stöhr et al. 2011, Moeck et al. 2012, Stöhr et al. 2012, Fröhlich et al. 2008); other studies are focused on the development of numerical modelling tools for swirl flows that are still a challenging application (García-Villalba et al. 2006, Roux et al. 2005).

In high swirl flows, the PVC is accompanied by a co-precessing vortex related to the convective waves through the inner and outer shear layer (Syred and Dahman 1978, Cala et al. 2006, Stöhr et al. 2011).

Several experimental investigations are focused on the near field of the swirling jet where different strategies were adopted to reconstruct the 3D flow features from point-wise and planar measurements. Cala et al. (2006) studied the unsteady precessing flow in a swirl burner for a Reynolds number Re=15,000 and Swirl number S=1.01. From the analysis of the phase-averaged data, they identified three precessing helical vortex structures classified as primary and secondary structures forming a 3D vortex dipole. Using POD analysis, phase-averaging technique and azimuthal symmetry of the helical

structures, Oberleithner et al. (2011) produced a 3D representation of the helical vortices from uncorrelated 2D snapshots (obtained by PIV data) in the case of a swirling jet at Re=20,000. The analysis highlighted that the dominant modes are associated with the PVC. Stöhr et al. (2012) performed planar PIV measurements along streamwise and crosswise sectional planes in order to investigate the flow features of the swirling flow with the presence of the flame. Following the approach proposed by van Oudheusden et al. (2005), the 3D topology of the PVC is reconstructed from phase averaged measurements (the phase extraction is carried out using the first two POD modes, containing the bulk of the energy associated with the periodic PVC motion). The reconstruction of the PVC showed clearly that the evolution of the PVC along the axial direction is coupled with a co-precessing vortex in the OSL. On top of this, a LOR of the velocity field is performed using the first two POD modes. The representation of the velocity field provided by the LOR exhibited a pronounced smoothing effect with lesser detailed information than the phase average; however, the LOR is extremely effective in extracting information on the most energetic vortical structures.

Even though the POD analysis based on the 2D planar measurements might enable a three-dimensional reconstruction of the periodic coherent structures, it does not allow an accurate description of the intricate instantaneous 3D structures of the turbulent outflow of swirling jets. Until now, very few studies report about instantaneous 3D measurements in swirling flows (Dulin et al. 2012, Scarano et al. 2015) and further investigations, especially at high Reynolds number, are needed.

4.2 Swirling flow characteristics

In the following, unless otherwise stated, the letters U, V and W will indicate the velocity components along the X, Y and Z directions, respectively. The corresponding lower case letters u', v', w' refer to the components of the turbulent velocity fluctuations obtained by subtracting the mean velocity components from the instantaneous realizations. In the case of a cylindrical reference frame, V_r and V_θ (directed accordingly to Figure 3.5) indicate the components along the radial and azimuthal directions, respectively. The results are presented in non-dimensional form, using the bulk jet velocity V_j and the diameter of the swirling lean pre-vaporized premixed LPP injector D_S as reference quantities. In the following, the statistical analysis has been performed for each velocity field by averaging a set of 500 uncorrelated snapshots.

In Figure 4.1, the average velocity field of the free and confined swirling jets are depicted by the iso-contours of $\overline{W}/V_j$ on the plane Z/D_S=0 (in this plane the vector representation of the $\overline{U}/V_j$ and $\overline{V}/V_j$ components is also reported) and by the iso-surfaces of the axial mean velocity $\overline{V}/V_j = -0.15$.

For both cases, the sudden expansion of the flow at the nozzle exit induces strong velocity gradients that determine the presence of an ISL and an OSL, as reported in (Stöhr et al. 2011, Stöhr et al. 2012). High values of $\overline{W}/V_j$ are detected near the nozzle exit, in agreement with the observations of Stöhr et al. (2011). A cone-shaped reverse flow stream, extending from the nozzle exit along the axial direction, is formed, promoting the formation of an inner recirculation zone IRZ (Lucca-Negro and O'Doherty 2001, Syred 2006, Stöhr et al. 2011).

The confinement dramatically alters the size and shape of IRZ (Syred, 2006) (see Figure 4.1b). The increased size of the IRZ is testified by the wider shape of the iso-surface of the negative axial velocity at the nozzle exit. Furthermore, an outer recirculation zone ORZ is formed between the OSL and the wall of the chamber due to the step-like geometry that the jet encounters when expands at the nozzle exit. In this condition, the flow undergoes the effect of a radial pressure gradient due to the presence of the wall, promoting the Coanda effect (Wille and Fernholz, 1965).

In order to estimate the effects induced by the confinement, the half spreading angle α_S of the swirling jet (Liang and Maxworthy, 2005) is measured as the slope of the linear regression of the radial position of the half-maximum axial velocity (in the outer shear layer) versus Y and it is evaluated in the Y range $0.1 < Y/D_S < 0.3$; the correlation coefficient between the data and the linear fit is equal to 0.99. For the case of the free swirling jet the measured half spreading angle is approximately 18°, while in presence of confinement α is about 36°, i.e. two times larger. Along with this different pattern, a larger swirl number is expected in this latter case. The swirl number S is evaluated on the measured average flow fields in the plane located at $Y/D_S = 0.1$ using the equation proposed in Toh et al. (2010):

$$S = \frac{2\int_0^{D_S/2} R^2 \overline{V}\ \overline{V_\theta} dR}{D_S \int_0^{D_S/2} R\left(\overline{V}^2 - \frac{1}{2}\overline{V_\theta}^2\right) dR} \qquad 4.1$$

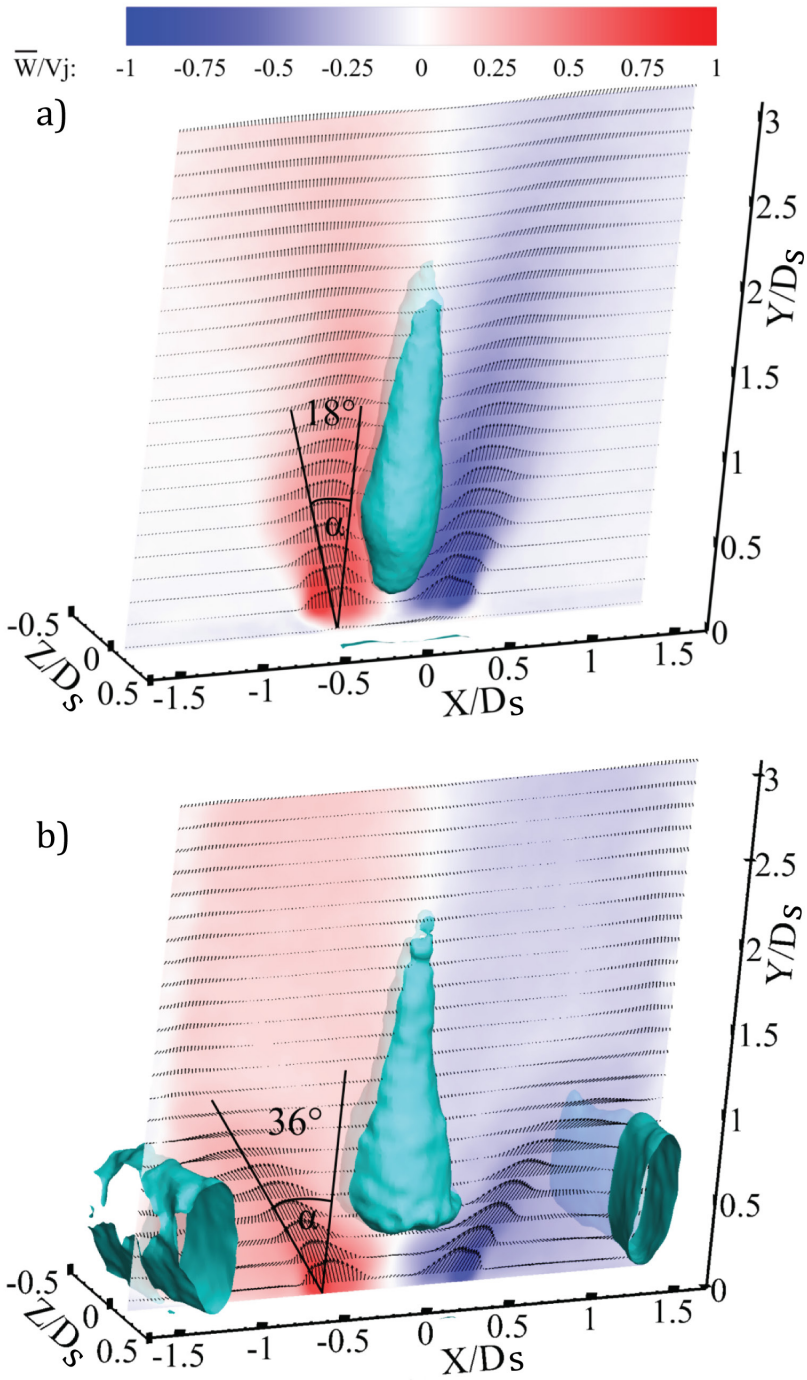

Figure 4.1 Iso-contours with velocity vectors of the mean velocity maps $\bar{W}/V_j$ on the plane Z/D_S=0 and iso-surface of axial mean velocity $\bar{V}/V_j = -0.15$ for the free swirling jet (a) and the confined swirling jet (b).

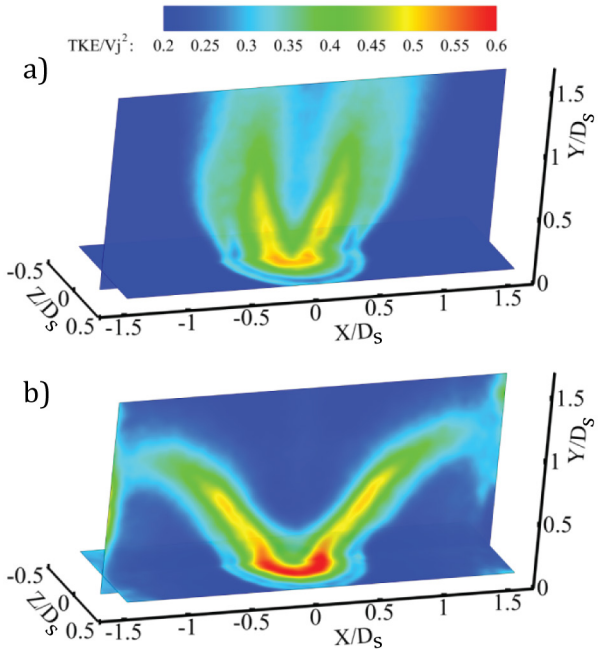

Figure 4.2 Iso-contour of TKE/V_j^2 on planes $Z/D_S = 0$ and $Y/D_S = 0.12$ for the free swirling jet (a) and the confined swirling jet (b).

where R is the radial coordinate. It is worth to note that the swirl numbers for the free and confined swirling jets are equal to 0.90 and 1.27, respectively. Such an increase of the value of the swirl number due to the confinement clearly reflects in the higher spreading angle in agreement with Liang and Maxworthy (2005), but, interestingly enough, it does not cause the expected upstream displacement of the reverse flow region.

In Figure 4.2, the normalized turbulent kinetic energy TKE/V_j^2 is shown for both the free and the confined configuration, respectively. The TKE is defined as:

$$TKE = \frac{\overline{u'u'}+\overline{v'v'}+\overline{w'w'}}{2} \qquad 4.2$$

Local maxima of the TKE are achieved within the shear layers (ISL and OSL), while a relatively low level of turbulence occurs in the neighborhood of the jet axis, i.e. in the IRZ. The confinement determines a higher TKE at the nozzle exit with respect to the case of the free jet, but a lower TKE on the jet axis. In the horizontal slice presented in Figure 4.2 (i.e. the plane $Y/D_S = 0.12$), the ISL and OSL of the jet are well discerned; further downstream the two shear layers tend to merge because of diffusion. The merging occurs at Y/D_S approximately equal to 0.44 and 0.30 for the free and confined swirling jet,

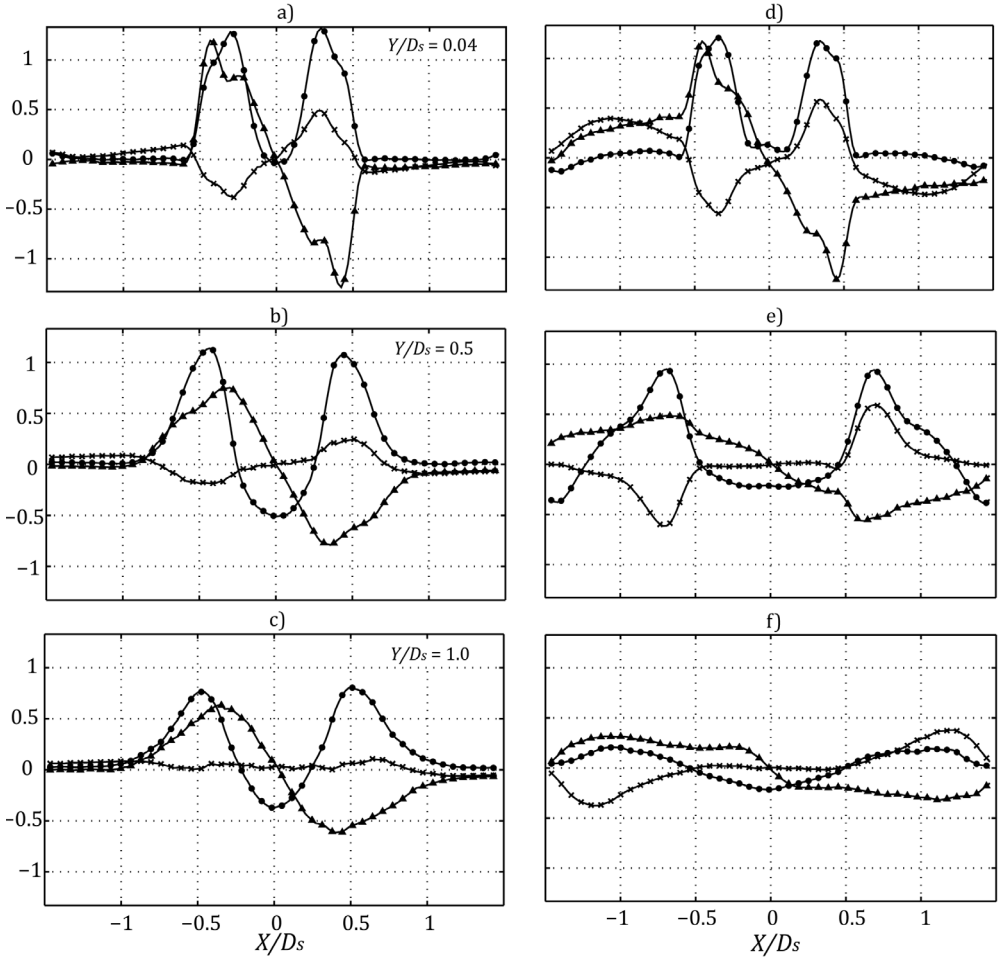

Figure 4.3 Profiles of the average velocity components for free swirling jet (a, b, c) and confined swirling jet (d, e, f) at $Y/D_S = 0.04, 0.5,\ 1.$ × $\overline{U}/V_j$, ● $\overline{V}/V_j$, ▲ $\overline{W}/V_j$. Symbols are placed each 3 measured vectors.

respectively; the abscissa of merging moves upstream in presence of the confinement due to the improved turbulent mixing in proximity of the nozzle exit.

In Figure 4.3, the profiles of the mean velocity components are reported for the free and confined cases at three longitudinal locations (i.e. $Y/D_S = 0.04,\ 0.5$ and 1.0). For both cases, at $Y/D_S = 0.04$ the profile of the axial velocity component $\overline{V}/V_j$ is wake-like, i.e. two local maxima are detected while the velocity is nearly zero in proximity of the jet axis. For the free case (Figure 4.3a), the profile of the $\overline{W}/V_j$ component (which here corresponds to the tangential velocity component) is characterized by the presence of four local peaks, which are due to the combination of the swirling flow issuing from the

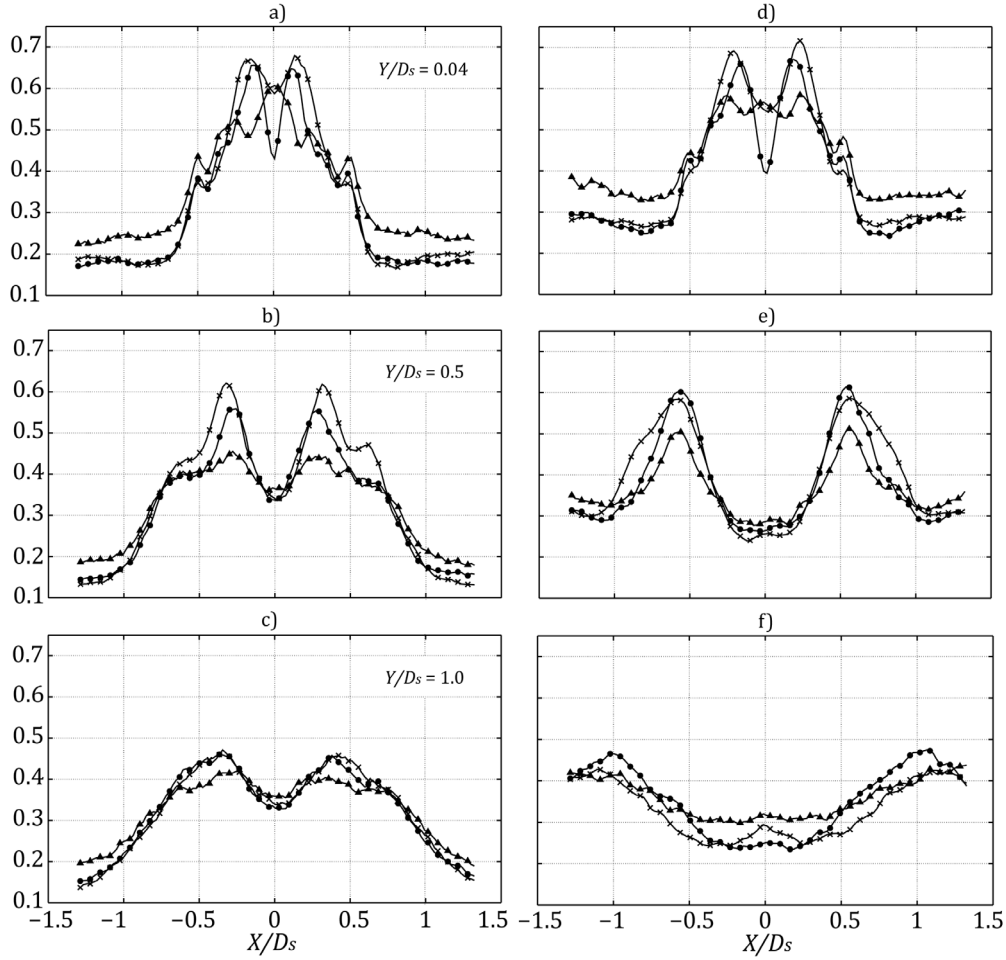

Figure 4.4 Radial profiles of the rms of the normalized turbulent fluctuations for free swirling jet (a, b, c) and confined swirling jet (d, e, f) at $Y/D_S = 0.04,\ 0.5,\ 1.$ $\times\ u'_{rms}/V_j$ ●v'_{rms}/V_j ▲w'_{rms}/V_j. Symbols are placed each 3 measured vectors.

circular and annular nozzles. On the other hand, for the confined case (Figure 4.3d) the internal peaks disappear and the profile exhibits two inflection points. A similar behaviour is detected for the axial mean velocity profile $\overline{V}/V_j$. For the free case, the stagnation point is located on the axis of symmetry of the jet at $Y/D_S = 0.04$ (Figure 4.3a), whereas at the same position the confined swirling flow exhibits a weak positive axial mean velocity value (Figure 4.3d) and the stagnation point is located further downstream from the nozzle exit.

The intensity of the $\overline{U}/V_j$ profiles (that is the radial velocity component for the considered profile) is weaker than that of the other components for both the free and the

confined configurations. Moving downstream, the decay of $\overline{U}/V_j$ is lower for the confined swirling jet, in particular at $Y/D = 1$ the values of the peaks of the $\overline{U}/V_j$ profile are of the same order of the normalized swirling velocity component $\overline{W}/V_j$. In Figure 4.3d-e-f, the effects of the entrainment induced by the ORZ are testified by non-zero values of the velocity components in the region between the OSL and the wall.

The normalized root mean square (rms) of the velocity fluctuations ($u'_{rms}/\mathrm{V_j}$, $v'_{rms}/\mathrm{V_j}$ and $w'_{rms}/\mathrm{V_j}$) are depicted in Figure 4.4. The turbulence intensity is larger in correspondence of the ISL and OSL regions. Even though the $u'_{rms}/\mathrm{V_j}$ and $v'_{rms}/\mathrm{V_j}$ decrease with a local minimum on the jet axis, as reported in Moeck et al. (2012), $w'_{rms}/\mathrm{V_j}$ reaches an additional local maximum value of 0.60 and 0.56 for the free and confined swirling jets at the nozzle exit ($Y/D_S = 0.04$), respectively.

Moving downstream, the effect of the vortex breakdown determines a rapid decay of the intensity of the turbulent fluctuations on the jet axis due to the improved mixing and turbulent dissipation. At $Y/D_S = 1.0$ (Figure 4.4c and f), the maximum values of the normalized velocity fluctuations are achieved much further away from the jet axis for the confined case than for the free case. This behaviour is due to the spreading of the swirling jet that influences the shape of the IRZ.

Even though the $\overline{U}/V_j$ component is weak compared to the other velocity components (Figure 4.3), the relatively high level of $u'_{rms}/\mathrm{V_j}$ indicates a fully 3D flow field in the ISL and OSL (Figure 4.4) with a complex cross-talk between the principal directions of the turbulent fluctuations.

4.3 Instantaneous velocity field

The instantaneous organization of the flow field is illustrated in two snapshots depicted in Figure 4.5. The vector representation of the U/V_j and V/V_j components on the plane $Z/D_S = 0$ shows a zig-zag pattern extending along the axial direction for the free swirling jet, in agreement with Stöhr et al. (2011). On the other hand, for the confined swirling jet a quiescent flow with a weak large recirculation region is detected beyond $Y/D_S = 1.2$.

The Q criterion (Jeong and Hussain, 1995) (Q is the second invariant of the velocity gradient tensor) is used to visualize vortical features. Iso-surfaces of QD_S^2/V_j^2=50 (color-coded with the normalized radial vorticity $\omega_r D_S/V_j$) reveal the presence of a 3D helical

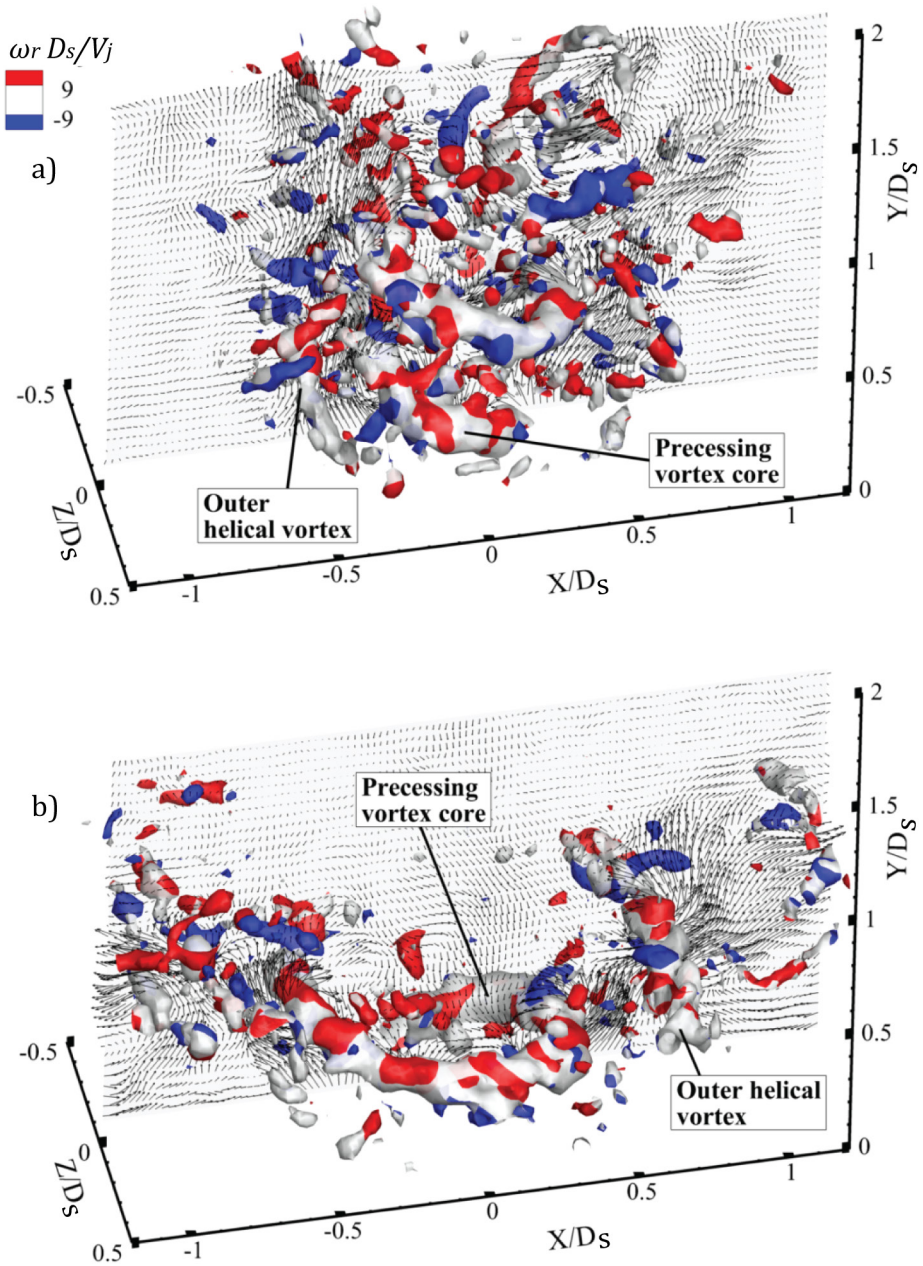

Figure 4.5 Instantaneous velocity field for the free (a) and the confined (b) swirling jet. Vortex visualization using Q (Jeong and Hussain, 1995) criterion color-coded with the normalized radial vorticity $\omega_r D_S/V_j$.

coherent structure, characterized by the PVC (Syred, 2006) and the outer helical vortex. Interestingly enough, the flow field is featured by the presence of smaller turbulent structures with significantly large radial vorticity. The helical vortex exhibits an azimuthal wavy shape in between the local peaks of radial vorticity. It can be hypothesized that these structures determine the azimuthal instability of the helical vortex before its dissipation about $0.8\,D_S$ and $0.5\,D_S$ downstream of the nozzle exit for the free and confined case, respectively. However, the limited spatial resolution of the present measurements does not allow a more conclusive analysis on this regard.

4.4 POD analysis

The unsteady organization of the turbulent swirling flow is analyzed by means of the POD analysis performed on the instantaneous measurements of the 3D velocity field. The distribution of the energy of the POD modes, obtained as the ratio between each eigenvalue and the sum of the entire set of eigenvalues, is illustrated in Figure 4.6. The energy distributions across the first 10 modes highlight that the first two modes constitute the most relevant contribution for both cases, in agreement with literature (Stöhr et al. 2011, Stöhr et al. 2012). For the free case, mode #1 and #2 contribute for the 5.2% and 5.0% of the total TKE. For the confined case, the first pair of modes are less energetic (4.9% and 4.8%, respectively); this slightly larger spreading of the energy over the set of modes may be due to the enhanced mixing effects induced by the simultaneous presence of the IRZ and the ORZ. Interesting enough all the other smaller turbulent features and the measurement noise represent 90% of the TKE.

The first mode is depicted in Figure 4.7 for the free and confined swirling jets, respectively. The iso-surfaces of positive $Q D_S^2/V_j^2$=0.7 color-coded with $\omega_\theta D_S/V_j$ (where ω_θ is the azimuthal component of the vorticity), the contour of $\omega_\theta D_S/V_j$ and the vector representation of the $\overline{U}/V_j$ and $\overline{V}/V_j$ components are blanked by imposing the $-1.2 < \omega_\theta D_S/V_j < 1.2$ constraint. Mode #1 and mode #2 (not shown for conciseness), describe the precessing motion, as it is characterized by two helical vortices located in the ISL, that are phase shifted of π/2 on the crosswise plane and extend up to $0.9\,D_S$ along the jet axis. The $\omega_\theta D_S/V_j$ contour reveals also the presence of the outer helical vortices, placed in the OSL, that are statistically correlated with the PVC helix (Stöhr et al. 2011).

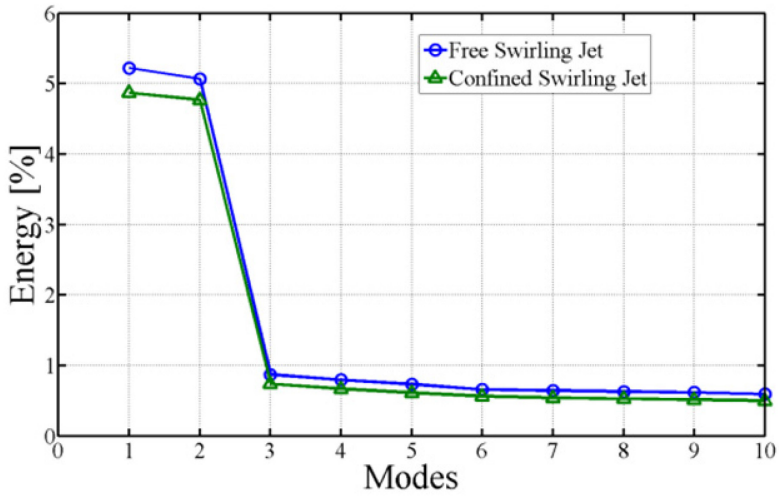

Figure 4.6 Energy distribution of the normalized eigenmodes for the first 10 modes for ○ free and △ confined swirling jet.

4.5 Low order reconstruction

The precessing motion of the PVC can be rebuilt by linearly composing a subset of modes carrying the bulk of the energy (see Ben Chiekh et al. 2004 for a detailed description). This is normally feasible when the flow field is dominated by a periodic/shedding phenomenology, for example the PVC observed for the flow under investigation. In this study the reconstruction of the flow field is achieved through a low-order model incorporating only the mean velocity field and the first two POD modes by applying equation 2.14. Considering the equations 2.15 and 2.16, the phase dependent coefficients $a_1(\varphi)$ and $a_2(\varphi)$ are related to the phase angle φ. Even though the time coefficients are statistically uncorrelated by definition, they are not independent. In order to verify that the first two modes represent the coherent harmonics related to the precession motion, in Figure 4.8, the scatter plots of the time coefficients for the individual realization on the normalized plane $(a_1/\sqrt{2\lambda_1}, a_2/\sqrt{2\lambda_2})$ are shown for the free and confined swirling jets, respectively. The time coefficients are located in the neighborhood of a circle with unit radius, thus confirming the validity of the assumption in equations 2.15 and 2.16. The scattering of the points around the circle is due to the effects of turbulence or small-scale fluctuations, that are not represented in the first two modes.

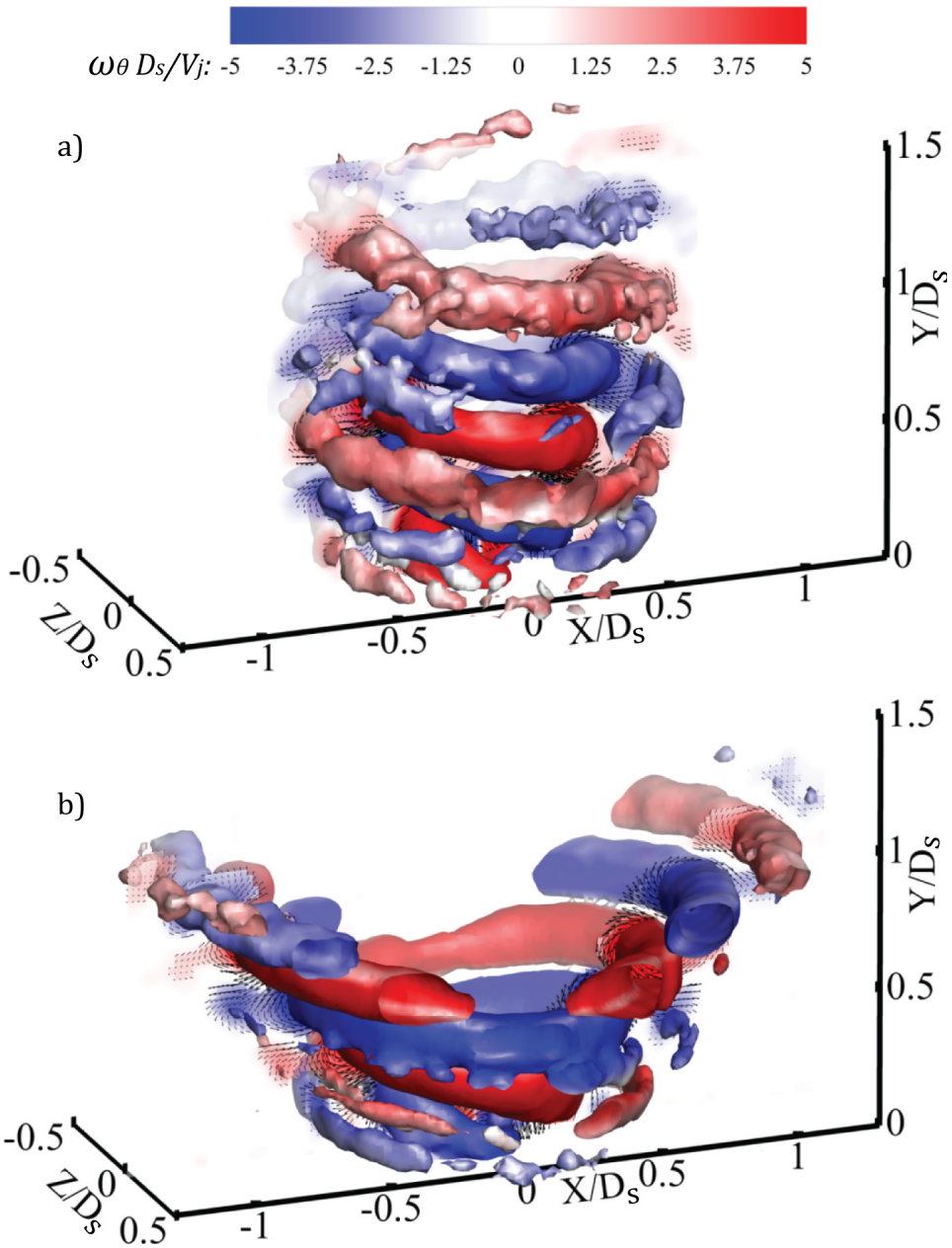

Figure 4.7 First POD mode describing the coherent streamwise development of PVC helix for the free (a) and confined (b) swirling jet. Iso-surface of positive QD_S^2/V_j^2=0.7 color-coded with $\omega_\theta D_S/V_j$. Contour of $\omega_\theta D_S/V_j$ with velocity vectors at plane $Z/D_S = 0$ blanked by imposing the $-1.2 < \omega_\theta D_S/V_j < 1.2$ constraint.

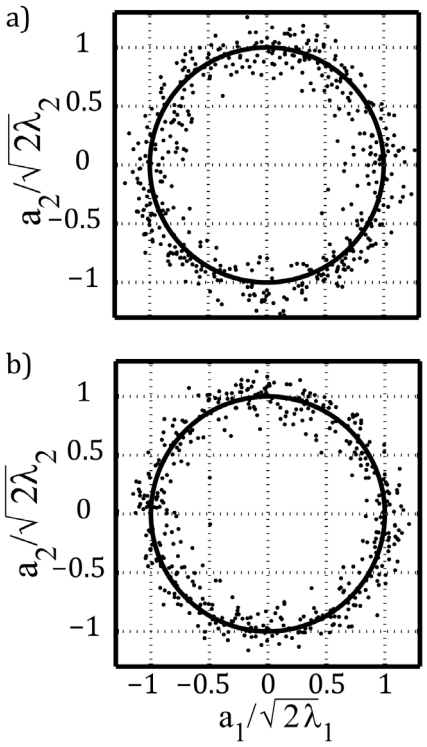

Figure 4.8 Scatter plot of the time coefficients a_1, a_2 for free (a) and confined (b) swirling jets. The circumference with radius 1 is plotted for reference.

The equations 2.15 and 2.16 can be used to extract the phase information, as in Ben Chiekh et al. (2004). An instantaneous realization and the LOR relative to the same phase ($\varphi \approx 0$) are compared in Figure 4.9 for the free (a and c) and for the confined (b and d) swirling jets, respectively. In order to identify the 3D coherent structures, the iso-surfaces of positive normalized QD_S^2/V_j^2 are evaluated at two values equal to 50 and 5 for the instantaneous and LOR velocity field, respectively (in the latter case a lower value is adopted, as the LOR results in smoother velocity fields). The V/V_j contour plot and the in-plane velocity vectors for $Z/D_S = 0$ depict the flow field.

In both free and confined cases, the reconstructed velocity field reveals a more pronounced pattern of the coherent structures: the rebuilt PVC and a counter-rotating and co-precessing outer helical vortex are identified on the external boundary of the OSL, as reported in the literature (Stöhr et al. 2011, Liang and Maxworthy 2005, Dulin et al. 2012). The LOR is not able to capture smaller coherent structures and azimuthal instabilities of the PVC that indeed represent about 90% of the TKE.

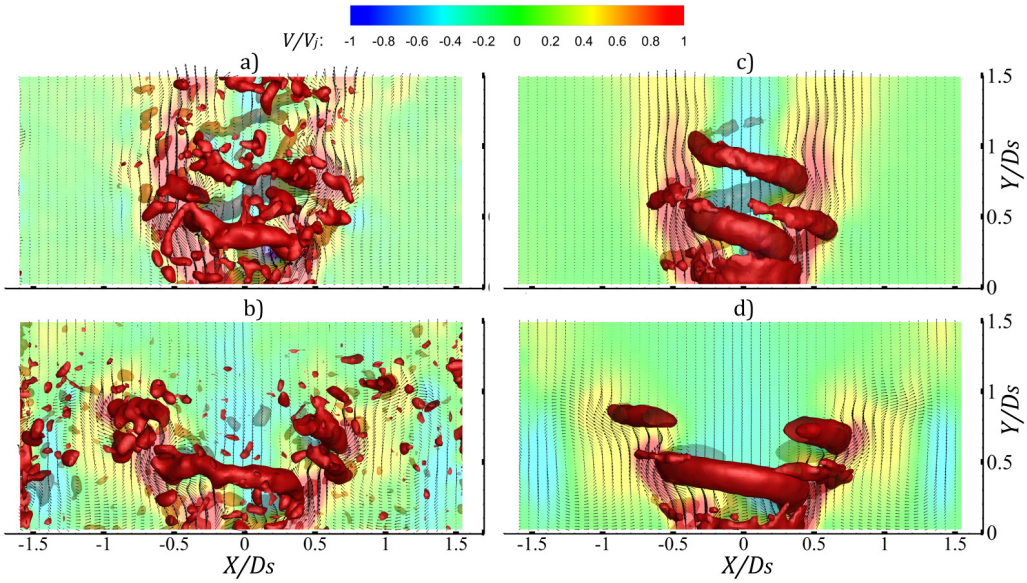

Figure 4.9 Iso-contours with velocity vectors of the instantaneous velocity maps V/V_j (left) and of the LOR velocity (right) at plane $Z/D_S = 0$. Iso-surface of positive QD_S^2/V_j^2 with the normalized azimuthal vorticity $\omega_\theta D_S/V_j$ for free swirling jet (a, c) and confined swirling jet (b, d).

4.6 Final remarks

The 3D organization of the flow structures of a free and a confined swirling jet issuing at $Re_{D_S} = 50{,}000$ from a double swirler aero engine lean burn injection system has been investigated in water by means of tomographic PIV. The vortex topological analysis shows different organization of the large-scale coherent structures between the free and confined configuration.

In both cases, the flow field is dominated by the presence of the vortex breakdown, leading to a cone-shaped stream wrapped around the jet axis, with a wide inner recirculation region.

The confinement dramatically alters the flow field topology, inducing an enhancement of turbulence at the nozzle exit and a more intense mixing. The spreading angle of the confined swirling jet is about two times larger than for the free swirling jet, promoting an increasing of the size of the IRZ in the crosswise direction. This pattern influences the sudden expansion of the swirling flow; in particular the measured swirl numbers for the free and the confined swirling jet are equal to 0.90 and 1.27, respectively. Even though the

effects of the confinement induce a larger spreading of the swirling jet, the expected upstream displacement of the reverse flow stream is not detected.

The instantaneous flow field is characterized by the presence of the PVC and of the outer helical vortex. 3D measurements allow also for the visualization of smaller turbulent structures of radial vorticity which are probably responsible of the development of azimuthal instability of the PVC leading to its further dissipation downstream. However, the limited spatial resolution does not allow for a detailed inspection of the interaction between the small turbulent structures and the PVC.

The application of the snapshot POD analysis to the velocity field is used to investigate the organization of the large scale flow. The first two POD modes are the most energetics and contain 10.2% and 9.7% for the free and the confined swirling jet, respectively. These modes are representative of the 3D helical vortices, i.e. of the PVC, and are located between the ISL and the OSL. Subsequently, a low order representation of the flow field has been calculated based on the first two POD modes. It is found that, using the low order reconstruction, the small-scale structures shown in the instantaneous velocity field are not captured causing a smoothing effect, but the PVC and the outer helical vortex are well represented. The results definitely highlight that 3D-3C measurements are needed for a complete understanding of the turbulent features in swirling flows, even though the path towards the application of Tomo-PIV in large Reynolds number experiments is still steep.

Chapter 5

3D organization of precessing jets

In this chapter, it is investigated a self-excited precessing flow generated by a 5:1 expansion of a round jet in a coaxial cylindrical chamber at Re_d=42,500. A comparative analysis between the JWG and RG inlet configurations has been conducted. The focus is placed upon the statistical analysis and the description of the three-dimensional organization of the large-scale structures generated in the cylindrical chamber.

5.1 Introduction

The development of devices with the aim of enhancing combustion processes by exciting large-scale coherent structures arising in turbulent jets is of fundamental interest for its practical application to burner in cement kilns (Newbold et al. 1997) and for the design of combustion chambers (Smit et al. 1998). The organization of these energy containing structures is influenced by excitation sources based on acoustic (Reynolds et al. 2003), mechanical (Simmons and Lai 1981) and fluidic processes as precessing jets (Nathan et al. 1998).

As already described in Section 1.2, the precessing jet PJ phenomenon is leaded by the intermittent bi-stable behaviour represented by the precessing jet PJ and axial jet AJ modes (Schneider et al. 1997a). This fluidic mechanism produces a highly 3D and unsteady flow field characterized by large-scale coherent structures, produced by the growth of unstable modes arising in the shear layer. These modes result to depend upon the inlet flow conditions, as geometry of the nozzle exit, contraction shape and upstream flow characteristics, and the Reynolds number (Abramovich, 1963).

In free submerged jets, the geometric shape of the nozzle exit has demonstrated a dramatic influence on the organization of the shear layer in the near field and its growing in the far field. Liepmann and Gharib (1992) examined a circular jet deducing that high strain braid regions, occurring between consecutive vortex rings, are influenced by the evolution of counter rotating streamwise vortex pairs leading to the flow transition to turbulence. In the early study conducted by Paterson (1984), multi-lobed profile placed at the exit of a circular nozzle generates mixing processes dominated by large-scale

secondary recirculation regions associated with strong radial velocity. Zaman and Raman (1997) used small tabs placed at the exit of a contoured nozzle to promote the presence of streamwise vortices within the shear layer. El Hassan and Meslem (2010) investigated the role of the Kelvin-Helmholtz (K-H) azimuthal rings and the streamwise vortices of a circular and a daisy-shaped jets using time resolved stereoscopic PIV and POD analysis (see Section 2.3.1 for details). They observed that in the daisy-shaped jet the entrainment process is enhanced by the earlier transition of the streamwise vortex pairs. Mi et al. (2001) investigated the mixing performance of a circular jet issuing from a contoured nozzle, a sharp-edged orifice and a long pipe. Using both qualitative flow visualization and point-wise velocity measurements, they observed that the sharp-edged orifice and the contoured nozzle exhibit evidence of more pronounced presence of coherent structures in the near field. The jet issuing from the contoured nozzle results with large and fairly organized vortices. However, the sharp-edged orifice produces asymmetric and more three-dimensional vortices in the near field. The large-scale structures, shed from the long pipe nozzle, feature less organized patterns with lower energetic vortices around the jet periphery. Mi et al. (2001) pointed out that the upstream separation induced by the geometry of the sharp-edged orifice increases the asymmetric pattern of the vortices.

The idea that the asymmetric organization of the coherent structures in a fluidic PJ contributes to the precessing motion suggests that a reduction of the coherence within the initial shear layer could influence the occurrence of the PJ mode. In the early study of Nathan (1988), the precessing motion was investigated for different inflow conditions. Despite the qualitative results obtained through flow visualization, Nathan (1988) deduced that inlet conditions could influence jet precession. Lee et al. (2001) used a triangular inlet orifice issuing into a cylindrical chamber with an exit lip. They found that for different chamber lengths and expansion ratios the oscillating motion is still present and the external oscillating jet follows a preferred azimuthal direction aligned with the corners of the triangular orifice. Wong et al. (2004) applied to a variety of fluidic PJ nozzles the three inlet conditions previously investigated by Mi et al. (2001). It was found that the precessing motion is promoted more easily by nozzles that shed less organized vortical structures into the initial shear layer. As already introduced, these asymmetric patterns are formed from the sharp-edge orifice and the long pipe. In addition, they pointed out that these turbulent structures are superimposed on the dominant precessing motion, that propagates up to the inlet. Babazadeh et al. (2011) used twelve micro-jets

mounted on the periphery of the inlet of a PJ nozzle to actively control the precessing motion. They determined the position of the jet centre using phase-locked stereo-PIV and pressure measurements, and then compared the results to deduce jet precession characteristics. Nevertheless, the investigation was focused on the effects on the precessing motion without any inspection of the instantaneous flow field. Cafiero et al. (2014) investigated PJ flows by means of Tomo-PIV. They described the internal flow field using POD analysis to infer insight on the main spatial organization of the coherent structures pertaining to the precessing motion.

Studies on PJ flows have been mostly focused on the flow statistics with particular emphasis on parametric investigations regarding different geometrical configurations (Nathan 1988, Wong et al. 2004, Madej et al. 2011) or using external forcing (Babazadeh et al., 2011) to stabilize and control the precessing motion. Nevertheless, as the precession is related to the organization of the coherent structures (Newbold et al. 1997, Wong et al. 2008, Birzer et al. 2011, Cafiero et al. 2014), the observation of their instantaneous pattern is of fundamental importance to understand the basic mechanism of this unstable flow field.

5.2 Precessing jet flow characteristics

In the present investigation, the flow field switches intermittently between the AJ and PJ modes; flow visualizations, conducted for the JWG configuration, have confirmed that the precession occurs in both directions, i.e., it can restart in opposite direction after having switched to the AJ mode (Nathan et al. 1998). It means that the average flow field is not expected to have a net swirling component for the JWG configuration.

The results are presented in non-dimensional form, using the bulk jet velocity V_j and the inner diameter D of the cylindrical chamber as reference quantities. In the following, the statistical analysis has been performed for each velocity field by averaging a set of 500 uncorrelated snapshots.

5.2.1 Mean flow characteristics in SER

In Figure 5.1, the mean velocity field of JWG and RG cases is depicted by iso-surface of axial mean velocity $\bar{V}/V_j$=0.99 and iso-contours with in-plane velocity vectors on cross-sectional planes at different axial distance from the inlet (Y/D=0.02 0.25, 0.50, 0.75 and 0.95).

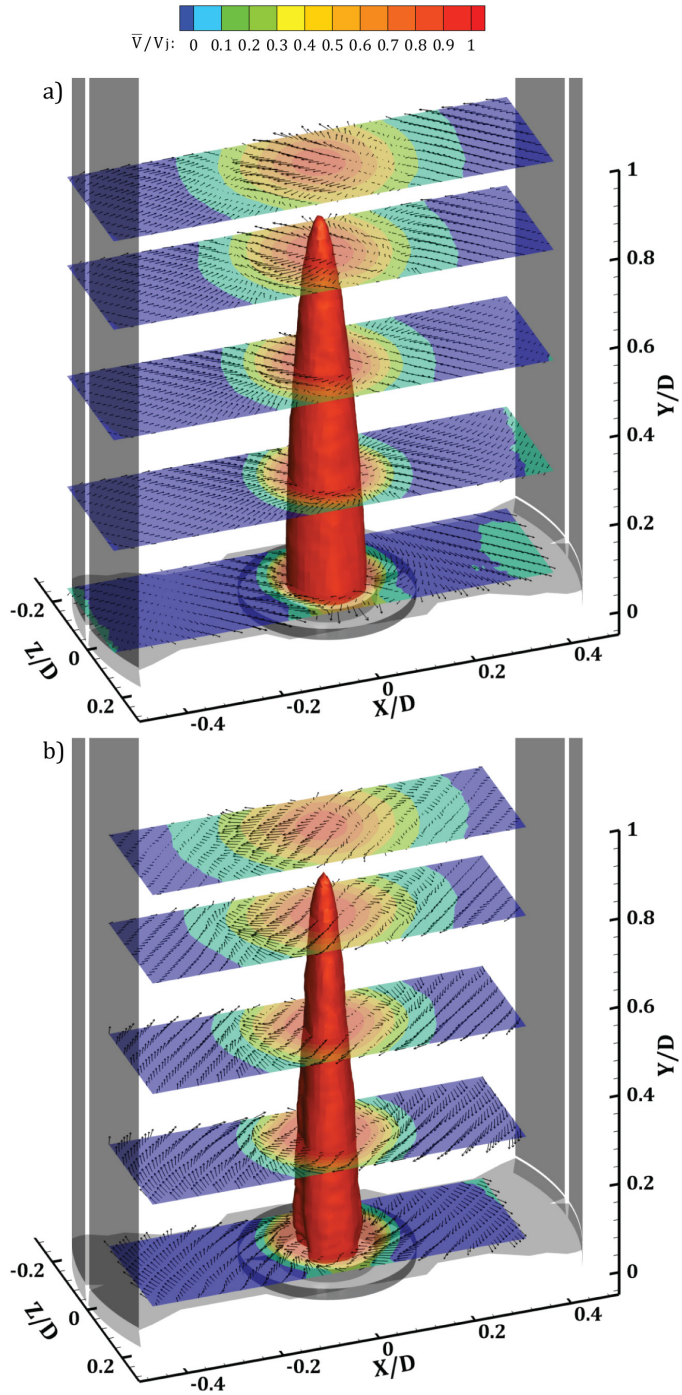

Figure 5.1 Iso-surface of axial mean velocity $\bar{V}/V_j$=0.99 and iso-contours with in-plane velocity vectors placed each five measured points on the planes Y/D=0.02 0.25, 0.50, 0.75 and 0.95 for the JWG (a) and RG (b) in SER.

For both cases, the potential core, which is identified by the iso-surface of $\bar{V}/V_j$=0.99, extends up to Y/D=0.8; further downstream (Y/D=0.95), the axial mean velocity decreases down to 0.9. On the cross-sectional planes, a detailed inspection of the in-plane velocity vectors reveals an inward motion due to the combined effect of the large-scale coherent structures (Liepmann and Gharib, 1992) and the asymmetric entrainment induced during the PJ mode. When the jet passes through the regular grid (RG configuration), the effect of the entrainment is superimposed by the swirl motion induced during the occurrence of PJ mode (Figure 5.1b). Indeed, a swirl motion is detected and it results stronger at the inlet.

In Figure 5.2, iso-contours of normalized turbulent kinetic energy TKE/V_j^2, equation (4.2), on the cross-sectional planes Y/D=0.25, 0.50, 0.75 and 0.95 and iso-contour of $\overline{u'v'}/V_j^2$ on the plane Z/D=0 are presented for the JWR and RG cases.

In both cases, the axial-symmetry of the TKE is well preserved, the overall turbulence is localized within the shear layer. In particular, a local maximum of TKE/V_j^2 about of 0.020 is reached at the plane Y/D=0.25. Further downstream at plane Y/D=0.5, the TKE/V_j^2 reaches a maximum of about 0.031 and 0.027 for JWG and RG, respectively. Further downstream (Y/D=0.95), the peak activity of the TKE/V_j^2 contributes with a maximum intensity of about 0.040. Even though the turbulence level is roughly the same for both cases at the end of the potential core, the iso-contour maps of TKE/V_j^2 indicate that its spread along the crosswise direction is wider for RG than for JWG. For this latter case, the turbulence maps exhibit a roughly uniform pattern along the azimuthal direction.

In terms of transverse Reynolds stress $\overline{u'v'}/V_j^2$, the striking effect of the regular grid in spreading the turbulence intensity is clearly brought out. Indeed, the level of stress results localized in the periphery of the jet core for JWG and more diffused long the crosswise direction for RG.

Centreline distributions of the axial mean velocity $\bar{V}/V_j$ are shown in Figure 5.3a. Both profiles show an inflection point around at Y/D=0.45. In particular for the RG case, the decay of the $\bar{V}/V_j$ reaches the value 0.95 at Y/D=0.79, which is located further downstream than that detected for the JWG case (Y/D=0.72). The turbulent properties also exhibit remarkable differences between the JWG and RG cases. In Figure 5.3b, the rms of the axial and radial turbulent fluctuations, v'_{rms}/V_j and u'_{rms}/V_j, are compared along the centreline for both configurations.

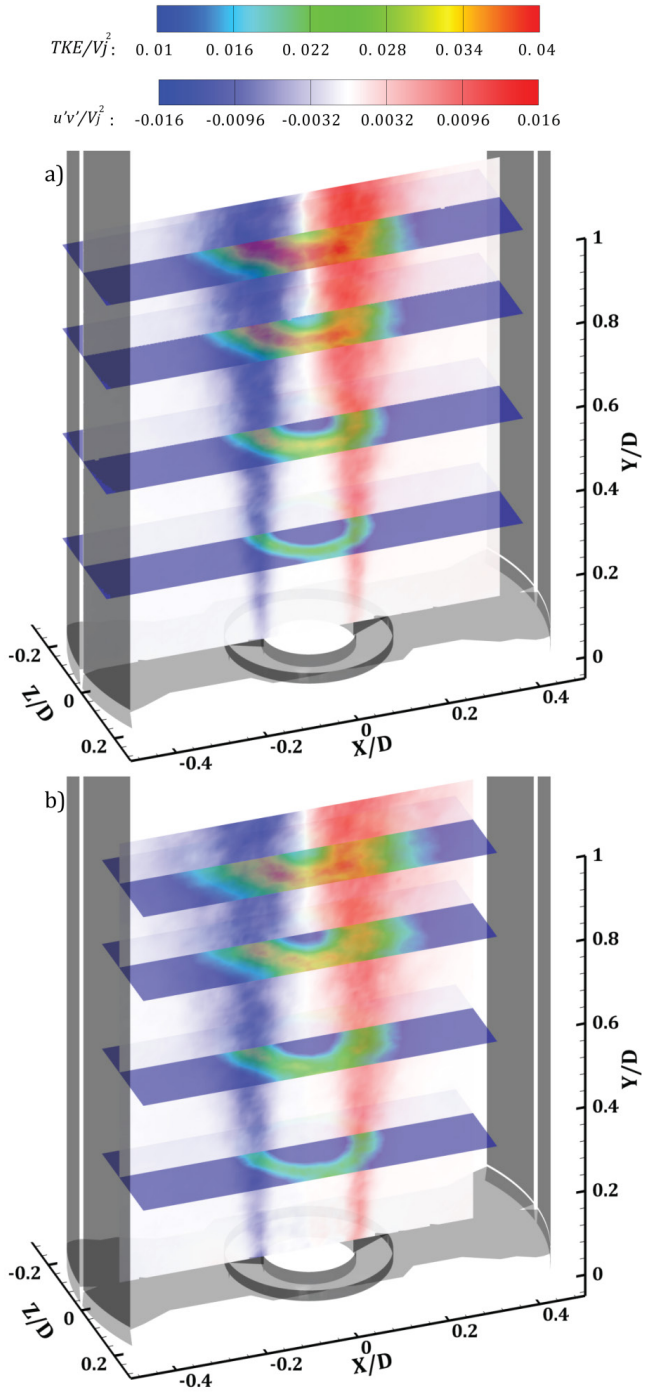

Figure 5.2 Iso-contours of TKE/V_j^2 on the planes Y/D=0.25, 0.50, 0.75 and 0.95 and iso-contour of $\overline{u'v'}/V_j^2$ on the plane Z/D=0 for the JWR (a) and RG (b) in SER.

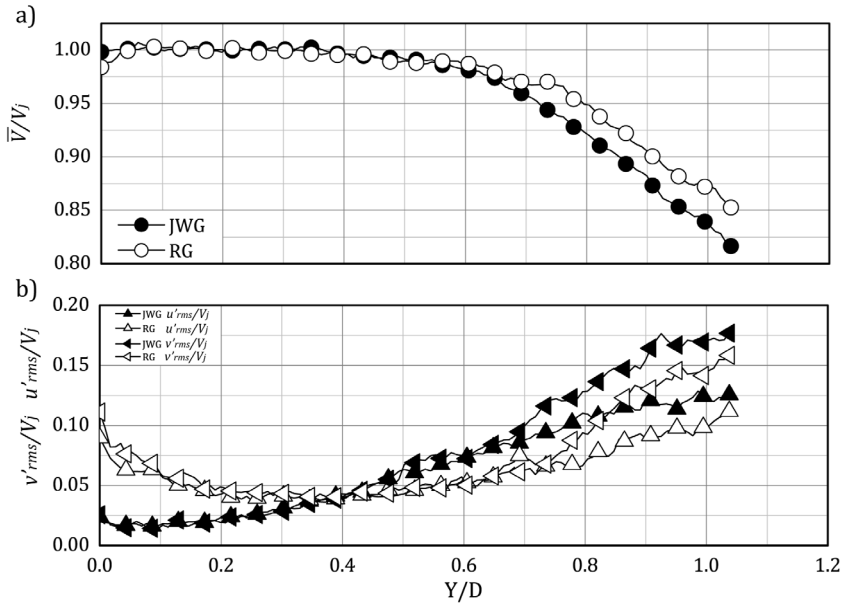

Figure 5.3 Centreline distribution of the axial mean velocity $\bar{V}/V_j$ (a) and of the rms of the axial and radial velocity fluctuations (b), v'_{rms}/V_j and u'_{rms}/V_j, respectively, in SER for JWG and RG configurations. Symbols are placed each five measured points.

For the JWG case, the axial and radial fluctuations increase along the centreline with similar rate up to Y/D=0.65. Moving downstream they reach different maxima v'_{rms}/V_j=0.17 and u'_{rms}/V_j=0.12 at Y/D=1. For RG case, the level of turbulence at the inlet is comparable to that reached at Y/D=1.0, the presence of the regular grid installed at the inlet determines an overall increment of the turbulence in the near-field along the centreline. In particular, axial and radial fluctuations level down to 0.05 between 0.22<Y/D<0.61 and then increase up to 0.15 and 0.096, respectively. However, at Y/D=0.4 the level of turbulence matches for both configurations.

In Figure 5.4, the radial profiles of the mean velocity components are reported for the JWG and RG cases at three cross-sections Y/D=0.25, 0.75 and 0.95. For both cases, at Y/D=0.25 the radial profiles of $\bar{V}/V_j$ are rather top-hat in shape, whereas, moving downstream, their distribution is similar to that observed for a fully-developed pipe flow (Mi et al. 2001). In Figure 5.4a(ii), the profile of $\bar{U}/V_j$ at Y/D=0.25, which corresponds to the radial velocity component, exhibits two external peaks of 0.29 and -0.27 for the JWG case and of 0.23 and -0.20 for the RG case at the radial location X/D=-0.18 and 0.17, respectively.

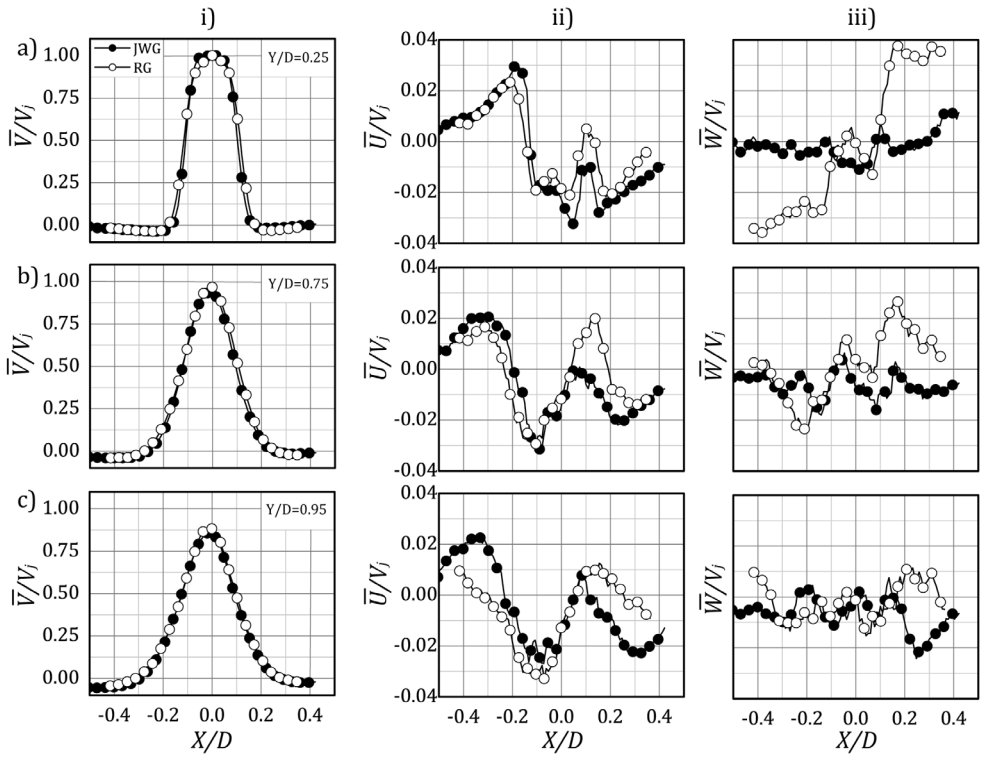

Figure 5.4 Radial profiles of the mean velocity components $\overline{V}/V_j$ (i), $\overline{U}/V_j$ (ii) and $\overline{W}/V_j$ (iii) at cross-sections Y/D=0.25 (a), 0.75 (b) and 0.95 (c) in SER for JWG and RG cases. Symbols are placed each four measured points.

This behaviour is produced by the entrainment effect occurring in proximity of the inlet, it was also observed in free submerged jets (Yule, 1978). At Y/D=0.75, the profiles are characterized by two external inflection points located approximately at X/D=-0.20 and 0.20. As already mentioned, the effect of the swirling motion induced by the PJ mode is testified by the non-zero value of $\overline{W}/V_j$ in proximity of the inlet for the RG configuration (Figure 5.4a(iii)). The residual swirling motion is anti-clockwise with an intensity of 0.036 and almost constant along the radial direction. Moving downstream, the strength of the swirling motion is reduced. At Y/D=0.75, $\overline{W}/V_j$reaches two anti-symmetric peaks of intensity equal to 0.025 (Figure 5.4b(iii)). At Y/D=0.95, the swirling motion becomes weaker, meaning that both configurations have a similar statistical behaviour further downstream.

Radial profiles of the root mean square of the velocity fluctuations v'_{rms}/V_j and u'_{rms}/V_j, and the transverse Reynolds stress $\overline{u'v'}/V_j^2$ for JWG and RG configurations are

reported in Figure 5.5. At Y/D=0.25, the turbulent fluctuations exhibit a peak activity within the shear layer region. The axial velocity fluctuation is approximately 55% higher than the radial one, and it is characterized by two symmetric peaks equal to 0.17. An overall increase of turbulence is detected from Y/D=0.75 (Figure 5.5b-c). In Figure 5.5b(i), v'_{rms}/V_j reaches two symmetric peaks of 0.19 at $|X/D|$=0.11 for both JWG and RG cases. In contrast, local minima of 0.12 and 0.07 are detected on the jet axis for JWG and RG, respectively. The radial fluctuation u'_{rms}/V_j exhibits peaks at the same radial position of v'_{rms}/V_j with maximum intensities of 0.13 and 0.11 for JWG and RG, respectively. Further away from the jet axis, the radial fluctuation for the JWG case gradually decreases with a rate comparable with that observed for the RG case. At Y/D=0.95 (Figure 5.5c), even though the axial fluctuation of JWG shows a lower residual level of turbulence than that produced in the jet with RG at off-axis regions (0.06 at X/D=|0.4|), two local maxima of approximately 0.19 are reached at X/D=-0.11 and 0.09. On the jet axis, the level of the axial fluctuation, as already said, is lower for the RG jet than for the JWG. The radial fluctuation (Figure 5.5c(ii)) roughly flattens to the value approximately of 0.12 and 0.10 on the jet axis for JWG and RG jet, respectively. As outlined by Bradshaw et al. (1964) in their early studies on a free submerged jet, the peak activity detected in axial and radial fluctuations are representative of the pairing process of the vortices within the shear layer.

As observed in free submerged jet flows (Yule, 1978), the transverse Reynolds stress $\overline{u'v'}/V_j^2$ presents an anti-symmetric radial distribution (Figure 5.5(iii)). This indicates that radial velocity fluctuation, predominantly influenced by the entrainment process, correlates with the axial velocity fluctuation, that is related to the axial induction of the large-scale structures in the shear layer (Alkislar et al. 2007). In Figure 5.5(iii), the peak of $\overline{u'v'}/V_j^2$ increases in magnitude to 0.010 for Y/D=0.75 for both configurations. Further downstream, for the JWG case $\overline{u'v'}/V_j^2$ reaches peaks of magnitude equal to 0.012, namely, 46% higher than that detected for the RG case (0.0082).

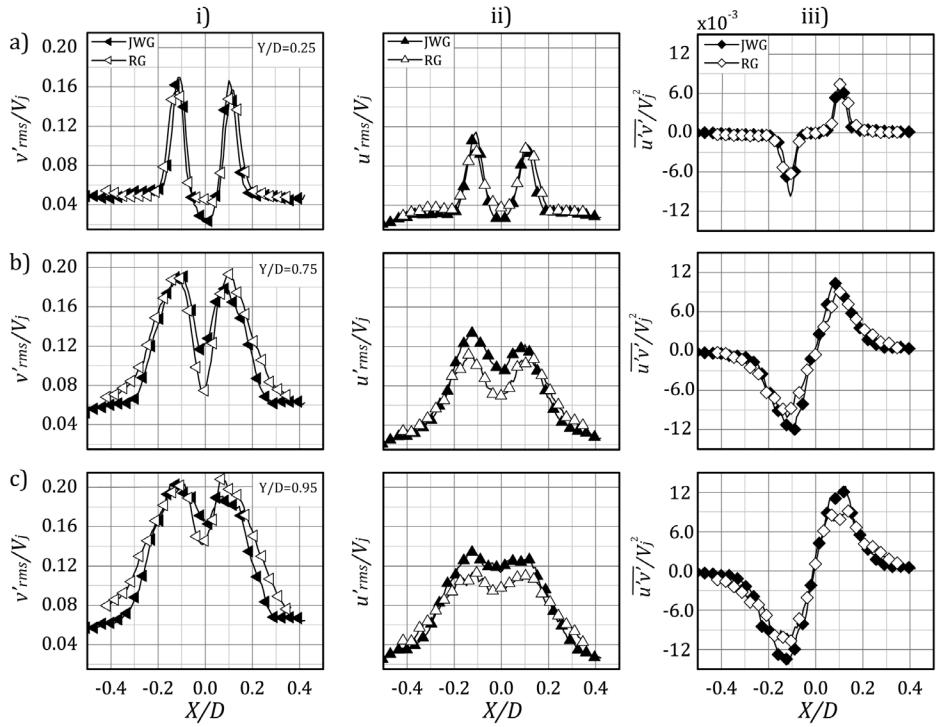

Figure 5.5 Radial profiles of the rms velocity fluctuations, v'_{rms}/V_j (i) and u'_{rms}/V_j (ii), and transverse Reynolds stress $\overline{u'v'}/V_j^2$ (iii) at cross-sections Y/D=0.25 (a), 0.75 (b) and 0.95 (c) in SER for JWG and RG cases. Symbols are placed each four measured points.

5.2.2 Mean flow characteristics in MIR

In Figure 5.6, the mean velocity field of JWG and RG is depicted by iso-surfaces of axial mean velocity $\bar{V}/V_j$=0.7 and -0.02, and by iso-contours with in-plane velocity vectors on cross-sectional planes at different axial distance (Y/D=1.0, 1.25, 1.5 and 1.75).

For both cases, the penetration of the jet, identified by $\bar{V}/V_j$=0.7, reaches the axial location at Y/D=1.43 and a weak reverse flow region is detected by the iso-surface of $\bar{V}/V_j$=-0.02 extending on the entire measurement region along the axial direction. On the cross-sectional planes, the effect of the entrainment is still present, as shown in SER. In particular, it is more pronounced for the JWG case (Figure 5.6a) and it appears stronger in the reverse flow region.

In the region of positive axial mean velocity enclosed by the iso-surface of $\bar{V}/V_j$=-0.02 (Figure 5.6), the entrainment effect characterizes the shear layer region with an inward motion towards the jet axis between 1.0<Y/D<1.5. Further downstream, an inversion in the vectors direction is observed.

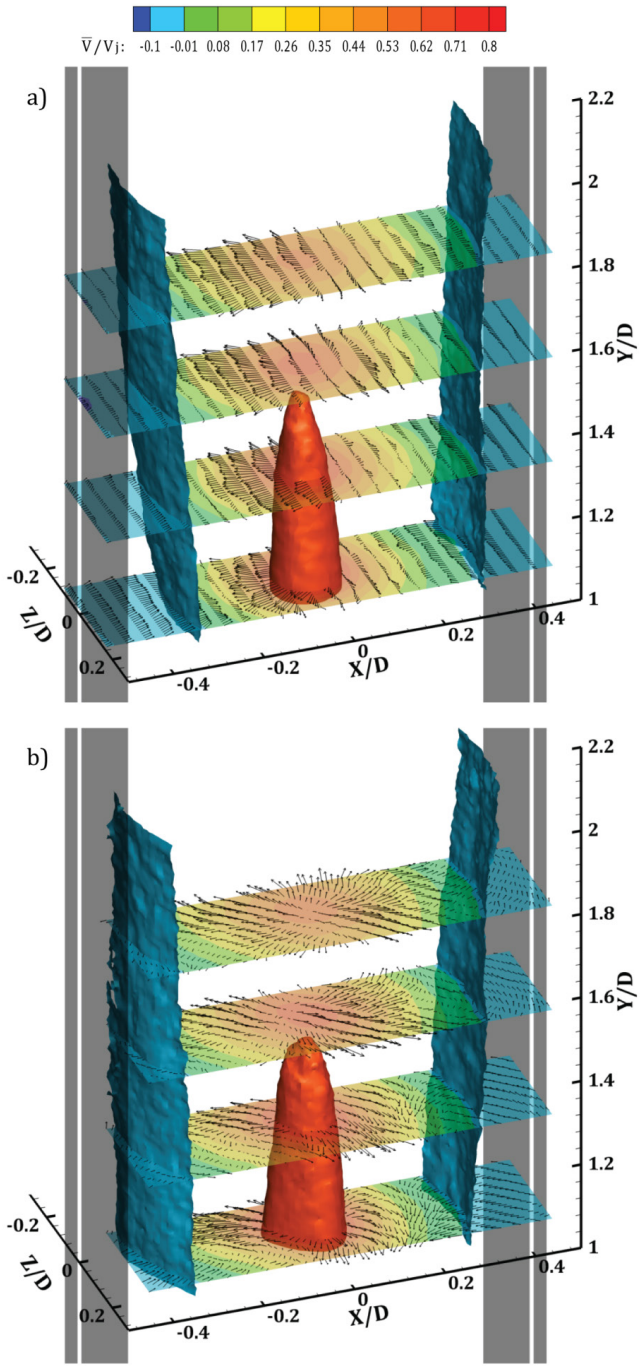

Figure 5.6 Iso-surfaces of axial mean velocity $\bar{V}/V_j$=0.7 and -0.02, iso-contours with in-plane velocity vectors placed each five measured points on the planes Y/D=1.0, 1.25, 1.5 and 1.75 for JWG (a) and RG (b) in MIR.

In Figure 5.7, iso-contours of TKE/V_j^2 on the cross-sectional planes Y/D=1.0, 1.25, 1.50 and 1.75 and iso-contour of $\overline{u'v'}/V_j^2$ on the axial plane Z/D=0 are presented for the JWG and RG configurations. The overall turbulence remains constant along the axial direction for both cases. At Y/D=1.0, despite the level of turbulence attains to a maximum of 0.046 for both configurations, the map of TKE/V_j^2 preserves a more coherent azimuthal distribution for the JWG case than for the RG one. At Y/D=1.25, for JWG case the TKE/V_j^2 decreases in intensity maintaining its azimuthal coherence over the cross-sectional plane; indeed the peak activity is localized into the shear layer region, reaching a maximum of 0.040. For the RG case, the map of the TKE/V_j^2 is characterized by a more diffused pattern over the cross-sectional plane with a maximum of 0.045. Further downstream, the turbulence is diffused along the crosswise direction covering entirely each cross-sectional planes, Y/D=1.50 and 1.75; the overall level of turbulence is higher for the RG case than for the JWG case.

Figure 5.8 shows a comparison plot of $\bar{V}/V_j$, v'_{rms}/V_j and u'_{rms}/V_j along the centreline for JWG and RG configurations. In Figure 5.8a, the axial mean velocity $\bar{V}/V_j$ decreases linearly along the centreline from approximately 0.91 to 0.47 between 1.0<Y/D<2.0 for both configurations. On the other hand, the axial and radial fluctuations remain constant on the values 0.18 and 0.12, respectively.

In Figure 5.9, the axial and radial mean velocity components are reported along X/D at cross-sections Y/D=1.0, 1.50 and 1.75 for JWG and RG cases. The profiles of $\bar{V}/V_j$ exhibit a Gaussian-like shape with the maximum on the jet axis and tails at negative values, for both configurations (Figure 5.9(i)). At Y/D=1.0, the negative $\bar{V}/V_j$ is enclosed between the region identified by $|X/D|$>0.3, reaching a minimum of -0.08. Further downstream, the profile is broader, whereas the region of negative $\bar{V}/V_j$ still preserves the same boundary. In Figure 5.9(ii), the radial mean velocity component shows that the entrainment effect is evident at Y/D=1.0 producing two anti-symmetric peaks of magnitude of 0.018. Moving downstream, an outward motion is detected by anti-symmetric peaks of intensity 0.018 around at $|X/D|$=0.11.

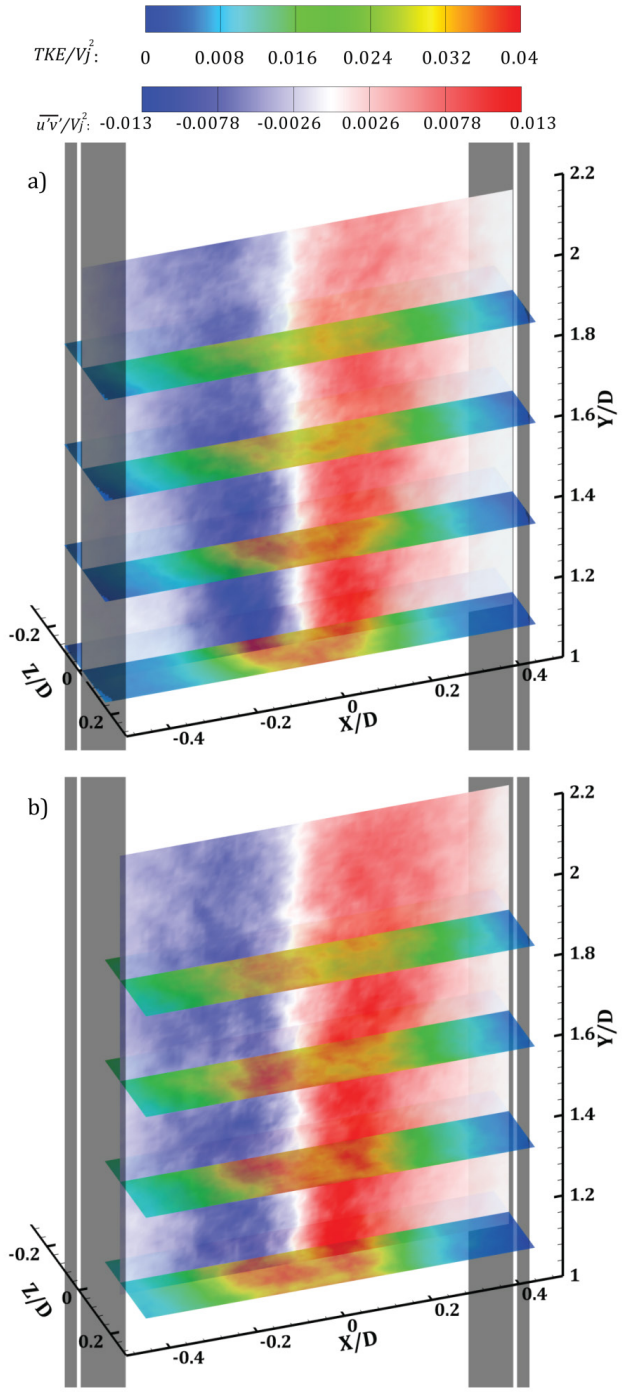

Figure 5.7 Iso-contours of TKE/V_j^2 on the planes Y/D=1.0, 1.25, 1.50 and 1.75 and iso-contour of $\overline{u'v'}/V_j^2$ on the plane Z/D=0 for the JWR (a) and RG (b) in MIR.

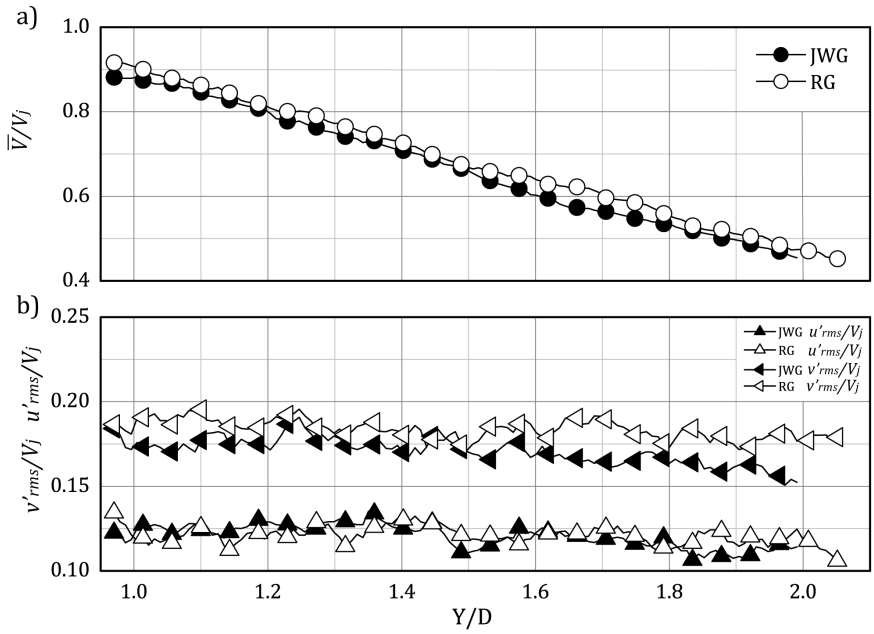

Figure 5.8 Centreline distribution of the axial mean velocity $\bar{V}/V_j$ (a) and of the rms of the axial and radial velocity fluctuations (b), v'_{rms}/V_j and u'_{rms}/V_j, respectively in MIR for JWG and RG configurations. Symbols are placed each five measured points.

Figure 5.10 shows the radial profiles of v'_{rms}/V_j and u'_{rms}/V_j at different cross-sections Y/D=1.0, 1.50 and 1.75 for the JWG and RG configurations. At Y/D=1.0, for the JWG case the axial fluctuation is axisymmetric with two peaks of 0.19 at around $|X/D|$=0.08. In proximity of the outer chamber v'_{rms}/V_j decreases down to 0.07. For the RG case, the axial-symmetry of the v'_{rms}/V_j is not verified, a peak of intensity 0.22 is detected at X/D=0.09; away from the jet axis, the axial fluctuation drops to 0.11 and 0.07 at X/D=-0.40 and 0.46, respectively. For both configurations, the radial fluctuations exhibit axial-symmetric profiles; at $|X/D|$<0.12, u'_{rms}/V_j flattens to about 0.13 and then decreases down to 0.03 moving away from the jet axis. Further downstream (Figure 5.10b-c), both configurations exhibit axial-symmetric radial profiles for axial and radial velocity fluctuations. In Figure 5.10b(i), a minimum of v'_{rms}/V_j=0.17 at the jet axis is observed together with two maxima of 0.19 at $|X/D|$=0.1 for the RG case. The presence of the regular grid at the inlet determines a slightly increment of the overall axial fluctuation respect to that observed for the JWG case. On the other hand, both configurations show that their radial fluctuations collapse at Y/D=1.5 and 1.75.

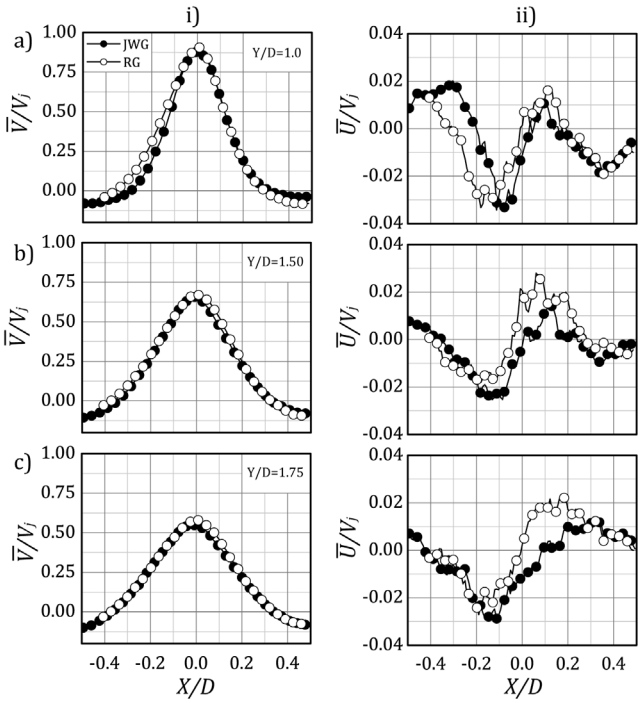

Figure 5.9 Radial profiles of the mean velocity components $\overline{V}/V_j$ (i) and $\overline{U}/V_j$ (ii) at cross-sections Y/D=1.0 (a), 1.50 (b) and 1.75 (c) in MIR for JWG and RG cases. Symbols are placed each four measured points.

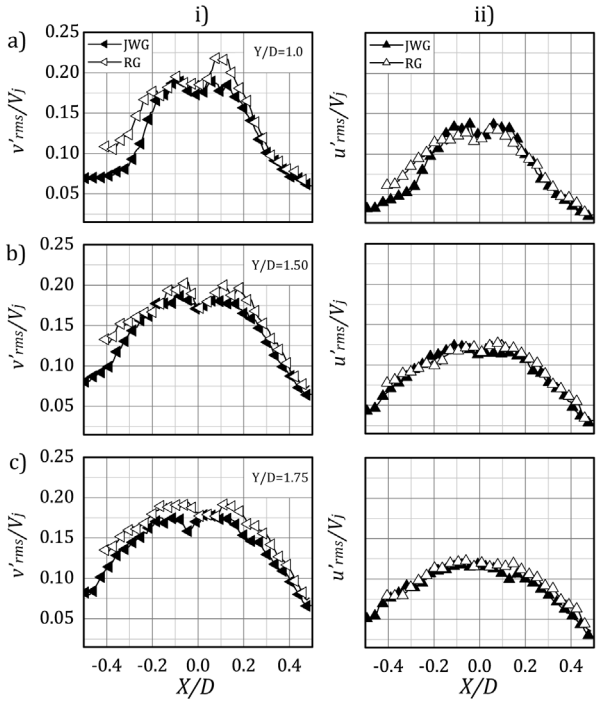

Figure 5.10 Radial profiles of the rms velocity fluctuations, v'_{rms}/V_j (i) and u'_{rms}/V_j (ii) at cross-sections Y/D=1.0 (a), 1.50 (b) and 1.75 (c) in MIR for JWG and RG cases. Symbols are placed each four measured points.

5.2.3 Mean flow characteristics in EJR

In Figure 5.11, the mean velocity field for JWG and RG cases is depicted by iso-surface of transversal mean velocity $\overline{U}/V_j$=0 color-coded with axial mean velocity $\overline{V}/V_j$. Iso-contour of $\overline{U}/V_j$ is shown at the axial plane Z/D=0; iso-contours with in-plane velocity vectors on cross-sectional planes at different axial distances Y/D=2.3, 2.5, 2.8 and 3.0 are also presented. For both configurations, the mean flow field is characterized by a transverse outward motion, as testified by the direction of the in-plane vectors on the cross-sectional planes. On the plane Z/D=0, an anti-symmetric pattern of $\overline{U}/V_j$ is shown in the axial range 2.0<Y/D<2.75. At the exit of the cylindrical chamber (Y/D>2.75), a quasi-uniform pattern of transversal mean velocity is observed on the axial plane Z/D=0 and on the cross-sectional plane Y/D=3.0 for the JWG case. On the other hand, for the RG case the iso-surface of $\overline{U}/V_j$=0 identifies an anti-symmetric composite pattern of the transversal mean velocity component. An inward motion due to entrainment effects is observed at the external regions delimited by the iso-surface of $\overline{U}/V_j$=0 from Y/D>2.75; this effect is stronger near the edges of the cylindrical chamber.

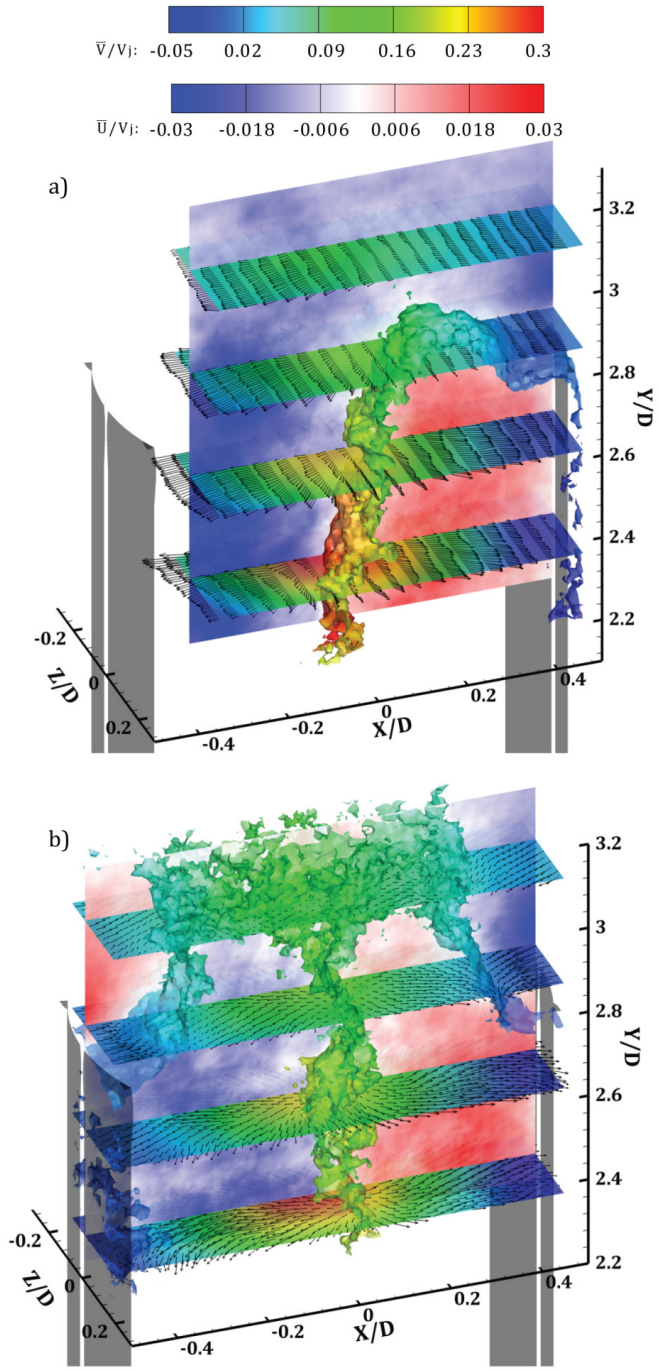

Figure 5.11 Iso-surface of transversal mean velocity $\bar{U}/V_j$=0 color-coded with axial mean velocity $\bar{V}/V_j$, iso-contour of $\bar{U}/V_j$ on the axial plane Z/D=0 and iso-contours on cross sectional planes Y/D=2.3, 2.5, 2.8 and 3.0 with in-plane velocity vectors placed each five measured points for the JWG (a) and RG (b) in EJR.

The turbulent characteristics are presented, for JWG and RG cases, in Figure 5.12 in terms of normalized turbulent kinetic energy TKE/V_j^2, depicted on the cross-sectional planes Y/D=2.3, 2.5, 2.8 and 3.0 and normalized transverse Reynolds stress $\overline{u'v'}/V_j^2$ on the axial plane Z/D=0. The overall turbulence decreases along the axial direction for both configurations. At Y/D=2.3, the distribution of the turbulent kinetic energy over the cross-sectional plane indicates the presence of a complex 3D pattern occurring in the entire observed region; peaks of maximum intensity of 0.025 for JWG and 0.031 for RG are detected. Further downstream (Y/D=2.5), the distribution of the TKE/V_j^2 preserves its spreading with a weaker overall turbulence intensity; peaks are observed with maximum values of 0.022 and 0.024 for the JWG and RG configurations, respectively. On the cross-sectional planes in proximity of the exit of the fluidic PJ nozzle (Y/D=2.8 and 3.0), the degree of spreading is reduced indicating that the overall turbulence is localized in the regions near the jet axis. For JWG case, the intensity of the TKE/V_j^2 reaches a maximum of 0.015 at the cross-sectional plane Y/D=2.8, and then reduces to 0.11 at Y/D=3.0. This indicates that an axial turbulence suppression down to 36% occurs along the streamwise direction. For the RG case, TKE/V_j^2 attains a maximum of 0.020 at Y/D=2.8 with a turbulence suppression down to 54% moving downstream at Y/D=3.0.

In Figure 5.13, axial mean velocity, axial and radial velocity fluctuations are compared along the centreline. For the JWG case, the axial mean velocity decreases linearly from 0.36 to 0.18, between 1.95<Y/D<2.53. Further downstream, it reduces its decay rate and drops to 0.12 at Y/D=3.0. For RG case, $\bar{V}/V_j$ decreases with a decay rate quite constant from a value of 0.30 between 1.95<Y/D<2.7 and then it levels out to 0.12. In Figure 5.13b, the axial fluctuation is 0.17 at Y/D=1.95 for JWG case, that is, 18% lower than that detected for the RG case at the same axial position. At Y/D=2.52, v'_{rms}/V_j decreases to 0.13 for both configurations, and then flattens down to 0.1 at Y/D=2.85. As already observed in MIR, the radial fluctuation remains constant with intensity of about 0.1 between 1.95<Y/D<2.60, further downstream slightly decreases to 0.07 at Y/D=2.85 and 3.0 for RG and JWG configurations, respectively.

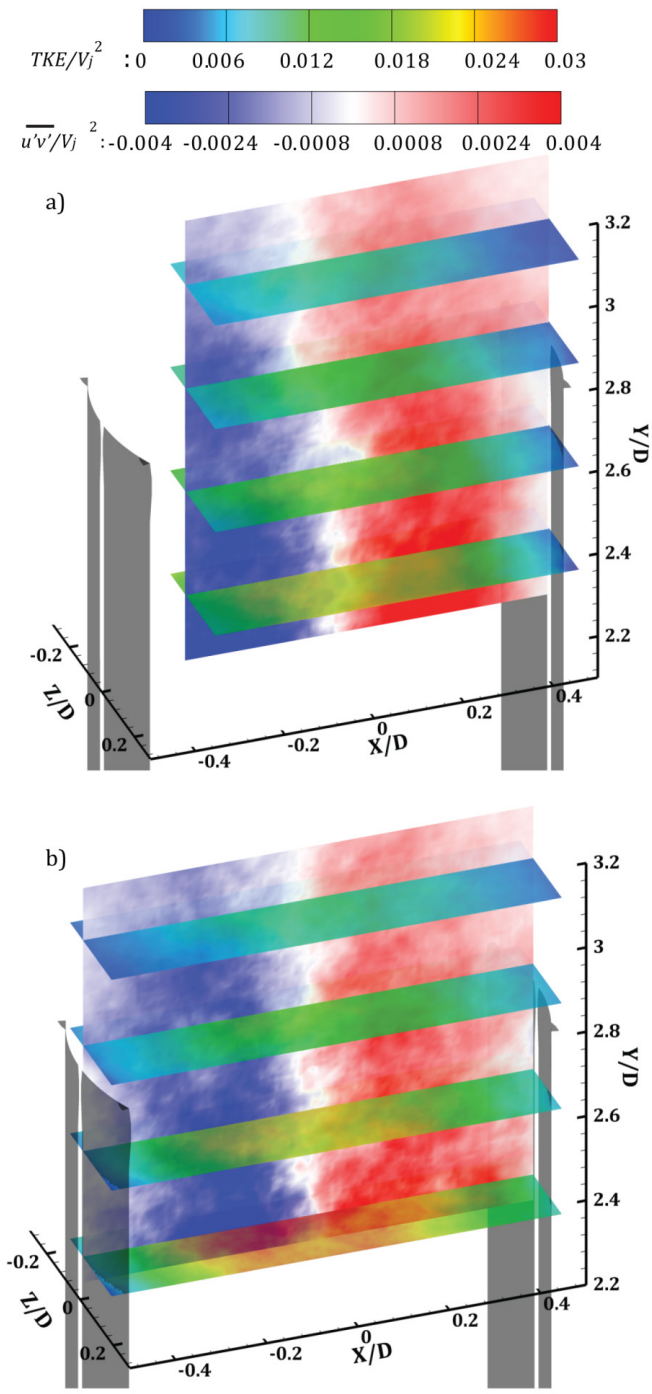

Figure 5.12 Iso-contours of TKE/V_j^2 on the planes Y/D=2.3, 2.5, 2.8 and 3.0 and iso-contour of $\overline{u'v'}/V_j^2$ on the plane Z/D=0 for the JWR (a) and RG (b) in EJR.

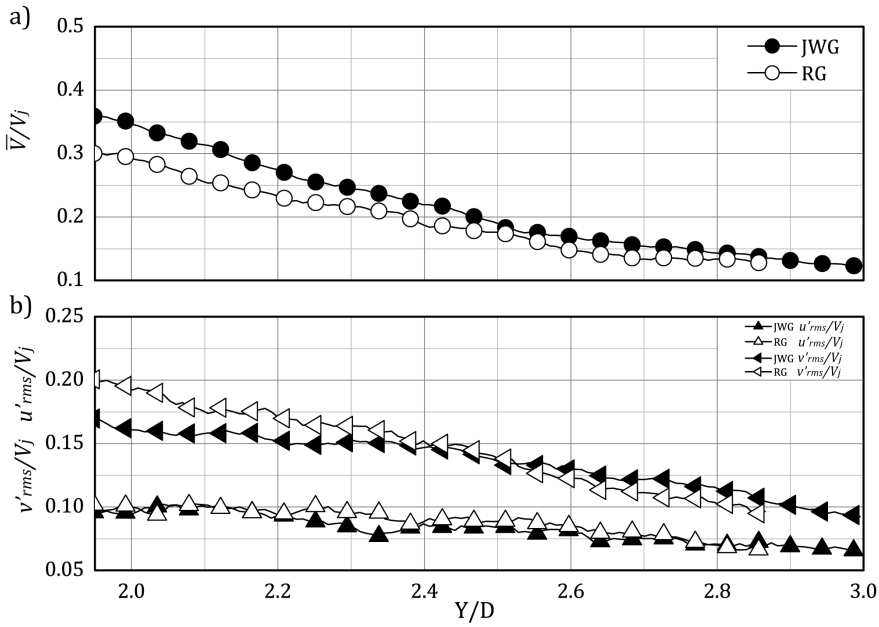

Figure 5.13 Centreline distribution of the axial mean velocity $\bar{V}/V_j$ (a) and of the rms of the axial and radial velocity fluctuations (b), v'_{rms}/V_j and u'_{rms}/V_j, respectively in EJR for JWG and RG configurations. Symbols are placed each five measured points.

Figure 5.14 shows radial profiles of the axial and radial mean velocity components at the axial positions Y/D=2.20, 2.55 and 2.80 for JWG and RG cases. At Y/D=2.20, $\bar{V}/V_j$ exhibits a maximum of 0.27 at the jet axis for the JWG case, whereas a peak of intensity of 0.23 is reached at X/D=-0.050 for the RG configuration. Away from the jet axis, the axial mean velocity drops to negative values of about -0.021 for both cases. An anti-symmetric distribution of the radial mean velocity is detected with two peaks of intensity 0.023 at $|X/D|$=0.28 for RG case. For JWG case, $\bar{U}/V_j$ decreases down to a minimum equal to -0.031 at X/D=-0.21 and reaches a maximum 0.020 at X/D=0.24. Thus, an outward motion across the jet is observed. At Y/D=2.55, the radial profile of $\bar{V}/V_j$ becomes broader with a maximum of intensity 0.17 at the jet axis for both configurations. For the RG case, the radial mean velocity shows an anti-symmetric profile with an inflection point at X/D=0. In the region enclosed by $|X/D|$<0.30, two peaks of intensity 0.01 at $|X/D|$=0.15 are shown, indicating a localized outward motion. In the regions $|X/D|$>0.30, the entrainment process of the fluid coming from the external ambient induces an inward motion with a maximum

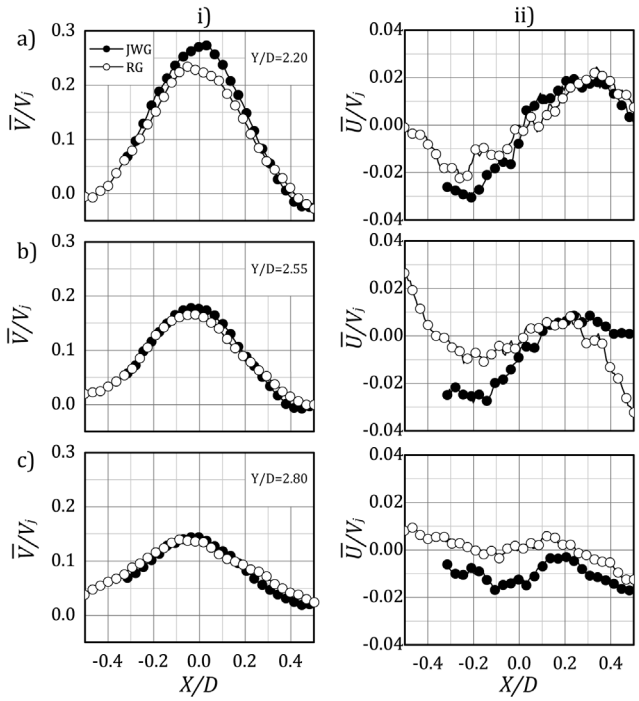

Figure 5.14 Radial profiles of the mean velocity components $\overline{V}/V_j$ (i) and $\overline{U}/V_j$ (ii) at cross-sections Y/D=2.20 (a), 2.55 (b) and 2.80 (c) in EJR for JWG and RG cases. Symbols are placed each four measured points.

intensity of 0.031 that rapidly decreases at the boundary of the investigated region. For the JWG case, the peak of $\overline{U}/V_j$ exhibits a quasi-anti-symmetric radial profile with a minimum of -0.025 at X/D=-0.21 and a maximum of 0.009 at X/D=0.26. At Y/D=2.80, the radial broadening of $\overline{V}/V_j$ is more pronounced with a maximum of 0.14 on the jet axis for both configurations. In Figure 5.14c(ii), for the RG case the radial mean velocity component shows a profile with three inflection points. For the JWG case, a residual negative radial velocity component is observed, $\overline{U}/V_j$ attains to a zero-value at X/D=0.21.

In Figure 5.15, radial profiles of the axial and radial velocity fluctuations are reported at Y/D=2.20, 2.55 and 2.80 for JWG and RG cases. At Y/D=2.20, the axial velocity fluctuation features a maximum of 0.18 at X/D=-0.084 and 0.15 on the jet axis, for RG and JWG cases, respectively. As already introduced, a residual intensity of v'_{rms}/V_j=0.10 and 0.051 is observed in the external region for the RG and JWG cases, respectively. However, the radial fluctuation (Figure 5.15a(ii)) rapidly levels out to 0.095 moving towards the jet axis, for both configurations. As a consequence, the main contribution to the overall

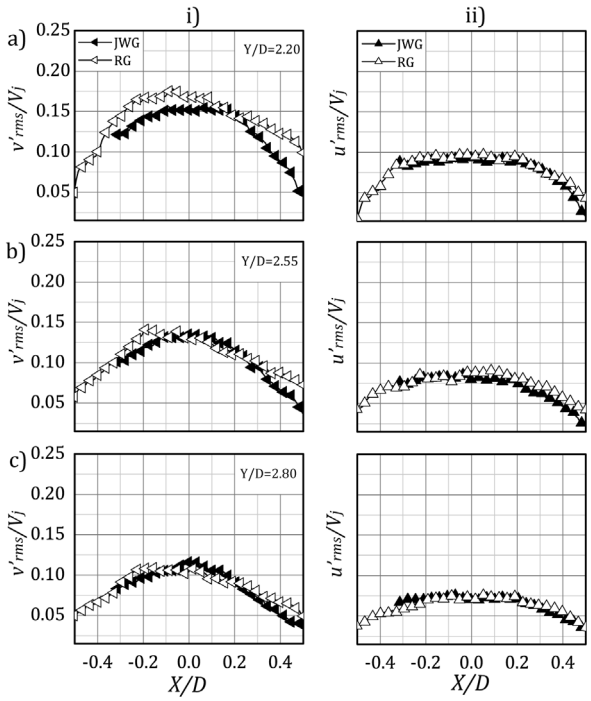

Figure 5.15 Radial profiles of the rms velocity fluctuations, v'_{rms}/V_j (i) and u'_{rms}/V_j (ii) at cross-sections Y/D=2.20 (a), 2.55 (b) and 2.80 (c) in EJR for JWG and RG cases. Symbols are placed each four measured points.

turbulence along the crosswise direction is produced by v'_{rms}/V_j. At Y/D=2.55 (Figure 5.15b), the axial fluctuation reaches a maximum of 0.13 at the jet axis and then flattens down to 0.070 at X/D=0.5 for the RG case, that is, 63% higher than that detected for the JWG case (0.043). Moving downstream, this difference is reduced, the radial profiles of both configurations are superimposed for the axial and radial velocity fluctuations (Figure 5.15c). At Y/D=2.80, v'_{rms}/V_j peaks with a maximum of 0.11 on the jet axis and decreases down to 0.05 in off-axis regions. At this radial location, the residual intensity of u'_{rms}/V_j=0.05 is of the same order of magnitude of v'_{rms}/V_j, meaning that the entrainment process is characterized by a 3D complex turbulent flow field at the exit of the cylindrical chamber.

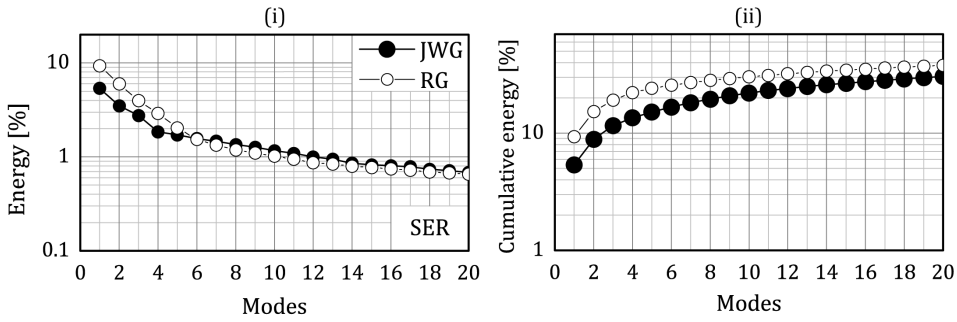

Figure 5.16 Energy distribution across the first 20 modes: normalized eigenmodes (i) and cumulative energy (ii) in SER.

5.3 POD analysis

Proper orthogonal decomposition (POD, see Section 2.3.1) has demonstrated a powerful data reduction method to extract information about coherent structures in turbulent flows (Berkooz et al. 1993). In order to elucidate the basic 3D patterns that participate to build up the large scale coherent structures in a PJ flow, the POD analysis is conducted on the velocity field of SER for the JWG and RG configurations. The decomposition is based on 500 uncorrelated snapshots, which produces, in principle, a number of modes equal to the number of realizations (Sirovich, 1987).

In Figure 5.16, the distribution of the energy across the POD modes is illustrated for the first 20 modes. The eigenvalues are normalized with respect to their sum, which corresponds to the total turbulent energy of the fluctuations. In addition, the cumulative sum of the energy is reported in order to highlight the contribution of each mode to build up the decomposition of the velocity field.

Modes #1 and #2 capture 9.4% and 6.1% of the total kinetic energy, respectively, for the RG case; whereas less kinetic energy corresponds to modes #1 and #2 for the JWG case (5.4% and 3.5%, respectively). The difference in the energy pertaining to modes #1 and #2 can be due to the shape of the measurement volume. Indeed, the entire inflow and outflow regions, captured by mode #1 (see Figure 5.17), are enclosed in the measurement volume, while for mode #2 those regions are in part located outside the observed volume.

The first two modes are depicted in Figure 5.17, in which iso-surface of positive (light grey) and negative (dark grey) v'/V_j are reported. For conciseness, only the modes relative to the JWG case are shown. Modes #1 and #2 describe the precessing motion of the PJ mode and are phase-shifted of $\pi/2$ with respect to the crosswise direction.

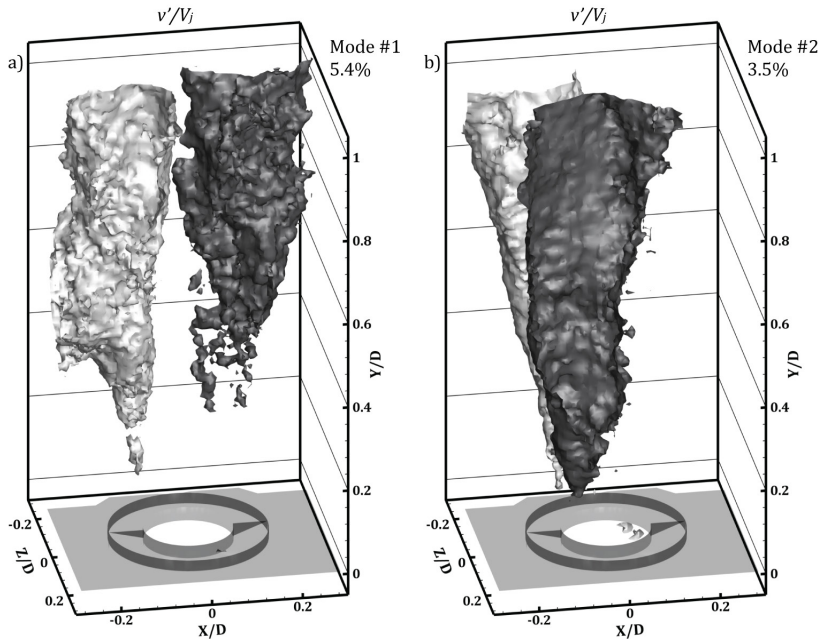

Figure 5.17 POD modes #1 and #2 describing the precessing motion of the PJ mode. Positive (light grey) and negative (dark grey) iso-surface of v'/V_j.

On the other hand, by inspecting the modes from #3 to #10, which correspond to 12.5% of the total kinetic energy, it is possible to infer insights on the large scale features developing in the near field of the jet. Modes #3 and #4, #5 and #6, #7 and #8, #9 and #10, are in pairs and are characterized by the same phase shift found for the first two modes. Iso-surfaces of v'/V_j, v'_r/V_j and v'_θ/V_j are presented, in the following figures, only for one mode of each pair. In Figure 5.18, modes #3 and #4 describe the precessing motion of the AJ mode. The axial and radial fluctuations show four filaments, two positive and two negative, extending along the streamwise direction. In Figure 5.19a-c, modes #5 and #6 describe an helical motion of the AJ mode occurring at the end of the potential core $0.6<Y/D<1.0$, as testified by the intertwining between positive and negative axial fluctuation; a wave-like motion is also observed by the wavy pattern of v'_r/V_j and v'_θ/V_j. This behaviour was previously reported by Iqbal and Thomas (2007), who pointed out similar observations for an axisymmetric free jet issuing at high Reynolds number. More recently, Violato (2013) described these braid regions for a subsonic free jet at Re_d=5,000. Modes #9 and #10 exhibit similar intertwining regions of the axial fluctuation indicating again a helical motion of the AJ mode. This is coupled with a wave-like motion and a periodic twisting as described by v'_r/V_j and v'_θ/V_j, respectively (Figure 5.19d-f).

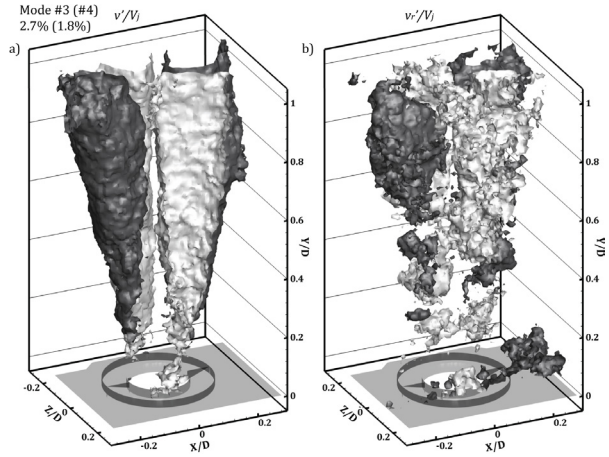

Figure 5.18 POD mode #3 describing the precessing motion of the AJ mode. Positive (light grey) and negative (dark grey) iso-surfaces of v'/V_j (a) and v_r'/V_j (b).

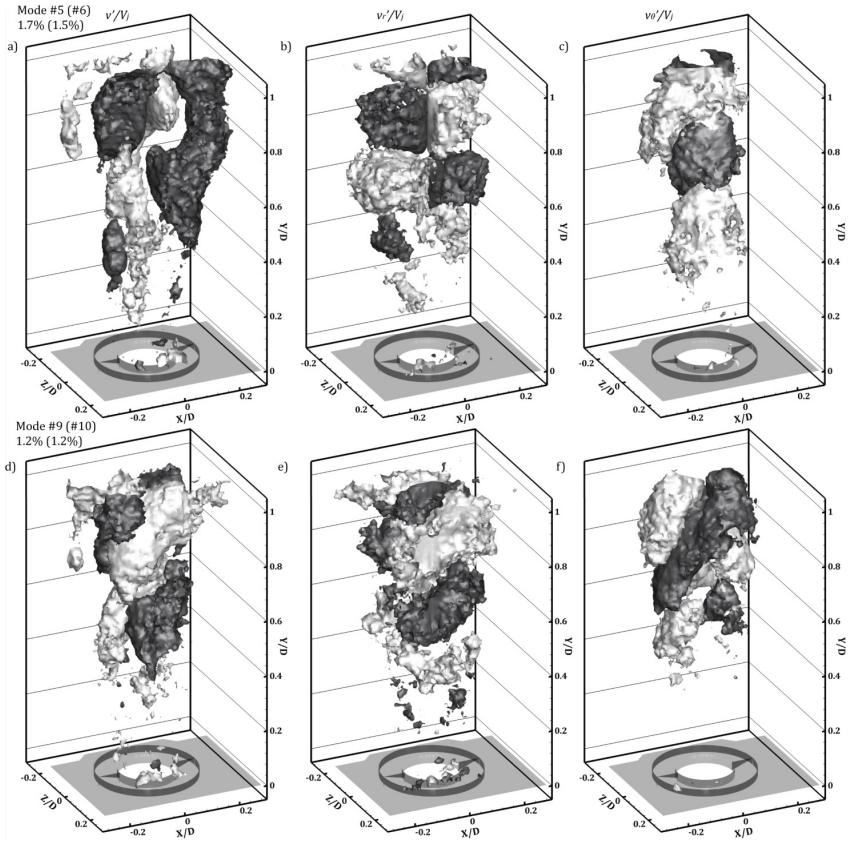

Figure 5.19 POD modes describing the helical motion of the AJ mode. Positive (light grey) and negative (dark grey) iso-surfaces of v'/V_j, and v_r'/V_j and v_θ'/V_j.

5.4 Instantaneous velocity field

Since the driving force of the precessing motion is the inertial effect induced by the asymmetric entrainment triggered by the turbulent fluctuations (Cafiero et al. 2014), the instantaneous flow field is expected to be predominantly influenced by the entrainment flow passing through the exit of the cylindrical chamber. During the precession, the entrainment region is extended along the chamber and interacts with an asymmetric recirculation region located at the inlet inducing a swirl motion on the basis of the chamber (Nathan et al. 1998). The asymmetry of these two regions promotes the occurrence of the PJ mode. Furthermore, as outlined by Nathan et al. (1998) the direction of the swirling motion is opposite to that of the precession to balance the angular momentum. As already mentioned, the present measurements enable to resolve in time the jet precession, thus it is possible to inspect its evolution by detecting the asymmetric entrainment. Since the parallelepiped shape of the measurement volume is oriented with its main length aligned with the diameter of the chamber (see Figure 3.10), the entrainment flow can be recognized by a 'bubble' of negative velocity located asymmetrically with respect to the jet column.

In this section, an investigation on the intricate instantaneous velocity field is conducted in SER, MIR and EJR for the JWG case in order to highlight the influence of the entrainment, together with the swirl motion, on the organization of the large-scale coherent structures that participate to the jet precession.

5.4.1 Flow topology in SER

The instantaneous flow organization is depicted in Figure 5.20 for JWG case when the incipient entrainment process occurs in SER. The iso-surface of V/V_j=1.05 (red) describes the jet column development along the axial direction. The contours of V/V_j in-the Z/D=0 plane clearly shows the presence of an asymmetric negative velocity region (V/V_j <-0.18) representing the travelling entrainment 'bubble' which is extended around 0.39<Y/D<0.44 on the left side of the chamber. The iso-surface of $\lambda_2 D/V_j$=-30 color-coded with the normalized axial velocity component V/V_j reveals an intricate pattern of vortices localized in the shear layer. Even though these structures are axisymmetric for the JWG in free-issuing condition (as already shown in Section 3.3.4), the most prominent feature of a PJ flow relies on their more complex organization caused by the growth of the Kelvin-Helmholtz instabilities and the presence of an azimuthal swirl component. Their combination produces helical vortices that wrap around the jet core.

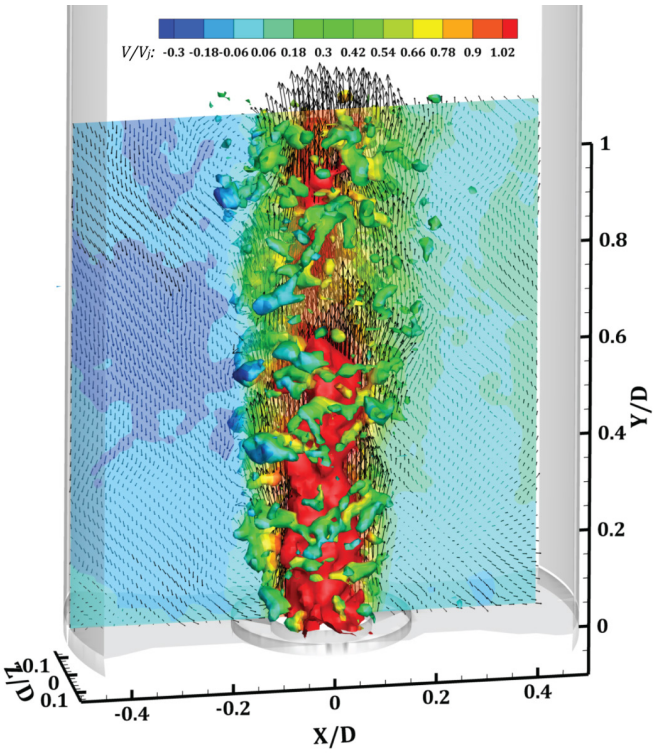

Figure 5.20 Instantaneous velocity field in SER for JWG case. Vortex visualization using λ_2 criterion color-coded with the normalized axial velocity component V/V_j. Iso-surface of V/V_j=1.05 (red) and iso-contour of V/V_j with in-plane velocity vectors placed each three measured points on the plane Z/D=0.

In Figure 5.21, a detailed inspection of the instantaneous velocity field from the inlet to Y/D=0.6 indicates the presence of an axial acceleration on the jet core induced by the helical vortices, as testified by the iso-surface of V/V_j=1.10. This acceleration in free axisymmetric jets is often referred to as pulsatile motion (Yule, 1978). The contours of $\omega_z D/V_j$ shows maxima (and minima) in the shear layer region located at the helical vortex cores. These structures extend up to Y/D=0.58 with a spacing between two consecutive helical vortices of about 0.14 D and 0.18 D at left and right sides with respect to the jet axis, respectively. Such difference can be due to the induction effect produced by the entrainment process with a negative flow region, as shown by the orientation of the velocity vectors present on the left side. This effect reduces the convective velocity of the helical vortices exposed to the entrainment region. As a consequence, the jet axis bends towards the wall of the chamber, this mechanism presumably can influence the precessing motion.

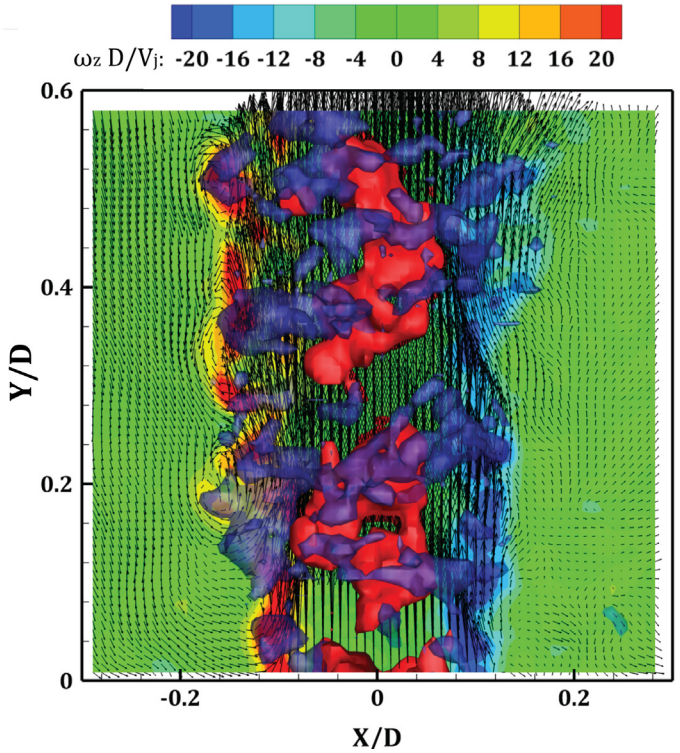

Figure 5.21 Visualization of helical vortices in SER for JWG case identified by the iso-surfaces of $\lambda_2 D/V_j$=-30 (blue)and V/V_j=1.10 (red). Iso-contour of $\omega_z D/V_j$ with in-plane velocity vectors.

Moving downstream 0.6<Y/D<1.0, the instantaneous flow field exhibits a more complex pattern characterized by streamwise filaments of axial and azimuthal vorticity as shown in Figure 5.22. However, the limited spatial resolution of the present measurements does not suffice for a conclusive understanding on these structures. The iso-surface of V/V_j=1.05 indicates the presence of a patch of flow at higher axial velocity induced by streamwise vortex filaments. At the radial position X/D=-0.18, the combined effect of the entrainment, together with the axial development of the jet, produces two recirculation regions at Y/D=0.69 and 0.77 with azimuthal velocities V_θ/V_j=-0.16 and -0.29, respectively.

Figure 5.23 illustrates the distribution and strength of the vortex filaments $\omega_y D/V_j$ in the cross-sectional planes Y/D=0.10, 0.27 and 0.80 with in-plane velocity vectors. At Y/D=0.10, the peaks of the axial vorticity $|\omega_y D/V_j|$>6 are localized in the shear layer (R/D=0.12). As shown by the in-plane velocity vectors, they are subjected to a swirl motion of V_θ/V_j=0.14.

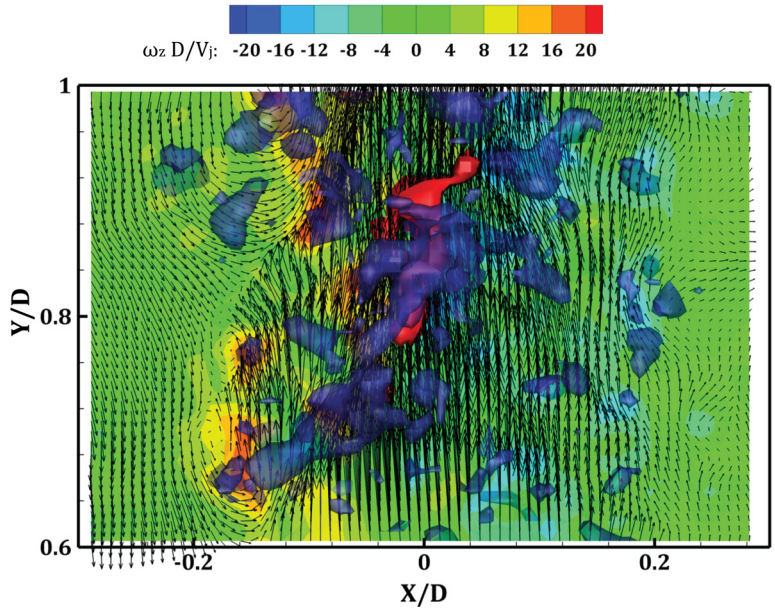

Figure 5.22 Visualization of streamwise and radial vortices in SER for JWG case identified by the iso-surfaces of $\lambda_2 D/V_j$=-30 (blue) and V/V_j=1.05 (red). Iso-contour of $\omega_z D/V_j$ with in-plane velocity vectors.

The cross-sectional map at Y/D=0.27 illustrates 6 counter-rotating vortices, that contribute to the elongation and compression of the helical structures, with magnitude of $\omega_y D/V_j$ ranging from 8 to 20. A detailed inspection of the contour map reveals the presence of 4 additional inner streamwise structures at radial distance R/D=0.082; they are counter-rotating with respect to the external streamwise filaments. On the opposite side respect to the entrainment region, the swirl motion exhibits a weaker intensity if compared to that observed at Y/D=0.1. In addition, an azimuthal motion of V_θ/V_j=-0.16, in opposite direction with respect to the swirl one, is detected on the upper-right side at R/D=2.2. Moving downstream, at Y/D=0.80 the azimuthal motion covers the entire right-side of the cross-sectional plane with a rather uniform azimuthal velocity profile of V_θ/V_j=-0.14. However, the absolute axial vorticity of the streamwise filaments remains rather the same covering scattered positions in the periphery of the jet axis.

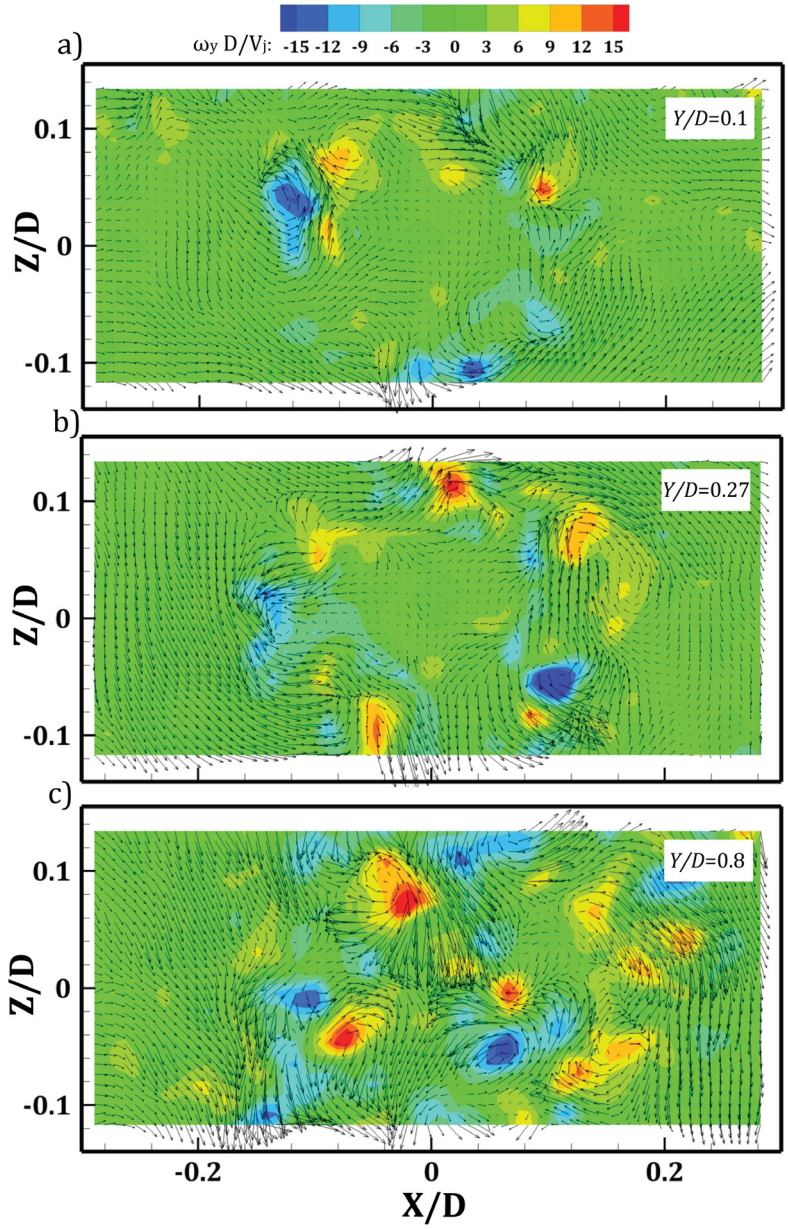

Figure 5.23 Iso-contours of axial vorticity component $\omega_y D/V_j$ at cross-sectional planes Y/D=0.1 (a), 0.27 (b) and 0.8 (c) with in-plane velocity vectors.

5.4.2 Flow topology in MIR

The temporal sequence based on the evolution of the entrainment process in MIR is illustrated in Figure 5.24 with snapshots separated in time by $\Delta t_{ac} V_j/D$=1.41, where Δt_{ac} represents the delay time between two subsequent acquired snapshots and is equal to the inverse of the acquisition frequency (0.067 s). The iso-surface of V/V_j=0.7 (in yellow) identifies the jet column, while V/V_j=-0.20 (in blue) represents the entrainment bubble. In order to visualize the main features of the flow field, iso-contours of normalized axial velocity are depicted on cross-sectional planes at Y/D=0.97, 1.25, 1.55 and 1.83 with in-plane velocity vectors. The flow field exhibits fully turbulent features with axial and radial filaments identified by the iso-surface of $\lambda_2 D/V_j$=-35 (in cyan). During the periodic entrainment process, these vortical structures are localized in the surrounding of the jet column with a scattered orientation. Similar vortex filaments were observed by Violato and Scarano (2011) downstream the potential core of an axisymmetric jet issuing at Re=5,000.

In Figure 5.24a, on the right-top side with respect to the jet column the negative axial velocity identifies the incipient entrainment bubble extending from Y/D=1.62 to 2.0. Moving upstream, the axial velocity decreases in magnitude reaching roughly a zero value on the planes Y/D=0.97 and 1.25, indicating the presence of a quiescent region located on the right bottom side of the volume. At the jet axis, the jet column is surrounded by vortex filaments mostly oriented along the azimuthal and radial directions.

At tV_j/D=1.41 (Figure 5.24b), the patch of flow of negative axial velocity moves upstream down to Y/D=1.34, mainly localized across the sectional plane Y/D=1.55. It is worth to note that this entrainment bubble induces an ejection of fluid towards the wall with peaks of instantaneous radial velocity of V_r/V_j=0.18. In the periphery of the bubble, the crosstalk between the entrainment process and the jet column produces a vortex filament (indicated in Figure 5.24b as 'vortex') without any convective velocity. It is oriented along the azimuthal direction at Y/D=1.55 and embraces the jet across the entire deep of the measurement volume. At Y/D=1.15, an engulfment of flow in radial direction towards the jet column is detected with peaks of V_r/V_j=-0.12. The combination of the ejection and the radial engulfment, both acting asymmetrically long the streamwise direction, imparts to the jet column a wave-like pattern characterized by two wave numbers along the streamwise and crosswise directions.

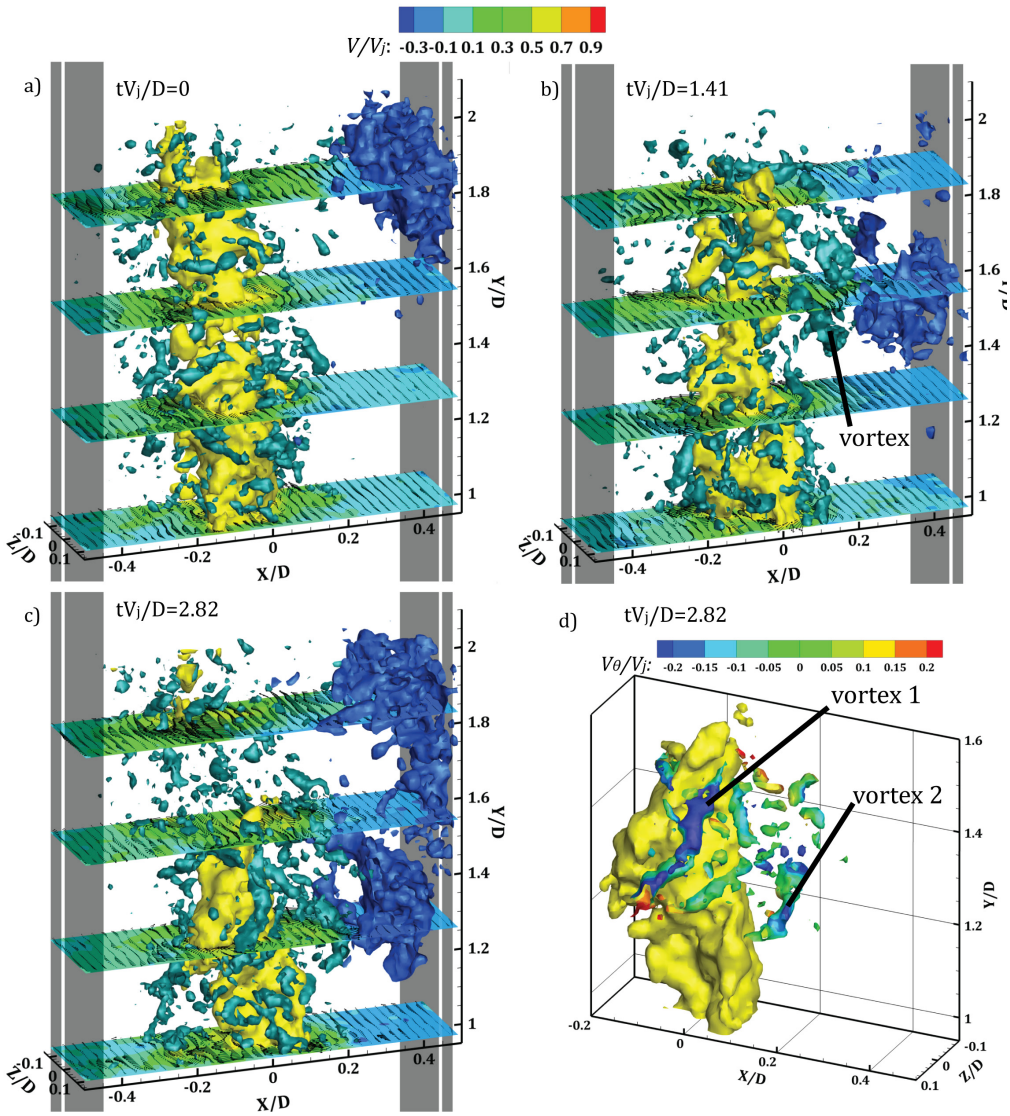

Figure 5.24 Time sequence of the periodic entrainment process in MIR. Iso-surfaces of axial velocity V/V_j=0.7 (yellow) and V/V_j=-0.2 (blue). Iso-contour of axial velocity on the cross-sectional planes Y/D=0.97,1.25, 1.55 and 1.83 with in-plane velocity vectors. Vortex representation using λ_2 criterion, iso-surface of $\lambda_2 D/V_j$=-35 (cyan); sub-figure (d) presents the instantaneous realization at tV_j/D=2.82 with the iso-surfaces of V/V_j=0.7 and $\lambda_2 D/V_j$ =-35 (this latter color-coded with the azimuthal velocity component) at a different isometric view.

At tV_j/D=2.82 (Figure 5.24c), the entrainment bubble moves upstream down to Y/D=1.25. Furthermore, a pursuer bubble is detected at Y/D=1.83. The presence of the pursuer patch flow can be ascribed by the intermittently behaviour of the PJ mode.

However, the leading bubble continues to induce the radial ejection of flow with peaks of V_r/V_j=0.11. By inspecting the periphery of the jet column, two main vortex filaments (indicated in Figure 5.24d as 'vortex 1' and 'vortex 2') are observed in the shear layer and in the neighbour of the leading bubble. Figure 5.24d presents the instantaneous realization at tV_j/D=2.82 (Figure 5.24c) with the iso-surfaces of V/V_j=0.7 and $\lambda_2 D/V_j$=-35 (this latter color-coded with the azimuthal velocity component) at a different isometric view, in order to better illustrate the spatial organization of 'vortex 1' and 'vortex 2'. In particular, the first vortex embraces the jet column with a convective velocity of V/V_j=0.7 and induces an azimuthal motion with V_θ/V_j=-0.15. It is predominantly oriented along the streamwise direction. On the other hand, the second vortex exhibits similar kinetic features of that described at tV_j/D=1.41. It is located at axial location Y/D=1.3 and oriented along the azimuthal direction.

5.4.3 Flow topology in EJR

A temporal evolution describing the entrainment process in EJR is depicted in Figure 5.25 by a sequence of snapshots with a time separation equal to that already considered in Section 5.4.2. The iso-surface of V/V_j=0.30 (in red) indicates the emerging jet issuing at the exit of the cylindrical chamber. The main features of the flow field are illustrated by iso-contours of normalized axial velocity component on the cross-sectional plane Y/D=2.0 and on the axial plane Z/D=0 with velocity vectors. In each instantaneous realization, the inflow, represented by the negative axial velocity, is sustained by a bulk of fluid coming from both the ambient and the emerging jet itself. On the right-top side in each instantaneous realization (Figure 5.25), the entrainment process induces a suction effect that advects the ambient fluid, in rather quiescent conditions, into the chamber. At the exit edge (Y/D=2.75), the fluid enters with V/V_j=-0.13 and moves upstream. The axial velocity component reaches a minimum of V/V_j=-0.20 at Y/D=2.22. As reported by Wong et al. (2004), the combination of both the entrainment process and the emerging jet determines a pressure gradient along the crosswise direction. It is clearly illustrated by the roll-up of the velocity vectors. In Figure 5.25a, on the plane Y/D=2.0 the emerging jet, issuing with a maximum axial velocity of V/V_j =0.47, is characterized by an azimuthal velocity component of V_θ/V_j=0.14 (not shown in Figure 5.25) rather uniform between -0.29<X/D<0.034. Moving towards the wall (X/D≥0), the axial and azimuthal velocity components decrease to zero-values approximately at X/D=0, and then switch in sign reaching an axial

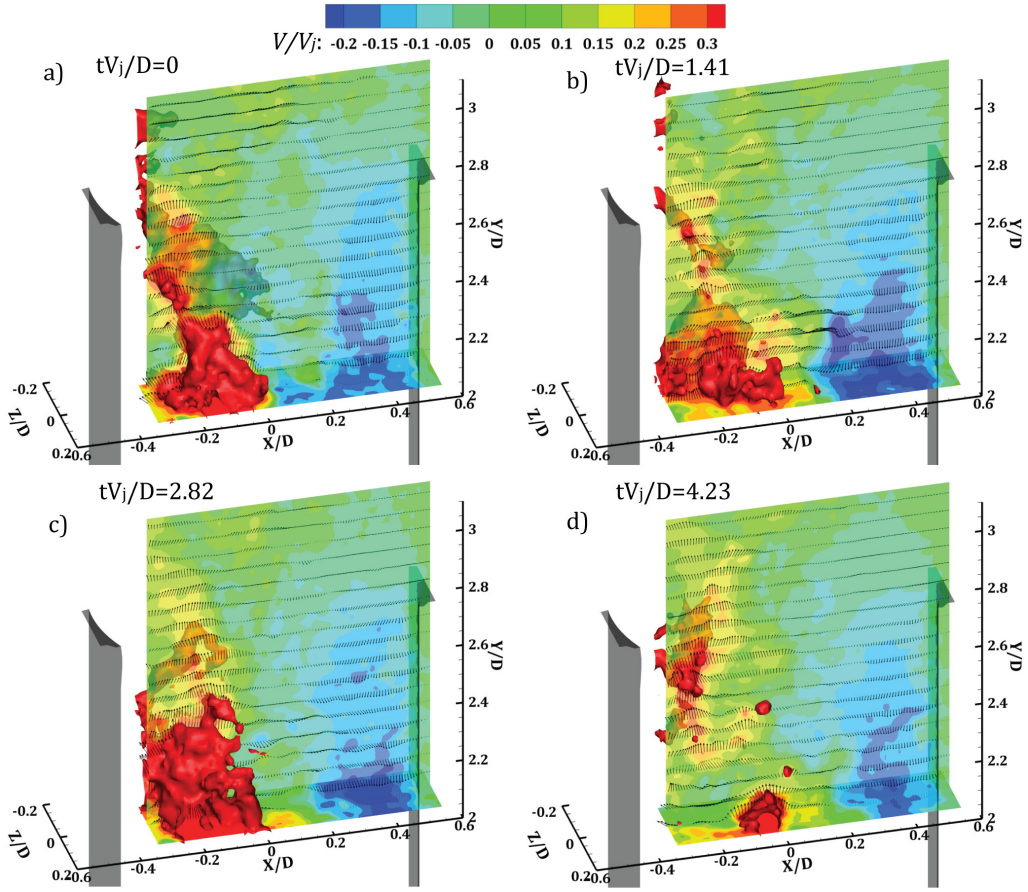

Figure 5.25 Time sequence of the periodic entrainment process in EJR. Iso-surface of axial velocity V/V_j=0.30 (red). Iso-contours of axial velocity represented on the cross-sectional plane Y/D=2.0 and on the axial plane Z/D=0 with velocity vectors placed each seven measured points along the streamwise direction.

and azimuthal velocity components of -0.17 and -0.067, respectively. Interesting enough, the radial velocity increases up to V_r/V_j=0.11 at X/D=0.1. At Y/D=2.9, the axial velocity decreases down to 0.42 (90% of that detected at Y/D=2.0), that is, the same order of magnitude of the radial and azimuthal velocity components. A similar pattern can be observed in the instantaneous realizations during the evolution of the entrainment process (Figure 5.25b-d).

Furthermore, the entrainment determines a deflection of the emerging jet towards the opposite side of the chamber where the inflow is established. Similar observations were outlined by Wong et al. (2008), who investigated the flow organization at the exit of a PJ nozzle equipped with a centrebody. They pointed out from phase-averaged planar PIV

measurements that the emerging angle of deflection β, defined as the complementary of the angle formed between the main direction of the emerging jet and the axis of the cylindrical chamber, is equal to β=53° within the near field of the PJ nozzle exit. In this investigation, the deflection angle in each instantaneous realization is measured by the orientation of the velocity vectors on the axial plane at Y/D=2.79 for each instantaneous realization. It results approximately to be β=54° in agreement with that found by Wong et al. (2008). Furthermore, it is worth to note that a weak recirculation region enclosed between the emerging jet and the inflow region is observed. It extends approximately between 2.1<Y/D<2.9.

5.5 Final remarks

The three-dimensional organization of a PJ flow at Re_d=42,500 has been investigated with tomographic PIV for two inflow conditions by using either simply a short-pipe nozzle JWG or placing a regular grid RG at a short pipe exit. The jet issues in a coaxial cylindrical chamber with expansion ration 5:1 and length of 2.75 the chamber diameter.

The present measurements confirm that the driving force of the precession is the inertial effect induced by the asymmetric entrainment on the opposite side of that of the outflow (Nathan et al. 1998). The entrainment region is extended along the chamber and interacts with an asymmetric recirculation zone, placed right below the exiting jet and extending down to the basis of the chamber.

The mean flow characteristics in SER indicate that the effect of the entrainment is present for both JWG and RG cases; in addition, when the jet passes through the regular grid, a residual azimuthal velocity component has been detected at the basis of the cylindrical chamber indicating a more pronounced PJ mode activity. As for the free submerged jets (Yule, 1978), the overall turbulence is localized in the shear layer for both configurations. For the RG case, an increment of turbulence has been observed at the inlet along the centreline, while at the end of the potential core it spreads more uniformly across the axial direction. In MIR, the entrainment is located at the periphery of the jet core for both configurations. The average flow field of the JWG exhibits an inward motion along the crosswise direction in the first half of the measurement volume, while an inversion occurs further downstream. For the RG case, the swirl motion still persists at the periphery of the jet, it can be ascribed to the PJ mode. In terms of produced turbulence, the centreline distribution of the fluctuations is constant for both configurations, while

along the crosswise direction the JWG exhibits a more coherent azimuthal distribution than that observed in the RG flow field. In EJR, the average flow field shows for both configurations that the entrainment process induces an inward motion at the exit of the cylindrical chamber, it is found stronger near the external edge. On the other hand, an outward motion associated with the PJ mode activity has been observed in the internal average flow field. The overall turbulence decreases along the streamwise direction, its spreading is larger in proximity of the chamber exit, while further downstream, is localized in the periphery of the axis of the chamber.

The 3D flow organization in SER is statistically investigated by applying the POD technique to the velocity field. The analysis is focused on the first 10 modes, that collect 22% and 31% of the total kinetic energy for JWG and RG, respectively. The first pair of modes describes the precessing motion of the PJ mode. Precession and helical motions of the jet column are also observed from the axial fluctuation. On the other hand, radial and azimuthal fluctuations indicate the presence of wave-like and twisting motions at the end of the potential core.

The intricate instantaneous velocity field for the JWG case has been investigated in order to highlight the influence of the entrainment on the organization of the large-scale coherent structures. The 3D vortex analysis has been carried out using vorticity and the λ_2-criterion.

In SER, the induced swirling flow generates helical vortices within the near field of the jet. These structures evolve along the streamwise direction for about $3d$, where their coherence ceases and the vortices merge according to the pairing phenomenon. Surprisingly enough, the formation of vortex rings due to the Kelvin–Helmholtz instability (visualized in free JWG conditions) does not occur, as it is replaced by the helical vortices. This leads to the conclusion that the PJ issued from a short pipe behaves much more like a swirling jet than a round jet also in the near field.

In MIR, vortex filaments have been observed in the surrounded region around the jet column. These structures are mostly oriented along the azimuthal and radial directions and evolve together with the jet column. Furthermore, it has been found that the crosstalk between the entrainment and the jet column produces a vortex filament characterized by a zero convective velocity.

In EJR, the entrainment process is sustained by a bulk of fluid coming from both the external ambient and the emerging jet. This causes a deflection of the exiting jet towards

the opposite side of the chamber where the inflow is established. The measured emerging angle of deflection is equal to 54°, in agreement with that reported by Wong et al. (2008). Furthermore, a weak recirculation region enclosed between the emerging jet and inflow has been observed across the exit of the cylindrical chamber.

Chapter 6

Conclusions and perspectives

In this thesis, an experimental investigation on swirl and precession in free and confined submerged jets has been carried out in cold flow conditions by means of tomographic particle image velocimetry. The experiments have been conducted in a tailored water jet facility. A high swirling flow is generated by a lean pre-vaporized premixed LPP injector for aero-engine applications. Whereas, a precessing jet PJ is obtained by a fluidic PJ nozzle. The research study has been taken on since swirling jets, in free and confined configurations, present many similarities to PJs in terms of generation mechanisms and flow features. Moreover, the PJ has been investigated for two inflow conditions using either a short-pipe nozzle (jet without grid JWG) or placing a regular grid RG at the inlet.

Firstly, the inflow of the fluidic PJ nozzle has been investigated for the JWG configuration without its cylindrical chamber in order to discard the presence of asymmetries and residual bias. To this purpose, the axial-symmetry of the inlet condition has been verified using planar PIV measurements at different Reynolds numbers (Re_d=150,000 and 16,000).

Since the presence of a reverse flow together with a well-stabilized precessing vortex core PVC is expected in high swirl flows, first efforts have been placed upon the study of the flow field generated by the LPP injector issuing at Re_{D_S}=50,000. The 3D organization of large-scale coherent structures has been inspected in free and confined configurations (this latter with an expansion ratio of 3:1). It has been found that their pattern is dramatically altered under the effect of the confinement. The mean flow characteristics show the dominance of the vortex breakdown for both configurations leading to the formation of an inner recirculation zone IRZ, which is wider in crosswise direction for the confined case. This effect has been found to promote also a larger spreading angle of 36°, which is two times larger than that measured for the free case. Furthermore, even though the degree of the geometrical swirl is the same for both configurations, the measured swirl number for the confined swirling jet is 41% higher (S=1.27) than that detected for the free configuration (S=0.90). For the confined case, an increase of the overall

turbulence in proximity of the nozzle exit has been detected. It has suggested that the level of mixing is locally enhanced, thus confirming that confined swirling jets are very suitable for combustion applications. The instantaneous flow field has been investigated in order to elucidate more insights on the spatial development of the PVC. In addition to this, an outer helical vortex has been detected in the external periphery of the PVC. Small turbulent structures of radial vorticity have been recognized probably responsible of azimuthal instabilities of the PVC and leading to its dissipation further downstream.

POD analysis based on the velocity vector field has been used to study how the large-scale coherent structures participate to the built-up of the overall turbulent kinetic energy. It has been found that the first two POD modes are the most energetics and represent the PVC and the outer helical vortex. They are located between an inner and outer shear layers. Subsequently, a low order reconstruction LOR, based on the superposition of the mean flow field and the first two POD modes, has been compared to the instantaneous velocity field. However, the small azimuthal and radial coherent structures, represented in the instantaneous realization, are not captured in the LOR representation.

From these considerations, the aim of the research has been driven on the study of large-scale coherent structures arising into the cylindrical chamber of the fluidic PJ nozzle. The PJ issues at Re_d=42,500, when the precession is established. In order to spatially resolve the 3D complex flow field, the entire probed volume has been investigated capturing three different velocity regions, i.e., sudden expansion region SER, middle internal region MIR and exit jet region EJR.

The global features of the PJ flow field have confirmed that the inertial effect due to the asymmetric entrainment is the driving force of the precession. For both the JWG and RG inlet conditions, the mean velocity field is characterized by an average entrainment along the axial direction. At the basis of the cylindrical chamber for the RG case, the presence of a residual azimuthal velocity component has suggested a more pronounced attitude of the jet to precess. In terms of produced turbulence, the turbulent kinetic energy TKE reaches its maximum intensity at approximately half of the chamber length for both cases.

The analysis of the 3D patterns has been aided by applying POD analysis to the velocity vector field in SER. It has been observed that the precessing motion is captured by the first pair of modes. Moreover, precession and helical motions of the jet, captured by

the successive modes, indicate an asymmetric pattern of the coherent structures in the shear layer of the jet, in contrast with that observed in the early POD analysis conducted for the free jet in JWG configuration.

Finally, a fundamental study on the instantaneous flow field under the entrainment effect has been carried out for the JWG case. It has been observed that the swirl motion localized at the basis of the chamber replaces the axisymmetric ring vortices with helical structures. This pattern evolves along the axial direction and, then, ceases its coherence further downstream. This behaviour has led to the conclusion that the PJ behaves much more like a swirling jet than a round jet especially in the near field. Moreover, it has been found that the crosstalk between the entrainment and the jet produces the coexistence of vortex filaments characterized by a zero convective velocity. An important topological feature has been drawn by inspecting the evolution of the precessing motion at the exit of the fluidic PJ nozzle. The deflection of the emerging jet towards the opposite side of the chamber is caused by the combined activity of the fluid coming from the ambient and the jet itself, thus forming a weak recirculation region across the exit of the chamber.

In conclusions, this experimental investigation has brought out more insights on the 3D flow patterns of swirling flows characterized by either a periodic-stable precessing helical structure or intermittent bi-stable fluidic mechanism that produces large scale precession motion. Ultimately, tomographic PIV has definitely shown to be suitable for the investigation of the large scale organization of flow fields with extremely complex 3D features, such as swirling and precessing jets.

6.1 Future works

The outlined achievements drawn in the present thesis have led to a better understanding about the spatial organization of the large scale coherent structures in flow fields of swirling and precessing jets. Both the investigated flows have been brought out their intrinsic 3D complexity leading to results representative of a unique 3D dataset among the others present in literature.

Nevertheless, there are many other aspects relative the swirling and precessing jets in terms of their dynamic evolution, which require to be investigated more in deep. An attempt has been made in the present work by resolving in time the precession of the precessing jets, but a complete description of the dynamic behaviour of the large scale coherent structures requires 4D measurements, i.e., to make measurements simultaneously resolved in space and time. In this context, a comprehensive description of

the large scale structures of the precessing motion and that embedded in the shear layer can be addressed using time resolved tomographic particle image velocimetry.

Some observations, brought out from the present modal analysis, highlight the requirement of an axisymmetric measurement volume (e.g. cylindrical-shape) for both swirling and precessing jets in order to capture the entire development of the helical vortices, that, as widely described in the present work, strongly feature these flow fields.

References

Abramovich, G. (1963). *The Theory of Turbulent Jets.* Cambridge, The Massachussets Institute of Technology, Press.

Adrian, R. (1991). Particle imaging techniques for experimental fluid mechanics. *Annal Rev Fluid Mech*, *23*, 261–304.

Adrian, R. J., and Yao, C. S. (1984). Development of pulsed laser velocimetry (PLV) for measurement of turbulent flow. *In Symposum of Turbulence,* 170–186.

Alkislar, M. B., Krothapalli, A. and Butler, G. W. (2007). The effect of streamwise vortices on the aeroacoustics of a Mach 0.9 jet. *Journal of Fluid Mechanics, 578*. http://doi.org/10.1017/S0022112007005022

Astarita, T. (2008). Analysis of velocity interpolation schemes for image deformation methods in PIV. *Experiments in Fluids*, *45 (2), 257–266*. http://doi.org/10.1007/s00348-008-0475-7

Astarita, T. (2009). Adaptive space resolution for PIV. *Experiments in Fluids*, *46*(6), *1115–1123.* http://doi.org/10.1007/s00348-009-0618-5

Babazadeh, H., Koch, C. R., and Nobes, D. S. (2011). Investigation of micro-jet active control of a precessing jet using PIV. *Experiments in Fluids*, *51*(6)*, 1709–1719.* http://doi.org/10.1007/s00348-011-1193-0

Battaglia, F., Tavener, S. J., Kulkarni, A. K., and Merkle, C. L. (1997). Bifurcation of low Reynolds number flows in symmetric channels. *AIAA Journal*, *35*(June), *99–105.* http://doi.org/10.2514/3.13469

Baum, E., Peterson, B., Surmann, C., Michaelis, D., Böhm, B., and Dreizler, A. (2013). Investigation of the 3D flow field in an IC engine using tomographic PIV. *Proceedings of the Combustion Institute*, *34*(2), *2903–2910*. http://doi.org/10.1016/j.proci.2012.06.123

Berkooz, G., Holmes, P., and Lumley, J. L. (1993). The Proper Orthogonal Decomposition in the analysis of turbulent flows. *Annu. Rev. Fluid Mech., 25, 539–575.*

Birzer, C. H., Kalt, P. a M., and Nathan, G. J. (2011). The influences of jet precession on large-scale instantaneous turbulent particle clusters. *International Journal of Multiphase Flow*, *37(4), 394–402.* http://doi.org/10.1016/j.ijmultiphaseflow.2010.12.003

Bradshaw, P., Ferriss, D. H., and Johnson, R. F. (1964). Turbulence in the noise-producing region of a circular jet. *Journal of Fluid Mechanics*, *19*(04), *591–624.* http://doi.org/10.1017/S0022112064000945

Buckingham, E. (1914). On phisically similar systems: illustrations of the use of dimensional equations. *Physically Similar Systems*, *4*, *345–376.* http://doi.org/10.1017/CBO9781107415324.004

Cabral, B., and Leedom, L. C. (1993). Imaging vector fields using line integral convolution. In *20th Annual Conference on Computer Graphics and Interactive Techniques (SIGGRAPH) 263–270*. http://doi.org/10.1145/166117.166151

Cafiero, G., Ceglia, G., Discetti, S., Ianiro, A., Astarita, T., and Cardone, G. (2014). On the three-dimensional precessing jet flow past a sudden expansion. *Experiments in Fluids*, *55*(2), *1677*. http://doi.org/10.1007/s00348-014-1677-9

Cala, C. E., Fernandes, E. C., Heitor, M. V., and Shtork, S. I. (2006). Coherent structures in unsteady swirling jet flow. *Experiments in Fluids*, *40*(2), *267–276.* http://doi.org/10.1007/s00348-005-0066-9

Candel, S. M. (1992). Combustion instabilities coupled by pressure waves and their active control. *Symposium (International) on Combustion*, *24*(1), *1277–1296*. http://doi.org/10.1016/S0082-0784(06)80150-5

Cassidy, J. J., and Falvey, H. T. (1970). Observations of unsteady flow arising after vortex breakdown. *Journal of Fluid Mechanics*, *41*(4), *727–736.*

Ceglia, G., Discetti, S., Ianiro, A., Michaelis, D., Astarita, T., and Cardone, G. (2014). Three-dimensional organization of the flow structure in a non-reactive model aero engine lean burn injection system. *Experimental Thermal and Fluid Science*, *52*, *164–173.* http://doi.org/10.1016/j.expthermflusci.2013.09.007

Chanaud, R. C. (1965). Observations of oscillatory motion in certain swirling flows. *Journal of Fluid Mechanics*, *21*, *111–127*.

Chiekh, M. Ben, Michard, M., Grosjean, N., and Béra, J.-C. (2004). Reconstruction temporelle d'un champ aérodynamique instationnaire à partir de mesures PIV non résolues dans le temps. In *9e Congrès Francophone de Vélocimétrie Laser,* 81, *14–17*.

Chigier, N. a., and Chervinsky, A. (1967). Experimental Investigation of Swirling Vortex Motion in Jets. *Journal of Applied Mechanics*, *34*(2), *443–451*. http://doi.org/10.1115/1.3607703

Debasish Mishra, K. Muralidhar, P. (1999). a Robust Mart Algorithm for Tomographic Applications. *Numerical Heat Transfer, Part B: Fundamentals*, *35*(4), *485–506.* http://doi.org/10.1080/104077999275857

Dellenback, P., Metzger, D., and Neitzel, G. (1988). Measurement in turbulent swirling flows through an abrupt axisymmetric expansion. *AIAA Journal*, *13*(4), *669–681*.

Discetti, S. (2013). Tomographic Particle Image Velocimetry Developments and applications to turbulent flows. *PhD Thesis, University of Naples "Federico II."*

Discetti, S., and Adrian, R. J. (2012). High accuracy measurement of magnification for monocular PIV. *Measurement Science and Technology*, *23*(11), *117001*. http://doi.org/10.1088/0957-0233/23/11/117001

Discetti, S., and Astarita, T. (2012a). A fast multi-resolution approach to tomographic PIV. *Experiments in Fluids*, *52*(3), *765–777*. http://doi.org/10.1007/s00348-011-1119-x

Discetti, S., and Astarita, T. (2012b). Fast 3D PIV with direct sparse cross-correlations. *Experiments in Fluids*, *53*(5), *1437–1451*. http://doi.org/10.1007/s00348-012-1370-9

Discetti, S., Natale, A., and Astarita, T. (2013). Spatial filtering improved tomographic PIV. *Experiments in Fluids*, *54*(4), *1–13*. http://doi.org/10.1007/s00348-013-1505-7

Doherty, T. O., Froud, D., Bates, C. J., and Syred, N. (1994). Characteristics of a power station boiler, *208*(2), *89–101*.

Dulin, V. M., Markovich, D. M., Tokarev, M. P., and Chikishev, L. M. (2012). Application of Modern Optical Methods for Detecting the Spatial Structure of Turbulent Flames. *Optoelectronics, Instrumentation and Data Processing*, *48*(3), *235–243*. http://doi.org/10.3103/S875669901203003X

El Hassan, M., and Meslem, A. (2010). Time-resolved stereoscopic particle image velocimetry investigation of the entrainment in the near field of circular daisy-shaped orifice jets. *Physics of Fluids*, *22*(3), *7–26*. http://doi.org/10.1063/1.3358465

Elsinga, G. E., Scarano, F., Wieneke, B., and Van Oudheusden, B. W. (2006). Tomographic particle image velocimetry. *Experiments in Fluids*, *41*(6), *933–947*. http://doi.org/10.1007/s00348-006-0212-z

Elsinga, G. E., Van Oudheusden, B. W., and Scarano, F. (2006). Experimental assessment of Tomographic-PIV accuracy. *In 13th Int Symp on Applications of Laser Techniques to Fluid Mechanics*, *26–29*.

Escudier, M. P., and Zehnder, N. (1982). Vortex-flow regimes. *Journal of Fluid Mechanics*, *115*, *105–121*.

Fröhlich, J., García-Villalba, M., and Rodi, W. (2008). Scalar mixing and large-scale coherent structures in a turbulent swirling jet. *Flow, Turbulence and Combustion*, *80*(*1*), *47–59*. http://doi.org/10.1007/s10494-007-9121-3

García-Villalba, M., Fröhlich, J., and Rodi, W. (2006). Identification and analysis of coherent structures in the near field of a turbulent unconfined annular swirling jet using large eddy simulation. *Physics of Fluids*, *18*(*5*), *1–18*. http://doi.org/10.1063/1.2202648

Gupta, A. K., Lilley, D. G., and Syred, N. (1984). *Swirl flows*. Energy and engineering science Series, Abacus Pre. London.

Gursul, I. (1993). Effect of nonaxisymmetric forcing on a swirling jet with vortex breakdown. *In AIAA, Shear Flow Conference, 46, 385–394*, Orlando, FL.

Gutmark, E., Parr, T. P., Hanson-Parr, D. M., and Schadow, K. C. (1989). On the Role of Large and Small-Scale Structures in Combustion Control. *Combustion Science and Technology*, *66*(*1-3*), *107–126*. http://doi.org/10.1080/00102208908947142

Hall, M. G. (1967). A new approach to vortex breakdown. *In Heat transactions and fluid mechanics institute*, *319–40*, San Diego: University of California.

Hallett, L. H., and Gunther, R. (1984). Flow and Mixing in Swirling Flow in a Sudden Expansion. *Canadian Journal of Chemical Engineering*, *62*, *149–155*.

Harvey, J. K. (1962). Some observations of the vortex breakdown phenomenon. *Journal of Fluid Mechanics*, *14*, 585. http://doi.org/10.1017/S0022112062001470

Herman, G. T., and Lent, A. (1976). Iterative reconstruction algorithms. *Computers in Biology and Medicine*, *6*(*4*), *273–294*. http://doi.org/10.1016/0010-4825(76)90066-4

Hill Jr., W. G., and Greene, P. R. (1977). Increased turbulent jet mixing rates obtained by self-excited acoustic oscillations. *Journal of Fluids Engineering*, *99*(*77*), *520–525*.

Hill, S. J., Nathan, G. J., and Luxton, R. E. (1992). Precessing and axial flows following a sudden expansion in an axisymmetric nozzle. *In 11th Australian Fluid Mechanics Conference University of Tasmania, Hobart, Australia, 14-18 December*, *1113–1116*.

Huang, H. T., Fiedler, H. E., and Wang, J. J. (1993). Limitation and improvement of PIV. *Experiments in Fluids*, *15-15*(4-5), *263–273*. http://doi.org/10.1007/BF00223404

Huang, R. F., Jufar, S. R., and Hsu, C. M. (2013). Flow and mixing characteristics of swirling double-concentric jets subject to acoustic excitation. *Experiments in Fluids*, *54*(1), *1421-1444*. http://doi.org/10.1007/s00348-012-1421-2

Iqbal, M. O., and Thomas, F. O. (2007). *Coherent structure in a turbulent jet via a vector implementation of the proper orthogonal decomposition*. *Journal of Fluid Mechanics 571, 281–326*. http://doi.org/10.1017/S0022112006003351

Jeong, J., and Hussain, F. (1995). On the identification of a vortex. *Journal of Fluid Mechanics*, *285*, *69–94*.

Keane, R. D., and Adrian, R. J. (1992). Theory of cross-correlation analysis of PIV images. *Applied Scientific Research*, *49*(*3*), *191–215*. http://doi.org/10.1007/BF00384623

Kelso, R. M. (2001). A Mechanism for Jet Precession in Axisymmetric Sudden Expansions. *In 14th Australasian Fluid Mechanics Conference* (pp. 829–832).

Krause, E. (1985). A contribution to the problem of vortex breakdown. *Computers & Fluids*, *13*(*3*), *375–381*. http://doi.org/10.1016/0045-7930(85)90008-8

Lee, S., Lanspeary, P., Nathan, G., Kelso, R., and Mi, J. (2001). Preliminary study of oscillating triangular jets. *In 14th Australasian Fluid Mechanics Conference*, *821–824*.

Leibovich, S. (1978). The structure of vortex breakdown. *Annal Rev Fluid Mech*, *10*, *221–246*. http://doi.org/10.1080/00958979009408200

Liang, H., and Maxworthy, T. (2005). An experimental investigation of swirling jets. *Journal of Fluid Mechanics*, *525*, *115–159*. http://doi.org/10.1017/S0022112004002629

Liepmann, D., and Gharib, M. (1992). The role of streamwise vorticity in the near-field entrainment of round jets. *Journal of Fluid Mechanics*, *245*, *643–668*. http://doi.org/10.1017/S0022112092000612

Lilley, D. G. (1977). Swirl Flows in Combustion: A Review. *AIAA Journal*, *15*(*8*), *1063–1078*. http://doi.org/10.2514/3.60756

Lucca-Negro, O., and O'Doherty, T. (2001). Vortex breakdown: A review. *Progress in Energy and Combustion Science*, *27*(*4*), *431–481*. http://doi.org/10.1016/S0360-1285(00)00022-8

Maas, H. G., Gruen, A., and Papantoniou, D. (1993). Particle tracking velocimetry in three-dimensional flows. *Experiments in Fluids*, *15*(*2*), *133–146*. http://doi.org/10.1007/BF00190953

Madej, A. M., Babazadeh, H., and Nobes, D. S. (2011). The effect of chamber length and Reynolds number on jet precession. *Experiments in Fluids*, *51*(*6*), *1623–1643*. http://doi.org/10.1007/s00348-011-1177-0

Masri, A. R., Kalt, P. A. M., and Barlow, R. S. (2004). The compositional structure of swirl-stabilised turbulent nonpremixed flames. *Combustion and Flame*, *137*(*1-2*), *1–37*. http://doi.org/10.1016/j.combustflame.2003.12.004

Mi, J., and Nathan, G. (2004). Self-excited jet-precession Strouhal number and its influence on downstream mixing field. *Journal of Fluids and Structures*, *19*(6), 851–862. http://doi.org/10.1016/j.jfluidstructs.2004.04.006

Mi, J., and Nathan, G. J. (2005). Statistical analysis of the velocity field in a mechanical precessing jet flow. *Physics of Fluids*, *17*(*1*), *015102*. http://doi.org/10.1063/1.1824138

Mi, J., Nathan, G. J., and Luxton, R. E. (2001). Mixing characteristics of a flapping jet from a self-exciting nozzle. *Flow, Turbulence and Combustion*, *67*, *1–23*.

Mi, J., Nathan, G. J., and Nobes, D. S. (2001). Mixing Characteristics of Axisymmetric Free Jets From a Contoured Nozzle, an Orifice Plate and a Pipe. *Journal of Fluids Engineering*, *123*(4), *878*. http://doi.org/10.1115/1.1412460

Moeck, J. P., Bourgouin, J. F., Durox, D., Schuller, T., and Candel, S. (2012). Nonlinear interaction between a precessing vortex core and acoustic oscillations in a turbulent swirling flame. *Combustion and Flame*, *159*(8), *2650–2668*. http://doi.org/10.1016/j.combustflame.2012.04.002

Mugridge, B. D. (1980). Combustion driven oscillations. *Journal of Sound and Vibration*, *70*(*3*), *437–452*. http://doi.org/10.1016/0022-460X(80)90311-9

Mungal, M. G., Karasso, P. S., and Lozano, A. (1991). The Visible Structure of Turbulent Jet Diffusion Flames: Large-Scale Organization and Flame Tip Oscillation. *Combustion Science and Technology*, *76*(4-6), *165–185*. http://doi.org/10.1080/00102209108951708

Nathan, G. J. (1988). *The enhanced mixing burner*. *PhD thesis,* University of Adelaide.

Nathan, G. J., Hill, S. J., and Luxton, R. E. (1998). An axisymmetric "fluidic" nozzle to generate jet precession. *Journal of Fluid Mechanics*, *370*, *347–380*. http://doi.org/10.1017/S002211209800202X

Nathan, G. J., Luxton, R. E. S. A. M., and Smart, J. P. (1992). Reduced NO_x emissions and enhanced large scale turbulence from a precessing jet burner. *In Twenty-Fourth Symposium (International) on Combustion*, *1399–1405*.

Nathan, G. J., Mi, J., Alwahabi, Z. T., Newbold, G. J. R., and Nobes, D. S. (2006). Impacts of a jet's exit flow pattern on mixing and combustion performance. *Progress in Energy and Combustion Science*, *32, 496–538*. http://doi.org/10.1016/j.pecs.2006.07.002

Newbold, G. J. R., Na, G. ., and Luxton, R. E. (1997). Large–Scale Dynamics of an Unconfined Precessing Jet Flame. *Combustion Science and Technology*, *126(1-6), 71–95*. http://doi.org/10.1080/00102209708935669

Newbold, G. J. R., Nathan, G. J., Nobes, D. S., and Turns, S. R. (2000). Measurement and prediction of NO_x emissions from unconfined propane flames from turbulent-jet, bluff-body, swirl, and precessing jet burners. *Proceedings of the Combustion Institute*, *28(1), 481–487*. http://doi.org/10.1016/S0082-0784(00)80246-5

Novara, M., Batenburg, K. J., and Scarano, F. (2010). Motion tracking-enhanced MART for tomographic PIV. *Measurement Science and Technology*, *21*, *035401*. http://doi.org/10.1088/0957-0233/21/3/035401

Novara, M., and Scarano, F. (2012). Performances of motion tracking enhanced Tomo-PIV on turbulent shear flows. *Experiments in Fluids*, *52(4), 1027–1041*. http://doi.org/10.1007/s00348-011-1187-y

O'Doherty, T., Griffiths, A. J., Syred, N., Bowen, P. J., and Fick, W. (2008). Experimental Analysis of Rotating Instabilities in Swirling and Cyclonic Flows. *Developments in Chemical Engineering and Mineral Processing*, *7(3-4), 245–267*. http://doi.org/10.1002/apj.5500070302

Oberleithner, K., Sieber, M., Nayeri, C. N., Paschereit, C. O., Petz, C., Hege, H. C., and Wygnanski, I. (2011). Three-dimensional coherent structures in a swirling jet undergoing vortex breakdown: stability analysis and empirical mode construction. *Journal of Fluid Mechanics*, *679, 383–414*. http://doi.org/10.1017/jfm.2011.141

Paterson, R. W. (1984). Turbofan Mixer Nozzle Flow Field—A Benchmark Experimental Study. *Journal of Engineering for Gas Turbines and Power*, *106(3), 692*. http://doi.org/10.1115/1.3239625

Prasad, A. K. (2000). Stereoscopic particle image velocimetry. *Experiments in Fluids*, *29(2), 103–116*. http://doi.org/10.1007/s003480000143

Raffel, M., Willert, C. E., Wereley, S. T., and Kompenhans, J. (2007). *Particle Image Velocimetry - A Practical Guide*. Second Edition, 92127.

Hunt, J. C. R., Wray A. A. and Moin P. (1988). Eddies, Streams, and Convergence Zones in Turbulent Flows, *Proceedings of the Summer Program*.

Reynolds, W. C., Parekh, D. E., Juvet, P. J. D., and Lee, M. J. D. (2003). Bifurcating and blooming jets. *Annual Review of Fluid Mechanics*, *35(1), 295–315*. http://doi.org/10.1146/annurev.fluid.35.101101.161128

Rodriguez-Martinez, V. M., Dawson, J. R., O'Doherty, T., and Syred, N. (2006). Low-Frequency Combustion Oscillations in a Swirl Burner/Furnace. *Journal of Propulsion and Power*, *22(1), 3–7*.

Roux, S., Lartigue, G., Poinsot, T., Meier, U., and Bérat, C. (2005). Studies of mean and unsteady flow in a swirled combustor using experiments, acoustic analysis, and large eddy simulations. *Combustion and Flame*, *141(1-2), 40–54*. http://doi.org/10.1016/j.combustflame.2004.12.007

Sarpkaya, T. (1971). On stationary and travelling vortex breakdowns. *Journal of Fluid Mechanics*, *45(03), 545*. http://doi.org/10.1017/S0022112071000181

Scarano, F. (2012). Tomographic PIV: principles and practice. *Measurement Science and Technology*, *24(1), 012001*. http://doi.org/10.1088/0957-0233/24/1/012001

Scarano, F., Ianiro, A., Lynch, K., and Cardone, G. (2015). Time - resolved tomographic PIV investigation of multichannel swirling jets, (1965), *15–18*.

Scarano, F., and Poelma, C. (2009). Three-dimensional vorticity patterns of cylinder wakes. *Experiments in Fluids*, *47(1988), 69–83*. http://doi.org/10.1007/s00348-009-0629-2

Schefer, R. W., Namazian, M., Kelly, J., and Perrin, M. (1996). Effect of confinement on bluff-body burner recirculation zone characteristics and flame stability. *Combustion Science and Technology*, *120(1-6), 185–211*. http://doi.org/10.1080/00102209608935573

Schneider, G. M., Froud, D., Syred, N., Nathan, G. J., and Luxton, R. E. (1997a). Velocity measurements in a precessing jet flow using a three dimensional LDA system. *Experiments in Fluids*, *23(2), 89–98*. http://doi.org/10.1007/s003480050089

Schneider, G. M., Hooper, J. D., Musgrove, A. R., Nathan, G. J., and Luxton, R. E. (1997b). Velocity and Reynolds stresses in a precessing jet flow. *Experiments in Fluids*, *22(6), 489–495*. http://doi.org/10.1007/s003480050076

Selle, L., Benoit, L., Poinsot, T., Nicoud, F., and Krebs, W. (2006). Joint use of compressible large-eddy simulation and Helmholtz solvers for the analysis of rotating modes in an industrial swirled burner. *Combustion and Flame*, *145(1-2), 194–205*. http://doi.org/10.1016/j.combustflame.2005.10.017

Sheen, H. J., Chen, W. J., and Jeng, S. Y. (1996). Recirculation zones of unconfined and confined annular swirling jets. *AIAA Journal*, *34(3), 572–579*. http://doi.org/10.2514/3.13106

Simmons, J. M., and Laif, J. C. S. (1981). Jet Excitation by an Oscillating Vane. *AIAA Journal*, *19(6), 673–676*.

Sirovich, L. (1987). Turbulence and the dynamics of coherent structures part I: coherent structures. *Quartely of Applied Mathematics*, *45(3), 561–571*.

Smithat, N. L., Megalosa, N. P., Nathana, G. J., Zhangb, D. K., and Smart, J. P. (1998). Precessing jet burners for stable and low NO, pulverised fuel flames - preliminary results from small-scale trials. *Fuel, 77(9), 1013–1016*.

Soloff, S. M., Adrian, R. J., and Liu, Z.-C. (1999). Distortion compensation for generalized stereoscopic particle image velocimetry. *Measurement Science and Technology*, *8(12)*, *1441–1454*. http://doi.org/10.1088/0957-0233/8/12/008

Stöhr, M., Boxx, I., Carter, C. D., and Meier, W. (2012). Experimental study of vortex-flame interaction in a gas turbine model combustor. *Combustion and Flame*, *159(8), 2636–2649*. http://doi.org/10.1016/j.combustflame.2012.03.020

Stöhr, M., Sadanandan, R., and Meier, W. (2011). Phase-resolved characterization of vortex-flame interaction in a turbulent swirl flame. *Experiments in Fluids*, *51(4), 1153–1167*. http://doi.org/10.1007/s00348-011-1134-y

Syred, N. (2006). A review of oscillation mechanisms and the role of the precessing vortex core (PVC) in swirl combustion systems. *Progress in Energy and Combustion Science*, *32(2), 93–161*. http://doi.org/10.1016/j.pecs.2005.10.002

Syred, N., and Beér, J. M. (1974). Combustion in swirling flows: A review. *Combustion and Flame*, *23(2), 143–201*. http://doi.org/10.1016/0010-2180(74)90057-1

Syred, N., and Dahman, K. R. (1978). Effect of High Levels of Confinement upon the Aerodynamics of Swirl Burners, *Energy Journal, 2(1), 8–15*.

Syred, N., O'Doherty, T., and Froud, D. (1994). The interaction of the precessing vortex core and reverse flow zone in the exhaust of a swirl burner. *ARCHIVE: Proceedings of the Institution of Mechanical Engineers, Part A: Journal of Power and Energy 1990-1996, 204-210, 208, 27–36*. http://doi.org/10.1243/PIME_PROC_1994_208_006_02

Syred, N., Wong, C. Y., Rodriguez-Martinez, V. M., Dawson, J. R., and Kelso, R. M. (2004). Characterisation of the Occurrence of the Precessing Vortex Core in Partially Premixed and Non-Premixed Swirling Flow. *In 12th international symposium on the applications of laser techniques to fluid mechanics*, *21–3*.

Toh, I. K., Honnery, D., and Soria, J. (2010). Axial plus tangential entry swirling jet. *Experiments in Fluids*, *48(2), 309–325*. http://doi.org/10.1007/s00348-009-0734-2

Tsai, R. Y. (1987). A Versatile Camera Calibration Technique for High-Accuracy 3D Machine Vision Metrology Using Off-the-Shelf TV Cameras and Lenses. *IEEE Journal on Robotics and Automation*. http://doi.org/10.1109/JRA.1987.1087109

Van Oudheusden, B. W., Scarano, F., Van Hinsberg, N. P., and Watt, D. W. (2005). Phase-resolved characterization of vortex shedding in the near wake of a square-section cylinder at incidence. *Experiments in Fluids*, *39(1), 86–98*. http://doi.org/10.1007/s00348-005-0985-5

Violato, D. (2013). *3D flow organization and dynamics in subsonic jets. PhD Thesis, TU Delft University.*

Violato, D., and Scarano, F. (2011). Three-dimensional evolution of flow structures in transitional circular and chevron jets. *Physics of Fluids*, *23(12), 1–25*. http://doi.org/10.1063/1.3665141

Westerweel, J. (1993). *Digital Particle Image Velocimetry - Theory and Application. TU Delft University Press*.

Westerweel, J. (1999). Fundamentals of digital particle image velocimetry. *Measurement Science and Technology*, *8(12), 1379–1392*. http://doi.org/10.1088/0957-0233/8/12/002

Westerweel, J., Elsinga, G. E., and Adrian, R. J. (2013). Particle Image Velocimetry for Complex and Turbulent Flows. *Annual Review of Fluid Mechanics*, *45(1), 409–436*. http://doi.org/10.1146/annurev-fluid-120710-101204

Wieneke, B. (2008). Volume self-calibration for 3D particle image velocimetry. *Experiments in Fluids*, *45(4), 549–556*. http://doi.org/10.1007/s00348-008-0521-5

Wille, R., and Fernholz, H. (1965). Report on the first European Mechanics Colloquium, on the Coanda effect. *Journal of Fluid Mechanics*, *23*(04), 801. http://doi.org/10.1017/S0022112065001702

Willert, C. (1999). Stereoscopic digital particle image velocimetry for application in wind tunnel flows. *Measurement Science and Technology*, *8(12), 1465–1479*. http://doi.org/10.1088/0957-0233/8/12/010

Willert, C. E., and Gharib, M. (1991). Experiments in Fluids Digital particle image velocimetry. *Experiments in Fluids*, *10, 181–193*. http://doi.org/10.1007/s00348-012-1280-x

Wong, C. Y., Lanspeary, P. V., Nathan, G. J., Kelso, R. M., and O'Doherty, T. (2003). Phase-averaged velocity in a fluidic precessing jet nozzle and in its near external field. *Experimental Thermal and Fluid Science*, *27(5), 515–524*. http://doi.org/10.1016/S0894-1777(02)00265-0

Wong, C. Y., Nathan, G. J., and Kelso, R. M. (2008). The naturally oscillating flow emerging from a fluidic precessing jet nozzle. *Journal of Fluid Mechanics*, *606*, *153–188*. http://doi.org/10.1017/S0022112008001699

Wong, C. Y., Nathan, G. J., and O'Doherty, T. (2004). The effect of initial conditions on the exit flow from a fluidic precessing jet nozzle. *Experiments in Fluids*, *36(1), 70–81*. http://doi.org/10.1007/s00348-003-0642-9

Yazdabadi, P. A., Griffiths, A. J., and Syred, N. (1994). Characterization of the PVC phenomena in the exhaust of a cyclone dust separator. *Experiments in Fluids*, *17(1-2), 84–95*. http://doi.org/10.1007/BF02412807

Yule, A. J. (1978). Large-scale structure in the mixing layer of a round jet. *Journal of Fluid Mechanics*, *89, 413*. http://doi.org/10.1017/S0022112078002670

Zaman, K. B. M. Q., and Raman, G. (1997). Reversal in spreading of a tabbed circular jet under controlled excitation. *Physics of Fluids*, *9(12), 3733–3741*. http://doi.org/10.1063/1.869511

List of Publications

Journal Papers

Ceglia, G., Trifoni, E., Gouriet, J-B., Chazot, O., Mareschi, V., Rufolo G., and Tumino G. (2015). Experimental investigation on IXV TPS interface effects in Plasmatron. *CEAS Space Journal, 1-11. ISSN: 1868-2502*

Cafiero, G., Ceglia, G., Discetti, S., Ianiro, A., Astarita, T., and Cardone G. (2014). On the three-dimensional precessing jet flow past a sudden expansion. *Experiments in fluids, 55(2), 1-13,. ISSN: 0723-4864*

Ceglia, G., Discetti, S., Ianiro, A., Michaelis, D., Astarita T., and Cardone G., (2013). Three-dimensional organization of the flow structure in a non-reactive model aero engine lean burn injection system. *Experimental Thermal and Fluid Science, 52, 164-173. ISSN: 0894-1777*

Conference Proceedings

Ceglia, G., Trifoni, E., Gouriet, J-B., Chazot, O., Mareschi, V., Rufolo G., and Tumino G, OFF-STAGNATION TESTS OF ESA IXV TPS INTERFACES IN PLASMATRON, *In Proceedings of the 8th European Symposium on Aerothermodynamics for Space Vehicles, 2nd – 6th March 2015, Lisbon.*

Ceglia, G., Violato, D., Tuinstra, M., and Scarano, F. (2013). High-resolution PIV analysis of compressibility effects in turbulent jets. *In Proceedings of the 10th International Symposium on Particle Image Velocimetry, Delft, The Netherlands, July 1-3*.

Violato, D., Ceglia, G., Tuinstra, M., and Scarano, F. (2013). 3D organization of high-speed compressible jets by tomographic PIV. *In Proceedings of the 10th International Symposium on Particle Image Velocimetry, Delft, The Netherlands, July 1-3*.

Ceglia, G., Discetti, S., Ianiro, A., Michaelis, D., Astarita, T., and Cardone, G. (2013). Tomographic PIV measurements of the flow at the exit of an aero engine swirling injector with radial entry. *In Proceedings of the 10th International Symposium on Particle Image Velocimetry, Delft, The Netherlands, July 1-3.*

Cafiero, G., Ceglia, G., Discetti, S., Ianiro, S., Astarita, T., and Cardone, G. (2013). The three-dimensional swirling flow past a sudden expansion. *In Proceedings of the 10th International Symposium on Particle Image Velocimetry, Delft, The Netherlands, July 1-3.*

Ceglia, G., Discetti, S., Ianiro, A., Michaelis, D., Astarita, T., and Cardone, G. (2013). Three-dimensional organization of flow structures at the exit of an aero-engine double swirling injector*. In Proceedings of the 8th World Conference on Experimental Heat Transfer, Fluid Mechanics and Thermodynamics, Lisbon, Portugal*, *16-20.*

Cafiero, G., Ceglia, G., Discetti, S., Ianiro, S., Astarita, T., and Cardone, G. (2013). The three-dimensional swirling flow past a sudden expansion. *In Proceedings of the 8th World Conference on Experimental Heat Transfer, Fluid Mechanics and Thermodynamics, Lisbon, Portugal*, *16-20.*

Ceglia, G., Discetti, S., and Astarita T. (2012). On the coherent structures motion in horizontal convection. *In Proceedings of the 15th International Symposium on Flow Visualization, Minsk, Belarus, June 25-28.*

Ceglia, G., and Discetti S. (2012). An experimental analysis in horizontal convection with IR thermography. *In Proceedings of the 11th International Conference on Quantitative InfraRed Thermography, Naples, Italy, June 11-14.*

Acknowledgments

Firstly, I am grateful to my supervisor Prof. Tommaso Astarita, who, with continuous support and dedication, guided me along the path of my PhD. I really appreciated the opportunity that you offered me for this Ph.D. I would like to thank Prof. Gennaro Cardone for your criticism during our technical and scientific discussions to find the right way through the variegate situations of complicate experimental setups. I sincerely thank Prof. Carlomagno for all valuable scientific explanations; I really appreciated the support that you gave me during my PhD. Many thanks go to Prof. Filvio Scarano for hosting me in his Lab at Delft University of Technology for a period of three months. During this period of dense scientific activities, you transmitted me your enthusiasm and pragmatism, essential for giving the best out of me.

A very special thank goes to Prof. Stefano Discetti, who was my tutor for my Master's thesis. I admire you for your constant dedication to the scientific research, always available for profitable discussions. I really appreciate your prompt support as loyal friend and enthusiastic researcher. I thank Prof. Andrea Ianiro, for the patience during the first part of my PhD, I enjoyed the time spent together during our experimental activities.

I would like to thank my colleagues and friends of the Labs at the University of Naples. Many warmly thanks go to Carlo Greco, Francesco Avallone, Gioacchino Cafiero and Roberto Opromolla. Dear friends, I very much enjoyed your friendship during my days at the Lab. I want to thank Giuseppe Sicardi for your technical solutions essentials for my experiments.

In Netherlands, I would also like to thank all the special people I was lucky to meet: Daniele Violato, Daniele Fiscaletti, Daniele Ragni, Jacopo Serpieri and Laura Vitale.

I thank my actual company Centro Italiano Ricerche Aerospaziali CIRA for allowing me the opportunity to conduct my PhD. In particular, my thanks go to Antonio Del Vecchio, who supported my research activities since the very beginning in CIRA. I would like to thank also my colleagues and friends Gianluca Amendola, Eduardo Trifoni, Carlo Purpura, Vincenzo Fiorillo, Luigi Savino and Adolfo Martucci.

Certainly, I have to thank my best friends for always accepting me for what I am: Donato Amitrano, Marco Lanzetta, Biagio Guadagni, Michele Pecchia and Salvatore Capodanno.

Acknowledgments

Most remarkably, I want to thank my family, which believed in me with great patient and commitment during these years. Many many thanks go to my brother Antonio and my sister Mariarosaria, you have given me all the love that I need to overcome my limits and follow the path of my life. And now… I am very curious about what will happen next.